

ON-CHIP QUANTUM PHOTONICS:
LOW MODE VOLUMES, NONLINEARITIES AND NANO-SCALE
SUPERCONDUCTING DETECTORS

A Dissertation

Submitted to the Faculty

of

Purdue University

by

Saman Jahani

In Partial Fulfillment of the

Requirements for the Degree

of

Doctor of Philosophy

December 2018

Purdue University

West Lafayette, Indiana

THE PURDUE UNIVERSITY GRADUATE SCHOOL
STATEMENT OF DISSERTATION APPROVAL

Prof. Zubin Jacob, Chair

School of Electrical and Computer Engineering

Prof. Minghao Qi

School of Electrical and Computer Engineering

Prof. Mahdi Hosseini

School of Electrical and Computer Engineering

Prof. Muhammad Ashraful Alam

School of Electrical and Computer Engineering

Approved by:

Prof. Pedro Irazoqui

Head of the School Graduate Program

To my parents

ACKNOWLEDGMENTS

This work could not be done without the helps and supports of many people. Above all, I would like to thank my advisor, Zubin Jacob, for his patience, endless encouragement, and support. I was very grateful to be one of his first PhD students and work closely with him. Zubin took a lot of time to discuss the ideas and to guide me through understanding difficult problems and solving them in the simplest form. I could not have asked for a better PhD advisor.

I would like to express my gratitude to Minghao Qi for his support and spending lots of time, energy, and precious nanofab money to realize on-chip devices and serving in my committee, Lukas Chrostowski for giving me the opportunity to learn silicon photonic design through SiEPIC program and for his fruitful comments on my designs, Ray DeCorby for giving us access to his lab and for the input on measuring relaxed total internal reflection and the deposition of multilayer waveguides, Vien Van for the collaboration on the fabrication and measurement of multilayer waveguides, Adrián Buganza Tepole for the input on solving diffusion equations, Hong Tang and Joseph Bardin for the input on superconducting single photon detectors. I would also like to thank Muhammad Ashraf Alam and Mahdi Hosseini for taking the time serving in my committee and for their comments and suggestions which have helped to improve my thesis, and Pinder Bains and Matt Golden for the administrative helps at the University of Alberta and Purdue University.

I have been extremely lucky to be surrounded by a group of friendly and talented colleagues at the University of Alberta and Purdue University. Especially, I would like to thank Farid Kalhor for his friendship and all the time we spent to discuss different ideas. Many thanks to Prashant Shekhar, Ward Newman, Cristian Cortes, and Sean Molesky, whom I worked with since the start of my PhD, for their scientific insights, their comments on my work, and all the fun we had together. I would like

to thank Jonathan Atkinson and Sagsik Kim for their commitments in collaboration to observe relaxed total internal reflection and skin-depth engineering, Li-Ping Yang, Sarang Pendharker, Hangqi Zhao, and Todd Van Mechelen for the collaboration and for their theoretical insights, and Ryan Starko-Bowes for his experimental insights.

I am thankful to Kasra Nikooyeh and Shima Khatibisepehr for their unconditional support and having me as a member of their family. I am deeply indebted to them.

Thanks to all my wonderful friends in Edmonton and West Lafayette whom I could always count upon, especially Moien Alizadehgiashi, Fariborz Daneshvar, Farzad Yazdanbakhsh, Sattar Soltani, Ammar Hassanzadeh Keshteli, Anahita Sadeghian, Mahdie Mojarad, Amin Pourmohammadbagher, and Mahsa Mehranfar for the amazing times we spent together between all works.

Last but not least, I want to thank the main source of energy in my life. I would like to thank my parents, Ahmad Jahani and Zahra Hosseinzadeh, my sister, Nazanin Jahani, and my brother, Nariman Jahani for their unlimited love and care. I am not sure that without their encouragements, I would have ever chosen to reach this level.

PREFACE

Chapter 1 and 2 in this thesis are reproduction of previously published works as:

- S. Jahani and Z. Jacob “Transparent sub-diffraction optics: Nanoscale light confinement without metal,” *Optica*, 1 (2), 96-100, (2014).
- S. Jahani and Z. Jacob “Photonic skin-depth engineering,” *Journal of Optical Society of America B*, 32 (7), 1346-1353, (2015).
- S. Jahani and Z. Jacob “Breakthroughs in Photonics 2014: Relaxed total internal reflection,” *IEEE Photonics Journal*, 7 (3), 0700505, (2015).

Chapter 3 is part of a research collaboration led by Z. Jacob and M. Qi. The results have been published as:

- S. Jahani et. al. “Controlling evanescent waves using silicon photonic all-dielectric metamaterials for dense integration,” *Nature Communications*, 9, 1893, (2018).

Chapter 3 is reproduction of previously published work as:

- S. Jahani, H. Zhao, and Z. Jacob “Switching Purcell effect with nonlinear epsilon-near-zero media,” *Applied Physics Letters*, 113 (2), 021103, (2018).

In these works, Z. Jacob served as the supervising author and was involved with concept formation and finalizing the manuscripts for publication. I am responsible for all other aspects.

TABLE OF CONTENTS

	Page
LIST OF TABLES	x
LIST OF FIGURES	xi
ABBREVIATIONS	xxx
ABSTRACT	xxxix
1 Background and motivation	1
1.1 Motivation	1
1.2 Historic perspective and thesis structure	3
1.2.1 Sub-diffraction photonics	3
1.2.2 Nonlinear epsilon-near-zero media	6
1.2.3 Single-photon detectors	6
2 Transparent subdiffraction optics: nanoscale light confinement without metal	9
2.1 Outline of the problem	9
2.2 Paradigm shift in light confinement strategy	10
2.2.1 Relaxed-Total Internal Reflection	12
2.2.2 Transforming optical momentum	12
2.2.3 Controlling optical momentum with dielectric anisotropy	13
2.3 Sub-diffraction light confinement without metal	13
2.4 Better than vacuum?	17
2.5 Figures of merit	18
2.5.1 Mode-length	19
2.5.2 Mode-width	20
2.5.3 Power in the core	21
2.6 1D Practical Realization	21
2.7 Application to Photonic integration	23

	Page
2.8	2D Extreme Skin-depth Waveguides 24
2.9	Goos-Hänchen phase shift 26
2.10	Summary 27
3	On-chip all-dielectric metamaterials for dense photonic integration 28
3.1	Outline of the problem 28
3.2	Relaxed total internal reflection 33
3.3	On-chip e-skid waveguides 35
3.4	Cross-talk in e-skid waveguides 39
3.5	Bending loss in e-skid waveguides 40
3.6	Methods 44
3.7	Summary 46
4	Switching Purcell effect with nonlinear epsilon-near-zero media 47
4.1	Outline of the problem 47
4.2	Linear and nonlinear response of hyperbolic metamaterials at ENZ . . . 48
4.3	Switching of evanescent waves 54
4.4	Summary 57
5	Superconducting nanowire single-photon detectors: quantum timing jitter and spectral dependence of quantum efficiency 58
5.1	Outline of the problem 58
5.2	Detection mechanism 61
5.2.1	Quasi-particle multiplication 62
5.2.2	Current redistribution 63
5.2.3	Single vortex crossing 63
5.3	Quantum timing jitter corresponding to the single-vortex crossing . . . 73
5.4	Energy-dependence and pulse-width dependence of the quantum efficiency 75
5.5	Summary 76
A	Additional results for transparent sub-diffraction optics 78
A.1	Relaxed total internal reflection 78

	Page
A.2 1D Extreme-skin-depth Waveguides	81
A.3 2D Extreme-skin-depth Waveguides	83
A.3.1 Dual-anisotropic cladding	83
A.3.2 Non-magnetic anisotropic cladding	86
A.4 Metamaterial fiber	90
A.5 Quasi-TEM waveguide	92
A.6 Figures of merit	94
A.6.1 Mode length/area	94
A.6.2 Power in the core	96
A.6.3 Cross-talk	96
A.7 Practical realization 1D and 2D	99
A.8 Comparison of different waveguide classes	101
A.8.1 Optical fibers	101
A.8.2 Photonic crystal fibers	102
A.8.3 Plasmonic waveguides	102
A.8.4 Slot waveguides	102
A.8.5 Extreme-skin-depth waveguides	102
A.9 Method	103
B Additional results for on-chip extreme skin-depth waveguides	104
B.1 Relaxed total internal reflection	104
B.2 Effect of periodicity and disorder on e-skid waveguides	104
B.3 Cross-talk	106
B.4 Bending loss	112
B.5 Mode conversion efficiency	117
B.6 Propagation loss	119
REFERENCES	121

LIST OF TABLES

Table	Page
3.1 Performance comparison between an e-skid waveguide and other dielectric waveguides. It is seen that the cross-talk is significantly reduced in e-skid waveguides at the negligible cost of propagation loss in comparison with other approaches.	31

LIST OF FIGURES

Figure	Page
1.1 Platform for on-chip quantum nanophotonics. The purpose of this study is to demonstrate some key elements for all-optical quantum information processing on a chip. We have proposed a nonlinear tunable epsilon-near-zero (ENZ) structure to enhance and to modulate decay rate of photon emissions from a quantum emitter. Emitted photons are strongly confined and guided by extreme skin-depth (e-skid) waveguides in an ultra-dense photonic integrated circuit without coupling to the adjacent waveguides or scattering at sharp bends. Since e-skid waveguides strongly confine light into a small area, the interaction of photons with a short superconducting nanowire single-photon detector (SNSPD) is enhanced. Hence, the photons are efficiently detected with a high temporal accuracy.	2
1.2 Mode volume in microwave and photonic structures. At low frequencies, metals are perfect reflectors and they can confine light to increase light matter interaction. At optical frequencies, because of the intrinsic loss of metals, light is dissipated and does not allow strong light matter interaction. Dielectric structures, such as photonic crystal cavities and microdisk resonators can confine light, but the mode volume in these dielectric structures is limited by the diffraction limit of light which impedes further confinement. Figure is reproduced from ref. [45] and ref. [11]. . . .	4
1.3 Various approaches to nano-waveguiding. a , Hybrid plasmonic waveguide. b , Dielectric slot waveguide. c , Photonic crystal waveguide. d , Extreme skin depth (e-skid) waveguide.	5
1.4 Schematic representation of main detection models for superconducting nanowire single photon detectors (SNSPDs). a , Hot-spot model. b , Quasi-particle (QP) diffusion model. c , Vortex-antivortex unbinding model. d , Single-vortex crossing model.	7

2.1 **Relaxed total internal reflection.** **a**, Conventional total internal reflection: If $n_1 > n_2$ and the incident angle is larger than the critical angle, the light is totally reflected to the 1st medium and decays in the 2nd medium. **b**, Relaxed total internal reflection: If $n_1 > \sqrt{\epsilon_x}$ and the incident angle is larger than the critical angle, the light is totally reflected. However, the penetration depth can be decreased considerably if $\epsilon_z \gg 1$. **c**, Wave propagation along the optical axis of a uniaxial medium. As the electric field is perpendicular to the momentum direction, permittivity in specific direction controls the momentum in the perpendicular direction. **d**, Conventional waveguide based on total internal reflection: As the core size is decreased, most of the power lies outside and decays slowly in the cladding. **e**, Transformed cladding waveguide: Relaxed total internal reflection ($n_1 > \sqrt{\epsilon_x}$) preserves the conventional waveguiding mechanism. Furthermore, the light decays fast in the cladding as the optical momentum in the cladding is transformed using anisotropy ($\epsilon_z \gg 1$). Thus the wave can be confined inside the core giving rise to sub-diffraction optics with completely transparent media. 11

2.2 **Subdiffraction light confinement without metal.** Normalized tangential electric field of the TM mode for a glass slab waveguide with a size of 0.1λ surrounded with all-dielectric metamaterial cladding. The metamaterial has dielectric constants of ($\epsilon_x = 1.1$ and $\epsilon_z = 15$). On comparison with a conventional mode which has air as the surrounding medium, a rapid decay of the evanescent fields is observed. The plots are normalized to the same input electric energy. (inset) As the anisotropy of the cladding is increased the mode length decreases significantly below the diffraction limit with completely transparent media. This can be achieved with a cladding size (width b), three times that of the core (width a) 14

2.3 **Mode length comparison of slab waveguides with core size.** It shows that the anisotropic cladding ($\epsilon_x = 1.1$ and $\epsilon_z = 15$) can confine the TM mode to sub-diffraction values. (inset) We emphasize that the net power in the core is also higher for the TCW as compared to conventional waveguides. 15

Figure	Page
2.4 Is the transparent anisotropic cladding better than vacuum cladding for confinement? (a) It is known that a silicon waveguide in vacuum is the best waveguide for low loss power confinement at optical frequencies. (b) However, we conclusively prove that if the cladding is strongly anisotropic, light confinement can be increased substantially. (c) The x-component of the electric field of HE ₁₁ mode for silicon waveguide in vacuum. The core radius is $r = 0.07\lambda$. Less than 2% of the power is confined inside the silicon core. (d) The x-component of the electric field of HE ₁₁ mode for the same waveguide surrounded by an anisotropic cladding ($\epsilon_x = \epsilon_x = 1.2 < \epsilon_{Si}$ and $\epsilon_z = \epsilon_{Si} = 12$). The cladding helps to confine up to 30% of the total power inside the core.	17
2.5 Figures of merit for 1D e-skid waveguides. (a) mode length, (b) mode width, and (c) power confinement. The core is glass. The isotropic cladding is air and the anisotropic cladding has a permittivity of $\epsilon_x = 1.2$ and $\epsilon_z = 15$	18
2.6 Power confinement versus cladding index. The core is silicon ($\epsilon_c = n_c^2 = 12$) with a size of 200 nm operating at $\lambda = 1550nm$. (a) The cladding is isotropic. If the contrast between the core and cladding index increases, a larger fraction of the total power is confined inside the core. (b) The cladding is anisotropic with $\epsilon_x = 1.2$. As the anisotropy of the cladding is enhanced, more power is confined inside the core. Thus the conventional waveguide and e-skid waveguide show fundamentally different behavior with increasing cladding index. The power is defined through the electromagnetic energy density defined in Appendix B and can be obtained by solving for the fields of a slab waveguide with anisotropic cladding. . . .	19

- 2.7 **Dense photonic integration at optical telecommunication wavelength** ($\lambda = 1550nm$). **a**, The transformed cladding with low cross-talk between closely spaced waveguides. This can be achieved by surrounding the waveguide cores (blue) with multilayer all-dielectric metamaterials. The multilayer metamaterial consisting of alternating sub-wavelength layers Germanium (26 nm) and Silica (14 nm). This all-dielectric structure achieves the anisotropy of ($\epsilon_x = 4.8$ and $\epsilon_z = 11.9$) **b**, Comparison of coupling length (cross-talk) for conventional slab waveguides, slot waveguides and transformed cladding waveguides. It is seen that the TCW improves the cross-talk by an order of magnitude and the practical multilayer structure result is in excellent agreement with the effectively anisotropic cladding. The core is silicon with a center to center separation of 0.5λ between waveguides. Each slot-waveguide has the same net size as the core of the other waveguides, the slot size is 0.01λ and is filled with glass. If the slot size is larger or the slot index is lower, the cross talk performance is worse than that shown above. Also note that the slot waveguide cross-talk is in fact always more than the conventional waveguide. 22
- 2.8 **2D extreme skin-depth waveguides.** **a**, Simulated distribution of the electric energy density inside a low-index 2D dielectric waveguide with arbitrary cross section using metamaterial claddings. **a**, The waveguide without cladding, **b**, the waveguide with all-dielectric non-magnetic cladding ($\epsilon_x = \epsilon_y = 1.2$ and $\epsilon_z = 15$). When the anisotropic cladding is added, the mode area of the waveguide is decreased from about $80A_0$ to $0.7A_0$, and the fraction of power inside the core to the total power is increased from less than 1% to about 36%. 24
- 2.9 **Goos-Hänchen effect in anisotropic media.** (a) Reflection amplitude and (b) reflection phase versus the incident angle. The first medium is glass and for the second medium $\epsilon_x = 1.2$. (c) Goos-Hänchen phase shift versus ϵ_z of the second medium. We assume the center of angular spectrum of the incident beam is 1% above the critical angle and all of the angular spectrum components are greater than the critical angle. As the anisotropy increases (i.e. skin depth decreases), the Goos-Hänchen phase shift decrease. 25

Figure	Page
<p>3.1 Fundamental differences between dielectric waveguides on an SOI platform. a, strip waveguide; b, photonic crystal waveguide; c, slot waveguide; d, e-skid waveguide. The skin-depth in the cladding of e-skid waveguide is shorter compared to the other structures due to the strong effective anisotropy of the multilayer cladding. This counterintuitive approach can have a cladding with a higher average index than the core and marks a departure from interference based confinement as in photonic crystal waveguides or slot waveguides which utilize nanoscale field enhancement.</p>	30
<p>3.2 Relaxed total internal reflection. a, Schematic of the relaxed-TIR experiment. We measure the reflection from the Si prism and Si/SiO₂ multilayer interface for both <i>s</i> and <i>p</i> polarizations at $\lambda = 1550$ nm. Multiple samples with different ρ have been fabricated. The periodicity for all samples is 100 nm and the total thickness of the multilayer is 500 nm. A 200 nm layer of tungsten is deposited on top of the multilayer (brown) to suppress the reflection from the air interface. b, The measured critical angle for <i>s</i> and <i>p</i> polarizations versus the silicon filling fraction in comparison with effective medium theory (EMT) calculations. Error bars represent the instrument limit of the measuring device. In contrast with the conventional phenomenon of TIR, observable differences between the critical angles is seen for different polarizations in agreement with relaxed-TIR theory. c, Retrieved effective permittivity of the multilayer from the critical angle measurements show strong anisotropy in agreement with EMT. The refractive index of Si and SiO₂ are taken to be 3.4 and 1.47, respectively, for the theoretical calculations. The inset shows the SEM image of an Si/SiO₂ multilayer with $\rho = 0.5$. d, Normalized calculated magnetic field profile for the TM mode of a conventional slab waveguide compared to extreme skin-depth (e-skid) waveguides with Si/SiO₂ multilayer cladding. The blue and grey regions represent Si and SiO₂, respectively. The core size, Λ, and ρ are 100 nm, 30 nm, and 0.5, respectively. The multilayer anisotropic claddings strongly affect the decay of the evanescent wave in the cladding. The practical multilayer structure performs close to an ideal anisotropic case ($\epsilon_{2x} = \epsilon_{\text{SiO}_2}$ and $\epsilon_{2z} = \epsilon_{\text{Si}}$).</p>	32

- 3.3 On-chip extreme skin-depth waveguides.** **a**, Ideal on-chip e-skid waveguide; light is confined by total internal reflection inside the core and as the effective anisotropy of the multilayer metamaterial cladding is increased, evanescent waves of TE-like modes decay faster in the cladding in comparison with the field in strip waveguides ($\varepsilon_{2z} = 1$). Note that $\varepsilon_{2x} = 1$ for all cases. **b**, The simulated electric field profile at the center of the e-skid waveguide with multilayer (green) and homogenized metamaterial ($\varepsilon_{2x} = 1.85$ and $\varepsilon_{2z} = 6.8$) (red) claddings, in comparison with a strip waveguide (blue). Inset shows the SEM image of the fabricated e-skid to strip waveguide transition. **c**, **d**, Schematic and field profiles of **(c)** realistic e-skid waveguide with multilayer claddings and **(d)** its equivalent model with EMT claddings. **e**, **f**, Effective refractive indices ($n_{\text{eff}} = k'_z/k_0$) and **g**, **h**, normalized decay constants ($k''_x/k_0 = 1/\delta k_0$) of the e-skid waveguide as functions of the core width w_0 and filling fraction ρ : with **(e, g)** multilayer and **(f, h)** EMT claddings, respectively. Geometric parameters are $h_0 = 220$ nm, $w_0 = 350$ nm, $\Lambda = 100$ nm, $\rho = 0.5$, and $N = 5$, unless otherwise indicated. The free space wavelength is $\lambda = 1550$ nm. Simulations confirm that the cladding achieves effective all-dielectric anisotropy as well as the increased decay constant of evanescent waves outside the core. 36

- 3.4 **Cross-talk in e-skid waveguides.** **a**, Schematic of coupled e-skid waveguides on an SOI platform. The waveguide height, center-to-center separation between the two waveguides (s), and Λ are 220 nm, 1000 nm, and 120 nm, respectively. A cladding oxide is also added on the top of the waveguides. The number of ridges between the waveguides is dictated by the waveguide core size **b**, Top view SEM image of the coupled e-skid waveguides. **c**, The experimental setup to measure the cross-talk between the two waveguides at the telecommunication wavelength ($\lambda = 1550$ nm). Light is in-coupled to the first waveguide through the middle grating coupler. The second waveguide is coupled to the first waveguide for a length of L . In this experiment, the bending radius is $5 \mu\text{m}$, hence, we can ignore the bending loss. **d**, The ratio between the measured output powers for strip waveguide and e-skid waveguide versus L at the telecommunication wavelength, respectively. The ratio for the e-skid waveguide is two orders of magnitude lower, indicating that far less power is coupled to the second waveguide. The inset shows the ratio for the waveguides without the top cladding oxide. In this case, the metamaterial cladding can increase the coupling length up to 30 times or reduce the cross-talk -30 dB. See Supplementary Figure 8 for more details. **e**, Comparison of the simulated and measured coupling length for e-skid waveguides and strip waveguides. The coupling length is normalized to the wavelength. Error bars represent the standard deviation of the fitting curves. The optimum match between the simulation and experiment is achieved when $\rho = 0.6$ for the cladding of e-skid waveguides. The coupling length for e-skid waveguides is an order of magnitude larger in comparison with strip waveguides (shaded region). The coupling length for strip waveguides with larger core size decreases because the overlap between the evanescent tails is increased although more power is confined inside the core (unshaded region). 38
- 3.5 **Curved waveguides and skin-depth engineering.** **a, b**, Refractive index profile (blue) and the magnetic field profile (green) of (a) a straight strip waveguide and (b) a straight e-skid waveguide. **c**, The corresponding bent waveguides (c,d) can be transformed to straight waveguides with inhomogeneous refractive index profiles in a new coordinate system. If the local refractive index of the cladding exceeds the effective modal index ($n'(u_0) > n_{\text{eff}}$), the waveguide mode starts radiating. This occurs at the radiation condition point denoted by $u = u_0$ (red arrows). The multi-layer metamaterial cladding in e-skid waveguides suppresses the evanescent wave field beyond this radiation condition point. Thus, in comparison with conventional bent waveguides, lesser power is radiated due to curvature effects. 41

Figure	Page
<p>3.6 Bending loss in e-skid waveguides. a, Layout and zoomed-in SEM images of the test devices to characterize the bending loss. b, Measured bending losses with different number of turns; circles and crosses are the e-skid and strip waveguides, respectively, and blue, green, and red are at different bending radiuses of $R = 1, 2,$ and $3 \mu\text{m}$. Each experimental result is fitted with a linear line: e-skid (solid) and strip (dashed) lines. The core size is $w_0 = 350 \text{ nm}$. c, Characterized bending loss vs. core size ($R = 1 \mu\text{m}$): e-skid (red) and strip (blue) waveguides. Inset shows the characterized bending loss vs. bending radius ($w_0 = 350 \text{ nm}$). Red and blue lines are the simulated bending losses of the e-skid and strip waveguides, respectively. Error bars represent the standard deviation of the fitting curves. Other parameters ($h_0, \Lambda, \rho, N,$ and λ) are the same as in Fig. 3.3. Confinement of the evanescent waves in e-skid waveguides due to the metamaterial cladding helps to reduce the bending loss at sharp bends in photonic integrated circuits. This effect is stronger for waveguides with smaller core sizes, as a considerable amount of the power lies outside the core and decays slowly.</p>	42
<p>4.1 Switching of Purcell effect. (a) A nonlinear gate signal controls the transmission of evanescent waves emitted by a quantum emitter above HMM around the ENZ frequencies. (b) The real part of effective permittivity of the Ag/TiO₂ multilayer metamaterial with Silver filling fraction of $\rho = 0.5$. The inset illustrates the iso-frequency dispersion curve of type I and type II HMMs. An optical topological transition is observed at ENZ. (c) Transmission of propagating and evanescent p-polarized waves through an Ag/TiO₂ multilayer with a total thickness of 400 nm and a periodicity of $\Lambda = 50 \text{ nm}$. The transmission of high-k modes in both regions is high, but in type I region, the effect is stronger, especially close to the ENZ wavelengths. Due to the finite thickness of the unit-cell, the ENZ wavelength is red-shifted in multilayer structure in comparison with EMT. (d) Purcell factor for a vertically oriented dipole above the slab modeled by EMT. A rapid change in the Purcell factor is observable at ENZ due to the optical topological transition. Other peaks in type I correspond to slow-light modes of the HMM slab.</p>	49

Figure	Page
4.2 Nonlinear response at ENZ. Nonlinear response of (a) <i>s</i> polarized and (b) <i>p</i> polarized incidences at different incident angles for the multilayer structures in Fig. 4.1 at $\lambda = 522$ nm which is slightly longer than the ENZ wavelength. As the input power increases, the transmission increases due to the change in effective permittivity of the multilayer slab. The power level is independent of the incident angle for the <i>p</i> -polarization. It is important to note that ENZ media show bistable behavior in the presence of low loss (inset). This bistability does not exist if we take into account nonlinear absorption i.e. imaginary part of $\chi^{(3)}$	51
4.3 Optically induced ENZ transition metamaterial. (a) Electric field distribution for the <i>p</i> polarized incidence when $I_{in}=8$ GW/cm ² and the incident angle is 45°. Since the operating wavelength is close to the ENZ and epsilon-near-pole (ENP) resonance, ϵ_z is very large which causes the electric field E_z to become very small in comparison with E_x . (b) Nonlinear ENZ transition metamaterials: The nonlinear effective permittivity of the HMM slab when the pump is on. We can see the topological transition from type II to type I occurs as a function of distance (as opposed to wavelength) due to the inhomogeneous power distribution inside the multilayer slab. This shows a unique regime of the multi-layer super-lattice functioning as a transition metamaterial.	52
4.4 Effect of nonlinear gate pulse on the linear transmission (a) around and away from the ENZ point. (a) Transmission of signal through the multilayer medium in the presence of the pump in comparison with that when the pump is off at $\lambda = 522$ nm. The nonlinearity allows us to suppress or enhance transmission of evanescent waves. The nonlinear pulse suppresses the Purcell factor from 41 to around 15. (b) Comparison of the transmission away from the transition point. The nonlinear pulse does not change the transmission for a wide range of wave-vectors. Thus the pump signal does not change the Purcell factor considerably.	55
4.5 Nonlinear response of the HMM slab to a finite pulse width. (a) Nonlinear transmission versus the pulse width at $\lambda = 500$ nm using FDTD method. The electric field amplitude is 10^4 V/m. When the pulse-width is very short, the electric field cannot be distributed in the entire space of the slab, so the pump cannot increase the transmission considerably. As the pulse-width increases, the transmission increases, and it approaches to the steady-state response when the pulse width is longer than 50 fs. (b) The Purcell factor at $\lambda = 500$ nm versus time in the presence of the gate signal. The nonlinear gate signal can switch the Purcell effect. We can see that the change in Purcell factor far away from the ENZ wavelength is negligible.	55

- 5.1 **Superconducting nanowire single photon detectors (SNSPDs).** **a**, When a photon falls on the detector, quasi-particles (QPs) are multiplied and the bias current is redistributed. Vortices are the topological defects of a thin superconductor and are nucleated at the nanowire edge. They can move to the other edge due to the force exerted by the bias current. **b**, Before the photon absorption, the vortex potential barrier does not allow them to move easily. However, due to the QP multiplication and current redistribution, the barrier reduces and vortices can be thermally excited and escape the barrier and cross the width of the nanowire. This process generates a voltage pulse propagating to the two ends of the detector. 59
- 5.2 **a**, and **b**, QP distribution, $C_{qp}(\vec{r}, t)$, normalized to the Cooper pair density, $n_{se,0}$, in a TaN SNSPD at $t = 1$ ps and $t = 5$ ps, respectively. It is assumed the photon is absorbed at $t = 0$. $T = 0.6$ °K. The photon energy is $h\nu = 1.5$ eV. The nanowire width, length, and thickness are 100 nm, 1000 nm, and 5 nm, respectively. **c**, and **d**, Normalized Current density in the y direction at $t = 1$ ps and $t = 5$ ps, respectively. The current density is normalized to the applied bias current. The arrows represent the current density vector, $\vec{j}(\vec{r}, t)$. Due to the hot-spot formation, current is redistributed and directed to the side walls. 61
- 5.3 **Vortex barrier dynamics** **a**, Vortex potential as a function of the vortex location (x_v) around the saddle point after the photon absorption for a TaN SNSPD. The photon energy and structure parameters are the same as those in Fig. 5.2. **b**, Potential barrier peak as a function of time. A change in the Cooper pairs density and current distribution reduce the barrier height. 64
- 5.4 **Vortex crossing rate and probability.** **a**, Single-vortex crossing rate as a function of time for NbN, TaN, and WSi SNSPDs. The bias current has been set to achieve a single photon detection probability of 0.5 for a photon energy of $h\nu = 1.5$ eV. The geometry is the same as that in Fig. 5.2. The enhancement in the vortex crossing rate is as a result of the suppression of the potential barrier. The probability of vortex crossing at the maximum rate is higher. However, there is considerable uncertainty in the vortex crossing time which results in a timing jitter in detection event. **b**, The evolution of vortex crossing probability as the vortex crossing rate changes. There is a steep change in the probability as the crossing rate goes up. 68

Figure	Page
5.5 Timing jitter corresponding to vortex crossing. Timing jitter in NbN, TaN, and WSi SNSPDs as a function of (a) temperature and (b) nanowire width. The other parameters are the same as that in Fig.5.4. Decreasing the temperature results in a sharper change in the vortex crossing rate. Hence, the uncertainty of vortex crossing reduces. Reducing the width of the nanowire causes that the QPs to distribute faster across the width of the nanowire, and as a result, the potential barrier reduces rapidly.	69
5.6 The effect of bias current on TaN SNSPD performance. a , Timing jitter, dark count probability (P_0), quantum efficiency (P_1) versus the bias current (I_b). I_b is normalized to the switching current (I_{SW}) which is defined as the minimum bias current at which the detector clicks in the time-bin of the single-photon arrival even if the photon is not absorbed. Note that I_{SW} is smaller than $I_{c,v}$. Increasing the bias current helps to improve the detection probability and the timing jitter but at the cost of an increase in the dark count probability. The detector parameters are the same as those in Fig. 5.2.	70
5.7 Single-photon detection probability (quantum efficiency) as a function of single-photon energy in TaN SNSPDs. The bias current is set to have near unity detection probability when the photon energy is larger than 1 eV. Other parameters are the same as those in Fig. 5.2. The exponential tail corresponds to the vortex escaping rate while the potential barrier has not vanished completely. As the temperature rises, the probability of vortex crossing increases even if the photon energy is not enough to reduce the potential barrier considerably.	71
5.8 Pulse-width dependent quantum efficiency in different models. a , Normalized QP numbers inside the ξ -slab, b , normalized current density at the edge, and, c , vortex crossing rate for different modes in a pulse with pulse width of $\tau_f = 100$ fs and the central energy of $h\nu = 0.75$ eV. It is seen that the number of QPs and current at the edge is not very sensitive to the small change of the photon energy. However, the single-vortex crossing rate is extremely sensitive as a result of a few percent change in the photon energy. d , Single-photon quantum efficiency versus the pulse-width in vortex model. The quantum efficiency is considerably increased for the very short pulses.	72

Figure	Page
A.1 The phenomenon of refraction and reflection revisited using transformation of optical momentum. Rays of light are reflected and refracted at an interface since the mesh representing electromagnetic space has a discontinuity. (a) Total internal reflection can be viewed as a transformation of optical momentum. When grid sizes in the second medium become large enough, the incident ray is totally reflected and evanescently decays in the second medium. (b) Only one component of the dielectric tensor controls the total internal reflection condition. By transforming the space in the other direction, we can control the momentum of evanescent waves and consequently decrease penetration depth in the second medium.	80
A.2 The graphical solution of (A.8) for the glass slab waveguide with a size of $\lambda_0/10$ and (a) air cladding (b) anisotropic cladding ($\varepsilon_x=1.2$ and $\varepsilon_z=20$). The solution moves to higher w (more confinement) without a large change in u .	82
A.3 Electromagnetic field profile for glass slab waveguide with a size of $\lambda_0/10$ and anisotropic cladding ($\varepsilon_x=1.2$ and $\varepsilon_z=15$) in comparison with the same waveguide without cladding. (a) Electric field. (b) Magnetic field. Field amplitudes are normalized to the same input energy. Fields decay faster in the anisotropic cladding.	82
A.4 The graphical solution by intersecting the left and right hand side of (A.13) and (A.17) for a cylindrical waveguide with glass core whose radius is $\lambda_0/10$ and the cladding is (a) air (b) anisotropic non-magnetic dielectric ($\varepsilon_{\perp} = 1$ and $\varepsilon_z = 20$) (c) dual-anisotropic dielectric ($\varepsilon_{\perp} = \mu_{\perp} = 20$ and $\varepsilon_z = \mu_z = 20$). It is seen that the waveguide mode shifts to lower values of u (higher w) denoting faster decay in the cladding.	83
A.5 The propagation constant of (a) 1D and (b) 2D nonmagnetic extreme-skin-depth (e-skid) waveguides in comparison with a conventional slab waveguide and an optical fiber with cladding permittivity of $\varepsilon = 1.1$. The core size/ radius is $\lambda_0/10$; $\varepsilon_x = 1.1$ ($\varepsilon_{\perp} = 1.1$) and $\varepsilon_z = 20$. The light line in the core and the cladding is also plotted, which shows the wave propagates inside the core due to the total internal reflection and decays away outside the core. The propagation constant in anisotropic case is larger since the power confinement is more.	88

Figure	Page
<p>A.6 (a) Schematic representation of a practical extreme-skin-depth (e-skid) metamaterial fiber at optical telecommunication wavelength ($\lambda = 1550 \text{ nm}$). The metamaterial cladding consisting of germanium nanorods embedded in porous silica surrounding a silicon rod core. (b-g) Normalized simulated distribution of the electric (top plots) and magnetic (bottom plots) energy density of the waveguide when the core diameter is 0.15λ and germanium fill fraction is 62.5%. (b) & (c) Electric and magnetic energy density of the bare waveguide. The fraction of power inside the core to the total power (η) is 3% and the mode area is $43(\lambda/2n_{core})^2$. (d) & (e) Electric and magnetic energy density of the waveguide with anisotropic cladding ($\epsilon_x = \epsilon_y = 3.7$ and $\epsilon_z = 11.8$). In the homogenized limit, the calculated η, mode area, and effective index are 35%, $1.85(\lambda/2n_{core})^2$, and 2.13, respectively. (f) & (g) Electric and magnetic energy density of the practical waveguide surrounded by nanowires which achieves the required anisotropy. According to effective theory, it achieves the effective permittivity of the cladding of part D & E. The simulated results of η, mode area, and effective index are 40%, $1.61(\lambda/2n_{core})^2$, and 2.09, respectively in agreement with the effective medium calculations. Significantly better performance can be achieved by using higher index rods in the nanowire design.</p>	89
<p>A.7 Electric field and energy density distribution of a extreme-skin-depth (e-skid) waveguide composed a cylindrical silicon core with a diameter of $0.15\lambda_0$ covered by a nonmagnetic anisotropic cladding ($\epsilon_{\perp 2}=3.7$ and $\epsilon_z=11.8$). (a) Analytical calculation. (b) Numerical calculation. The analytical calculation of η, mode area, and effective index are 34.6%, $1.94(\lambda/2n_{core})^2$, and 2.126, respectively. The simulated results are 26%, $2.58(\lambda/2n_{core})^2$, and 2.15, respectively. The slight deviations between analytical and simulated results arise due to a finite sized simulation domain.</p>	91
<p>A.8 Normalized electric field distribution of the waveguide in Fig. A.7 in comparison with the case without cladding. The cladding causes fields to decay fast outside in the cladding signifying the transformation of optical momentum.</p>	91
<p>A.9 Light confinement inside a low-index 2D dielectric waveguide using metamaterial claddings. Confining a guided wave inside a transparent low index dielectric with arbitrary cross section. The momentum transforming cladding surrounding the core leads to simultaneous total internal reflection and rapid decay of evanescent waves outside the core.</p>	92

Figure	Page
A.10 Light confinement inside a low-index 2D dielectric waveguide using metamaterial claddings. Confining a guided wave inside a transparent low index dielectric with arbitrary cross section. The momentum transforming cladding surrounding the core leads to simultaneous total internal reflection and rapid decay of evanescent waves outside the core.	94
A.11 Deep sub-diffraction performance: Irrespective of core size made of glass, one can always achieve sub-diffraction mode lengths with access to higher index media. This is difficult at optical frequencies but can be achieved by anisotropic metamaterials at THz and microwave frequencies.	95
A.12 Comparison of (a) normalized mode area and (b) power inside the core fraction for the glass 2D waveguide with and without cladding versus core radius. The cladding permittivity in tangential and longitudinal direction is 1 and 20, respectively. It is seen that the metamaterial cladding decreases the mode area and also causes the power in the core to increase.	95
A.13 The normalized magnetic field amplitude of the first (a) even (b) odd TM mode of coupled silicon slab waveguides with the slab size of 0.1λ and center-to-center separation of 0.5λ for silica (dashed red lines) and germanium-silica multilayer (solid blue lines) cladding with effective permittivity of $\varepsilon_x=4.8$ and $\varepsilon_z=11.9$	96
A.14 (a) Simulation results of the tangential electric field for even (up) and odd (bottom) modes of the coupled silicon waveguides. The core size is 0.1λ and center-to-center separation of 0.5λ . The required anisotropic all-dielectric response can be obtained using a germanium/silica multilayer with germanium fill fraction of 0.6. The inset shows the fields when the cladding is bulk silica. Note that the fields at the midpoint of the waveguide is significantly decreased with the TCW, a necessary condition for low cross talk. The coupling length of the structure with silica cladding is only 6λ , but it becomes more than 132λ with the metamaterial cladding. The power fraction inside the core also increases from 25% to 45%. (b) The simulation results of symmetric (up) and antisymmetric (bottom) modes for the practical structure with germanium/silica multilayer cladding and a unit cell size of 40 nm. The fields show good correspondence with the effective medium approximation and the coupling length is 119λ	98
A.15 Normalized coupling length versus the cladding size. The core is silicon ($n = 3.47$) with a size of 0.1λ and center to center separation of 0.5λ . When the cladding is anisotropic ($\varepsilon_x = 4.8$ and $\varepsilon_z = 11.9$) the coupling length is much larger than that when the cladding is isotropic ($\varepsilon = 4.8$). The waveguides are surrounded by glass.	99

Figure	Page
A.16 Role of core index, core size, cladding anisotropy and cladding size. (a) Comparing power confinement in the slab waveguide with anisotropic cladding ($\varepsilon_x = 1.1$ and $\varepsilon_z = 20$) as opposed to isotropic cladding. The core size is $a=0.1\lambda$ and the cladding size is three-times bigger than the core. It is seen that the power confinement in the core can be larger for the TCW even for high index cores. (b) Coupling length in the slab waveguide with anisotropic cladding ($\varepsilon_x = 1.1$ and $\varepsilon_z = 20$) is two orders of magnitude larger when compared to the isotropic cladding. The center-to-center separation of the coupled waveguides is $s = 0.5\lambda$. The cladding size is three-times bigger than the core surrounded by air. The core size is $a = 0.1\lambda$	101
B.1 Comparison of the field profile for the p-polarized electromagnetic wave propagation through an Si/SiO ₂ multilayer anisotropic metamaterial below (top) and above (bottom) the critical angle ($\theta_c = 32.33^\circ$). For both cases, $\Lambda = 100$ nm and $\rho = 0.5$. It is seen that incident light is totally reflected although the total thickness of the metamaterial layer ($t = 500$ nm) is subwavelength ($\lambda = 1550$ nm).	105
B.2 Effect of the cladding periodicity on 1D e-skid waveguides. The comparison of the x-component of the electric field at $\lambda=1550$ nm. The core is silicon with a size of 100 nm. The cladding is Si/SiO ₂ multilayer with $\rho = 0.5$. (a) The periodicity is $\Lambda=10$ nm. (b) The periodicity is $\Lambda=30$ nm. (c) The periodicity linearly varies from $\Lambda=20$ nm to $\Lambda=45$ nm. The total thickness of the waveguide in all cases is 400 nm. The modal effective index (n_{eff}) for the three cases are 1.9062, 1.8864, and 1.8864, respectively. The ratio between the power confined inside the core and total power (η) for the three cases are 30.98%, 29.79%, and 29.99%, respectively. $n_{\text{eff}}=1.5281$ and $\eta=12.36\%$ when the cladding is removed. It is clearly seen that as long as the periodicity is subwavelength, the performance of e-skid waveguide depends on the effective permittivity of the multilayer cladding not the periodicity or disorder in the cladding. Thus the waveguiding mechanism in e-skid waveguides is fundamentally different from that in photonic crystal waveguides.	106
B.3 Effect of the cladding periodicity on the modal index.	107

Figure	Page
<p>B.4 Measured transmission spectra to the through and coupled waveguides. a, Strip waveguide; b, e-skid waveguide. (Inset) Schematic representation of the experimental setup to measure the coupling length. Light is in-coupled through the middle grating coupler. The waveguide core size and the coupling distance (L) is 450 nm and 140 nm, respectively, in both cases. The other parameters of the waveguides are the same as the waveguides in Fig. 4 in the main text. The anisotropic cladding causes coupling to the second waveguide to drop almost 20 dB. This helps to reduce the cross-talk in dense photonic integrated circuits.</p>	108
<p>B.5 Normalized coupling length (L_c/λ) versus the center-to-center separation between the coupled waveguides (s). $w_0 = 450$ nm, $\Lambda = 100$ nm, and $\rho = 0.5$. Other simulation parameters are the same as those in Fig. 3 in the main text. $L_c = 1$ cm has been defined as the minimum decoupling length. In this case, the minimal separation length (center-to-center) in e-skid waveguides and strip waveguides are 1104 nm and 1466 nm, respectively. This shows that e-skid waveguides will have higher performance for dense photonic integration than strip waveguides.</p>	109
<p>B.6 Effect of cladding anisotropy on the coupling length for TE-like and TM-like modes of e-skid waveguides. a, Schematic representation of the two coupled Si waveguides with a core size of 300 nm, height of 220 nm, and center-to-center separation of 1000 nm operating at $\lambda = 1550$ nm. The waveguides have been covered by a homogeneous anisotropic metamaterial (yellow) with $\varepsilon_x = 2$ and $\varepsilon_y = \varepsilon_z$. b, Coupling length for TE-like mode versus ε_z. c, Coupling length for TM-like mode versus ε_z. As we enhance the anisotropy of the cladding, the coupling length of TE-like mode increases as a result of skin-depth reduction in the cladding. . .</p>	110

- B.7 E-skid waveguides for controlling the evanescent waves of the TM-like mode.** **a**, The schematic representation of proposed e-skid waveguides for controlling the skin-depth of the TM-like mode (inset). Since the electric field of the TM-like mode is polarized in the y direction, the cladding must be anisotropic in yz plane. To simplify the structure, the anisotropic cladding (yellow) is implemented only underneath the waveguides. The plot shows the normalized coupling length between the two waveguides versus the anisotropy of the metamaterial layer while the permittivity in the y direction is fixed to be 2.2. The thickness of the layer is 120 nm. The waveguide parameters are the same as that in Fig. B.6. **b**, Practical Si/SiO₂ multilayer structure to confine the evanescent waves and reduce the cross-talk between the two waveguides. $\Lambda = 40$ nm and the silicon filling fraction is $\rho = 0.5$. **c** and **d**, The normalized electric field profile of the even mode of the coupled strip and e-skid waveguides, respectively. It is seen that the multilayer structure helps to confine the mode inside the waveguide and reduces the overlap between the evanescent waves of the two waveguides. This results in the increase of the coupling length from 14.5λ to 30.6λ 111
- B.8 Cross-talk in e-skid waveguides without an Upper cladding.** **a**, Schematic layout to measure the cross-talk and **b**, SEM image of coupled e-skid waveguides on an SOI platform. Geometric parameters are set to $h_0 = 220$ nm, $\Lambda = 100$ nm, $\rho = 0.5$, and $N = 5$, setting the separation distance between the two waveguides to be $d_{\text{sep}} = 550$ nm. There is no upper cladding. **c-e**, Coupling length L_c characterization by measuring the output power ratio (I_2/I_1) vs. device length L ; core widths w_0 are (**c**) 350 nm, (**d**) 400 nm, and (**e**) 450 nm, respectively. Red and blue circles are the measured power ratio for the e-skid and strip waveguides, respectively, and dashed lines are their fitting curves with $I_2/I_1 = \tan^2(\pi L/2L_c)$. **f**, Normalized coupling length (L_c/λ) for the e-skid (red circles) and strip (blue circles) waveguides. Red and blue lines are their respective simulation results. 112

Figure	Page
<p>B.9 Bending loss. a, Schematic representation of the experimental setup to measure the bending loss. Light is in-coupled through the middle grating coupler. It is divided into two branches of equal length but with a different number of bends. b, The top view SEM image of an e-skid waveguide with multiple bends. The inset shows a closer view. The bending radius is $1\ \mu\text{m}$ and the other parameters of the waveguides are the same as the waveguides in Fig. 4 in the main text. c, The comparison of bending loss between e-skid and strip waveguides at telecommunication wavelength. The experimental points are fitted by a straight line. d, The comparison of simulated and measured bending loss in e-skid and strip waveguides versus the core size indicating a considerable reduction in the bending loss, specially when the core size is small.</p>	113
<p>B.10 Full-wave simulation of the TE-like mode of curved waveguides. Full-wave simulation results of the magnetic field of the TE-like mode of curved (a) strip waveguide, (b) e-skid waveguide with $\Lambda=120\ \text{nm}$, and (c) e-skid waveguide with $\Lambda=20\ \text{nm}$. The waveguide core size and bending radius are $300\ \text{nm}$ and $1\ \mu\text{m}$, respectively. Other simulation parameters of the waveguides are the same as those in Fig. B.9. The waveguides are excited from the left side. The anisotropic cladding reduces the skin-depth in the cladding. Thus, the scattering at the bend is reduced in the e-skid waveguide case. The comparison of the field amplitude at the end of the waveguides clearly shows that the bending loss in e-skid waveguide is relatively lower. In the ideal case where the periodicity is deep subwavelength, the bending loss is considerably lower in e-skid waveguides.</p>	114
<p>B.11 Full-wave simulation of the TM-mode of curved waveguides. a, Full-wave simulation results of the magnetic field of the TM-like mode of curved e-skid waveguide with $\Lambda=120\ \text{nm}$. Other simulation parameters of the waveguides are the same as those in Fig. B.10. b, The field profile of the same waveguide when the multilayer cladding is replaced by an isotropic cladding with the same permittivity as the effective permittivity of the multilayer metamaterial in the y direction. Since the electric field of the TM-like mode is polarized in the y direction and the electric field in the x direction is negligible, the anisotropy does not play any role in confinement. Thus, the TM-like mode is similar to that of an isotropic cladding waveguide. Note the TE-like mode probes the anisotropy of the multi-layer cladding and is fundamentally different.</p>	115

- B.12 Comparison of the full-wave simulated bending loss in e-skid and strip waveguides for both TE-like and TM-like modes.** The structure is the same as in Fig. B.10. The bending loss for TE-like modes in e-skid waveguide is lower in comparison with that in strip waveguides because the multilayer cladding confines the light inside the core and reduces the skin depth in the cladding, especially when the core size is small and a considerable fraction of the total power is in the cladding. The green curve shows the bending loss for the TM-like mode when the metamaterial cladding is replaced by an isotropic cladding with the same size and the same permittivity as the effective permittivity of the multilayer metamaterial in the y direction. It is seen that the TM-like modes do not feel the anisotropy of the multilayer cladding. Thus, the anisotropic cladding cannot help to control the evanescent waves for TM-like modes. As a result, the bending loss for TM-like modes in e-skid waveguide is even worse than that in strip waveguides. 116
- B.13 Mode conversion efficiency.** **a**, The schematic representation of the experiment set-up. **b**, SEM image of an e-skid to strip waveguide transition. **c**, Measured transmission spectra of the racetrack resonators without (blue) and with (red) the metamaterial claddings, and characterized mode conversion efficiency (CE). **d** & **e**, Fitted resonances: (**d**) without (strip waveguide) and (**e**), with (e-skid waveguide) the metamaterial claddings. The waveguide geometries are set to $h_0 = 220$ nm, $w_0 = 350$ nm, $w_\rho = w(1 - \rho) = 50$ nm, and $N = 5$ 118
- B.14 Propagation losses in e-skid and strip waveguides.** The circles represent normalized transmission through straight e-skid (blue) and strip (red) waveguides at $\lambda = 1550$ nm. The length of the waveguides is varied from 0 to 1.8 mm to characterize the propagations loss (fitting curves). The propagation loss in e-skid and strip waveguide is 3.43 and 2.65 dB/cm at $\lambda = 1550$ nm, and the average losses for e-skid and strip waveguides for wavelengths between 1540 nm to 1560 nm are 3.67 dB/cm and 1.84 dB/cm, respectively, with a standard deviation of 1.0 dB/cm and 1.4 dB/cm, respectively. The other waveguide parameters are $w_0 = 450$ nm, $h_0 = 220$ nm, $w_\rho = w_{(1-\rho)} = 50$ nm, and $N = 5$. This clearly shows that e-skid waveguides have comparable losses to standard strip waveguides opening the path for practical applications. 120

ABBREVIATIONS

EMT	Effective Medium Theory
ENZ	Epsilon Near Zero
E-skid	Extreme Skin-Depth
FDTD	Finite-Difference Time-Domain
HMM	Hyperbolic Metamaterials
QP	Quasi-Particle
SEM	Scanning Electron Microscopy
SNSPD	Superconducting Nanowire Single-Photon Detector
SOI	Silicon on Insulator
TE	Transverse Electric
TEM	Transverse Electro-Magnetic
TIR	Total Internal Reflection
TM	Transfer Magnetic
TMM	Transfer Matrix Method
TO	Transformation Optics

ABSTRACT

Jahani, Saman Ph.D., Purdue University, December 2018. On-Chip Quantum Photonics: Low Mode Volumes, Nonlinearities and Nano-Scale Superconducting Detectors. Major Professor: Zubin Jacob.

Miniaturization of optical components with low power consumption fabricated using a CMOS foundry process can pave the way for dense photonic integrated circuits and on-chip quantum information processing. Optical waveguides, modulators/switches, and single-photon detectors are the key components in any photonic circuits, and miniaturizing them is challenging. This requires strong control of evanescent waves to reduce the cross-talk and bending loss as well as low mode volumes to increase light-matter interaction.

In this thesis, we propose a paradigm shift in light confinement strategy using transparent all-dielectric metamaterials. Our approach relies on controlling the optical momentum of evanescent waves, an important electromagnetic property overlooked in photonic devices. For practical applications, we experimentally demonstrate photonic skin-depth engineering on a silicon chip to confine light and to reduce the cross-talk and bending loss in a dense photonic integrated circuit.

We demonstrate that due to the strong light confinement in the proposed waveguides, it is possible to miniaturize and integrate superconducting nanowire single-photon detectors (SNSPDs) into a silicon chip. The timing jitter and dark-count rate in these miniaturized SNSPDs can be considerably reduced. Here, we propose a theoretical model to understand the fundamental limits of these nanoscale SNSPDs and the trade-off between timing jitter, dark-count, and quantum efficiency in these detectors. We propose experimental tests to verify the validity of our model.

Switching/modulating cavity Purcell factor on-chip is challenging, so we have proposed a nonlinear approach to switch Purcell factors in epsilon near zero (ENZ) materials. We demonstrate fourfold change in the Purcell factor with a switching time of 50 fs.

The work in this thesis can lead to a unique platform for on-chip quantum nanophotonics.

1. BACKGROUND AND MOTIVATION

1.1 Motivation

Quantum information processing has emerged as a new way to solve problems which are impossible to be solved with conventional computers. Recently, several platforms have been proposed to implement a quantum computer, such as superconducting circuit-QED (IBM and Google), trapped ions (IonQ), and majorana fermions (Microsoft). Although these approaches are promising, integrating with an optical interface is fundamentally necessary for efficient combination with communication systems. Hence, it would be ideal to have an optical platform to perform quantum information processing in interconnect nodes and control of flying qubits. Progress in quantum information processing at optical frequencies can be accelerated by developments in the control and manipulation of light-matter interaction at the nanoscale [1]. Some recent achievements include on-chip superconducting single photon detectors [2], spin routing of single photons [3–6], long range dipole-dipole interactions [7, 8], enhancement or suppression of vacuum fluctuations in a selected spectrum [8–19], modulation and switching of light sources [20–23], and switching at the single photon level [24–27].

The ideal materials for on-chip nanophotonic applications should have the ability to confine light with low mode volume, the ability to control the polarization of light, strong nonlinear response to switch and modulate signals, and the ability to absorb and detect a single-photon at the telecommunication wavelength. Confining light can increase the integration density, enhance light-matter interaction, improve switching light and single photon detection efficiency. However, light confinement in natural transparent dielectrics is bounded by the diffraction limit of light.

The purpose of my work has been to improve the functionality of photonic integrated circuits for on-chip quantum information processing applications. For this

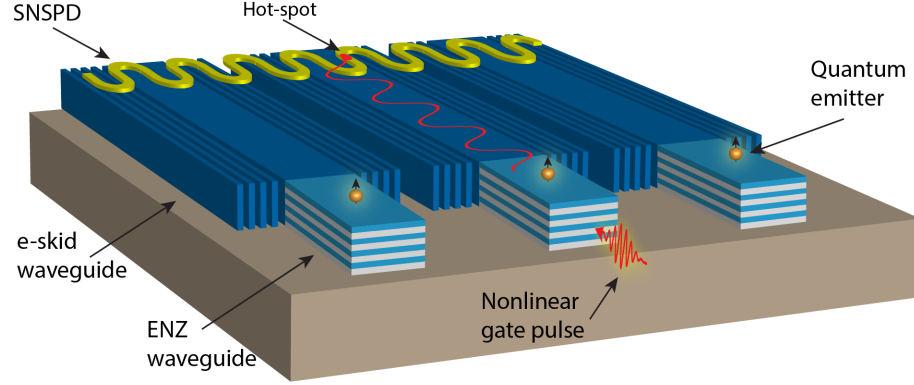


Fig. 1.1. **Platform for on-chip quantum nanophotonics.** The purpose of this study is to demonstrate some key elements for all-optical quantum information processing on a chip. We have proposed a nonlinear tunable epsilon-near-zero (ENZ) structure to enhance and to modulate decay rate of photon emissions from a quantum emitter. Emitted photons are strongly confined and guided by extreme skin-depth (e-skid) waveguides in an ultra-dense photonic integrated circuit without coupling to the adjacent waveguides or scattering at sharp bends. Since e-skid waveguides strongly confine light into a small area, the interaction of photons with a short superconducting nanowire single-photon detector (SNSPD) is enhanced. Hence, the photons are efficiently detected with a high temporal accuracy.

purpose, we need to confine light to enhance light-matter interaction. Plasmonic structures can surpass the diffraction limit of light by coupling light to the free electrons of metal, but due to the optical losses of metals, light cannot propagate more than a few microns. Here, we have proposed a new class of all-dielectric anisotropic metamaterials to engineer the skin-depth of evanescent waves. This allows us to strongly confine light and to surpass the diffraction limit. In addition to strong confinement, strong nonlinearity is needed to switch and modulate light. We have demonstrated that the nonlinearity in anisotropic ENZ media is considerably stronger than conventional dielectrics. We have shown the possibility of switching of Purcell effect around the ENZ wavelengths. Finally, for quantum information processing, it is needed to accurately detect a single-photon with high temporal resolution (low timing jitter). To understand the fundamental limit of single-photon detection at the

nanoscale, we have studied the detection mechanism of nanoscale superconducting single photon detectors. These detectors can be placed on top of our proposed e-skin waveguides to increase the light-matter interaction and hence to improve the quantum efficiency (Fig. 1.1). Before proceeding, I will provide some historical context outlining the progress have been made in the last few decades in this field and how my research contributes to the field.

1.2 Historic perspective and thesis structure

1.2.1 Sub-diffraction photonics

In 1611, Johannes Kepler, a German mathematician and astronomer, discovered the phenomenon of total internal reflection ten years before Willebrord Snell derived his famous formula for the refraction of light. It is interesting to note that 200 years lapsed before it was accidentally discovered by Daniel Colladon in 1842 that TIR can be used for light guiding. Total internal reflection (TIR) is the fundamental operating principle behind many photonic devices, such as optical dielectric waveguides [28], total internal reflection fluorescence microscopes [29] and laser cavities [30].

The emergence of nanoscale photonics led to revisiting the laws of refraction and reflection through artificially structured materials, such as chiral materials [31], negative index materials [32,33], photonic crystals [34], and bio-inspired structures [35,36]. Many interesting phenomena were observed, which are not seen in conventional dielectrics. Recent works have also shown the existence of a generalized Snell's law to control refraction and reflection of light using metasurfaces which control the phase gradient at the interface between dielectric media [37–39]. This allows the control of an optical ray with arbitrary phase, amplitude, and polarization [40–43].

However, all of these approaches deal primarily with propagating waves. In 2014, we introduced relaxed TIR to control the evanescent waves produced during TIR [44]. The skin depth of evanescent waves at TIR is the fundamental reason dielectric photonics is diffraction-limited in size. We have shown that relaxed total internal

reflection requires unique anisotropy and is achievable using lossless semiconductor building blocks. This can surprisingly lead to sub-diffraction light confinement in photonic waveguides (without using metallic components).

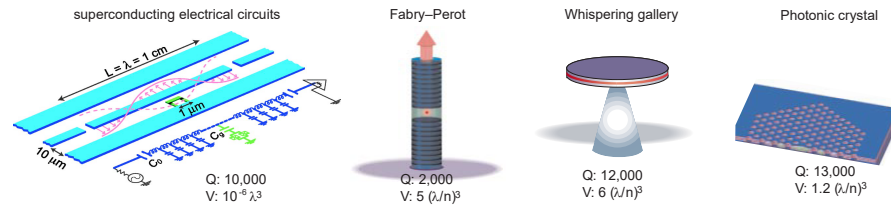


Fig. 1.2. **Mode volume in microwave and photonic structures.**

At low frequencies, metals are perfect reflectors and they can confine light to increase light matter interaction. At optical frequencies, because of the intrinsic loss of metals, light is dissipated and does not allow strong light matter interaction. Dielectric structures, such as photonic crystal cavities and microdisk resonators can confine light, but the mode volume in these dielectric structures is limited by the diffraction limit of light which impedes further confinement. Figure is reproduced from ref. [45] and ref. [11].

Light has a characteristic size set by its wavelength which is around a micron at optical communication frequencies and fundamentally impedes any effort to integrate it on current industrial standards of nanoscale circuitry (Fig. 1.2). As micron scale fibers and waveguides are made smaller, the fundamental roadblock arises since light escapes out of the core of the fiber even if the core is made from a high refractive index dielectric such as silicon [46]. This causes crosstalk between adjacent waveguides in dense photonic integrated circuits.

The search for replacement of optical fibers in photonic integrated circuits has led to the design of many photonic waveguide architectures. These waveguides can be categorized in two major classes: metallic (or plasmonic) and dielectric waveguides. Metallic waveguides are predominantly used for guiding electromagnetic waves at microwave frequencies due to the specular reflection of metals at low frequencies. However, due to the intrinsic loss of metals at optical frequencies, it is difficult to scale microwave waveguides for higher frequency applications. A number of architec-

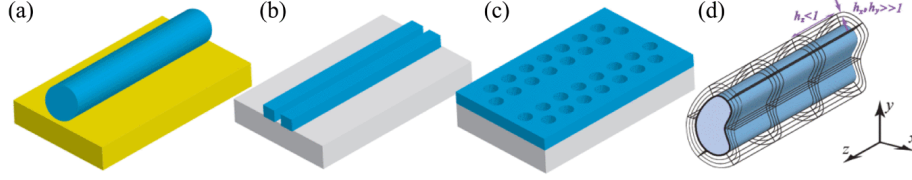


Fig. 1.3. **Various approaches to nano-waveguiding.** **a**, Hybrid plasmonic waveguide. **b**, Dielectric slot waveguide. **c**, Photonic crystal waveguide. **d**, Extreme skin depth (e-skin) waveguide.

tures have recently emerged to effectively utilize metals for waveguiding at optical frequencies. These include the long range surface plasmon polariton (SPP) on metal strip waveguides (IMI, I insulator, M metal) [47] which are useful for sensing applications but not for sub-diffraction confinement. The inverse design consisting of MIM waveguides [48], confines light to subwavelength scales but it leads to low propagation lengths. V-groove [49] and wedge [50] plasmons are excellent candidates for relatively long range propagation and sub-diffraction confinement however excitation and detection of these modes as well as interfacing with existing silicon waveguide technology are major challenges. Recently, hybrid dielectric-plasmonic waveguides (see Fig. 1.3a) [51] have emerged that confine light in a low index gap above metals reducing the field penetration in the metal thus allowing for increased propagation length. Another alternative is an epsilon-near-zero metamaterial waveguide [52] which allows modes to tunnel through subwavelength size structures. However, due to the optical losses of metals at optical frequencies, the propagation loss in the above mentioned sub-diffraction plasmonic structures is relatively high [50].

Dielectric slot-waveguides (see Fig. 1.3b) and photonic crystal waveguides (see Fig. 1.3c) are the two major all-dielectric architectures which are able to strongly confine light. In slot waveguides, the electric field intensity goes up in a small low index gap surrounded by two high index rods. This allows sub-diffraction confinement of the mode inside the gap [53, 54]. Photonic crystal waveguides can contain and confine light in defects in the designed photonic band gap. If there is no disorder,

light cannot escape from the core even at sharp bends [55]. However, in both of these structures, if two waveguides are fabricated close to each other, light can easily be coupled to the adjacent waveguide. Thus it causes considerable cross talk in photonic integrated circuits [56]. In Chapter 2 and 3, we propose a new class of transparent anisotropic claddings to reduce skin depth using relaxed-TIR rules. Reducing the skin depth of the cladding can lead to sub-diffraction confinement of the mode inside the so-called extreme skin depth (e-skid) waveguide (see Fig. 1.3d). This is contrary to years of waveguide literature which claimed that transparent media cannot confine light to below the diffraction limit.

1.2.2 Nonlinear epsilon-near-zero media

Nonlinearity in conventional dielectric structures is very weak which makes the modulation and switching of light a difficult task in photonic integrated circuits. Epsilon-near-zero (ENZ) media have emerged as a promising platform in nanophotonics due to the field enhancement and quasi-static behavior of light in these media [57]. It has been shown recently that because of the low refractive index and field enhancement in these media, nonlinearity is strongly enhanced [58, 59]. In addition, it has been shown it is possible to strongly modify decay rate of a quantum emitter near an ENZ media [10, 60]. In Chapter 3, we leverage these two features of the ENZ media to switch and modulate the Purcell effect with a nonlinear pulse in ENZ media [61].

1.2.3 Single-photon detectors

Superconducting single-photon detector (SNSPD) is the most promising detector for on-chip single-photon detection at telecommunication wavelength for application such as boson sampling [62, 63] and quantum key distribution [64]. It is usually composed of a very thin (4-6 nm) and narrow (40-200 nm) superconductor which is biased with a DC current very close to the the superconducting depairing critical

current and connected to an electronic readout circuit. When a photon falls on the nanowire, if the photon has enough energy, a phase transition is triggered and a voltage pulse is generated which is amplified and detected by the readout circuit.

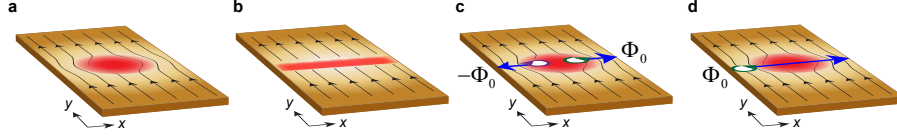


Fig. 1.4. **Schematic representation of main detection models for superconducting nanowire single photon detectors (SNSPDs).** **a**, Hot-spot model. **b**, Quasi-particle (QP) diffusion model. **c**, Vortex-antivortex unbinding model. **d**, Single-vortex crossing model.

Despite the experimental advancements in SNSPDs [65], the fundamental mechanism of the single-photon detection is poorly understood [66]. Over the past two decades, several detection models have been proposed to explain the formation of the first normal conducting region in SNSPDs (Fig. 1.4). The earliest and the simplest model to explain the detection mechanism is hot-spot model. In this model, it is assumed that the photon absorption causes the formation of a normal conducting hot-spot at the absorption location. This results in a change in the applied bias current distribution as shown in Fig. 1.4a. If the current density around the edge goes above the critical current, a phase transition happens and the normal conducting region spreads across the width of the nanowire. This model gives a simple physical explanation, but it cannot predict most of the experimental observations [66], especially it cannot explain the detection event if the photon energy is not high enough to form a hot-spot. In quasi-particle (QP) model (Fig. 1.4b), there is no need to have a normal conducting region to trigger a phase transition. The photon absorption breaks superconducting Cooper pairs to QPs. If the Cooper pairs are depleted in a volume with a thickness greater than the coherence length of Cooper pairs, the phase coherence in superconductor is destroyed and a normal conducting belt is formed across the width.

Recently, some groups have demonstrated that vortex and antivortex can also be responsible for the click event, especially if the photon energy is very low or even if there is no photon (dark-count). Vortices are defects in a thin superconductor and they can be in a form of vortex-antivortex pairs or single-vortices. Vortices can move because of the force applied by the bias current. The movement of single vortices is dissipative and can break Cooper pairs on their way. In vortex-antivortex unbinding model (Fig. 1.4c), it is assumed that the formation of hot-spot due to the photon absorption can depair vortex-antivortex pairs and because of the bias current, the unpaired vortex and antivortex move in opposite directions and form a normal conducting belt. In a narrow superconductor there is no need to have vortex-antivortex in pairs. Even single vortices can be thermally excited and enter the nanowire from the edge. However, there is a vortex potential barrier which does not allow them to move. A change in the current distribution due to the photon absorption can reduce the potential barrier. Hence, vortices can escape the barrier and move to the other edge. This process releases enough energy to see an observable voltage pulse at the output (Fig. 1.4d).

Although each of these models can explain some experimental observations at specific wavelengths, they fail to predict the SNSPD response for a broad range of wavelengths and bias currents as well as the trade-space in SNSPDs and material and design parameters to improve the efficiency and temporal resolution of the click events. In Chapter 4, we propose a new detection model which can depict some recent experimental observations [67, 68]. Our model demonstrates the trade-off between quantum efficiency, timing jitter, and dark-count in different class of SNSPDs for a wide range of wavelengths [69]. This model can predict the functionality of nanoscale SNSPDs integrated onto a photonic chip.

2. TRANSPARENT SUBDIFFRACTION OPTICS: NANOSCALE LIGHT CONFINEMENT WITHOUT METAL

We introduce a paradigm shift in light confinement strategy to overcome the size limitation on conventional optical devices imposed by the wave nature of light. Contrary to popular assumption, we show that light can be confined below the diffraction limit using completely transparent artificial media (metamaterials with $\varepsilon_{ij} > 1$, $\mu_{ij} = 1$). Our approach relies on controlling the optical momentum of evanescent waves, an important electromagnetic property overlooked in photonic devices. For practical applications, we propose a class of waveguides using this approach that outperforms the cross-talk performance by an order of magnitude as compared to any existing photonic structure. Our work overcomes a critical stumbling block for nanophotonics by completely averting the use of metals and can impact electromagnetic devices from the visible to microwave frequency ranges.

2.1 Outline of the problem

Modern computation and communication systems rely on the ability to route and transfer information using electronic and electromagnetic signals. Massive efforts over the last decade have been driven by miniaturization and integration of electronics and photonics on the same platform [70]. However, the diffraction limit of light is a fundamental barrier to interface micron scale waveguides to nanoscale electronic circuitry. Furthermore, dense photonic integration is hampered because crosstalk between waveguides increases as the separation between them is reduced.

At low frequencies, metals due to their high reflectivity can be used for confining light at the subwavelength scale. At optical frequencies, metals can achieve the same

task by coupling light to free electrons. This leads to a surface plasmon polariton (SPP) which shows properties of nanoscale waveguiding [50, 71]. However, due to absorption in metals this approach cannot guide light more than a few microns [50, 51, 72]. Furthermore, the dissipated energy leads to thermal issues which are especially significant in miniaturized circuits hindering dense photonic integration. Hence, low loss approaches to light confinement at the nanoscale are a fundamental necessity for photonics.

Prevalent all-dielectric nanophotonic approaches can be classified according to two fundamental principles governing them. One which utilizes the large index contrast between media to confine light within nanoscale slots [53, 73, 74] and the other which uses bragg reflection of waves in the bandgap of photonic crystals [34, 55, 75, 76]. However, neither of the approaches functions on the evanescent fields outside the core of the resonator or waveguide. These unchecked evanescent waves are the fundamental origin of cross-talk in nanophotonics and this significantly limits the ability of these classes of dielectric waveguides for photonic integration [56, 77].

In this chapter, we surpass the diffraction limit of light by a new class of all-dielectric artificial materials that are lossless. This overcomes one of the fundamental challenges of light confinement in metamaterials and plasmonics: metallic loss. Our approach relies on controlling the optical momentum of evanescent waves as opposed to conventional photonic devices which manipulate propagating waves. This leads to a counterintuitive confinement strategy for electromagnetic waves across the entire spectrum. Finally, we propose a class of practically achievable waveguides based on these momentum transformations that exhibit dramatically reduced cross talk compared to any dielectric waveguide (slot, photonic crystal and conventional).

2.2 Paradigm shift in light confinement strategy

We introduce two distinct photonic design principles that can ideally lead to sub-diffraction light confinement without metal.

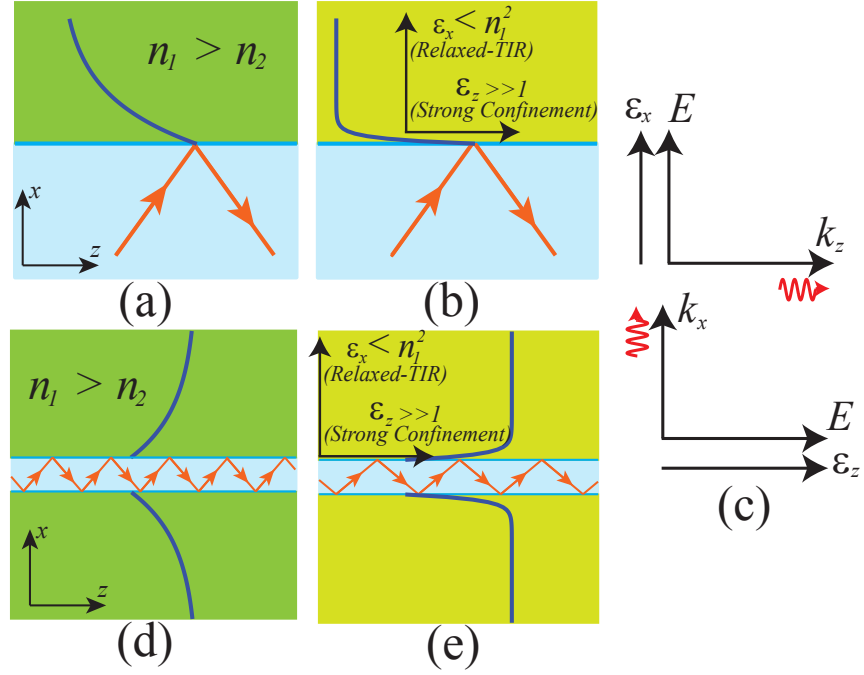


Fig. 2.1. **Relaxed total internal reflection.** **a**, Conventional total internal reflection: If $n_1 > n_2$ and the incident angle is larger than the critical angle, the light is totally reflected to the 1st medium and decays in the 2nd medium. **b**, Relaxed total internal reflection: If $n_1 > \sqrt{\epsilon_x}$ and the incident angle is larger than the critical angle, the light is totally reflected. However, the penetration depth can be decreased considerably if $\epsilon_z \gg 1$. **c**, Wave propagation along the optical axis of a uniaxial medium. As the electric field is perpendicular to the momentum direction, permittivity in specific direction controls the momentum in the perpendicular direction. **d**, Conventional waveguide based on total internal reflection: As the core size is decreased, most of the power lies outside and decays slowly in the cladding. **e**, Transformed cladding waveguide: Relaxed total internal reflection ($n_1 > \sqrt{\epsilon_x}$) preserves the conventional waveguiding mechanism. Furthermore, the light decays fast in the cladding as the optical momentum in the cladding is transformed using anisotropy ($\epsilon_z \gg 1$). Thus the wave can be confined inside the core giving rise to sub-diffraction optics with completely transparent media.

2.2.1 Relaxed-Total Internal Reflection

First, we revisit the conventional light confinement mechanism of total internal reflection that is widely utilized for waveguides and resonators. We consider a simple 2D case with an interface along the z-axis between medium 1 and 2 and TM polarized incident light. A habitual prejudice immediately leads us to conclude that $n_1 > n_2$ as a condition for total internal reflection of light moving from medium 1 to 2 (Fig. 2.1a). Here, we argue that the above is a sufficient but not necessary condition and the requirement can be relaxed to

$$n_1 > \sqrt{\varepsilon_x} \quad (2.1)$$

where the z-axis is parallel to the interface and the x-axis is normal to it. Note that ε_x is defined as the dielectric constant of medium 2 perpendicular to the interface. We call this condition relaxed-Total Internal Reflection. We provide a simple proof of this using momentum conservation of light parallel to the interface in uniaxial anisotropic media. The tangential momentum of light $k_z^{\parallel} = n_1 k_0 \sin \theta$ is conserved along the interface where $k_0 = \omega/c = 2\pi/\lambda$ is the free space wavevector of light and θ is the angle of incidence. Once the light enters the medium 2, even though the parallel momentum is conserved, the dispersion relation of TM polarized waves changes to

$$\frac{(k_z^{\parallel})^2}{\varepsilon_x} + \frac{(k_x^{\perp})^2}{\varepsilon_z} = (k_0)^2 \quad (2.2)$$

We see that the perpendicular component of the wavevector in the second medium k_x^{\perp} can be zero or imaginary (evanescent wave) if $k_z^{\parallel} > \sqrt{\varepsilon_x} k_0$ i.e. $n_1 > \sqrt{\varepsilon_x}$. Note that as expected, for angles of incidence greater than the critical angle of relaxed-TIR ($\theta_c = \sin^{-1}(\sqrt{\varepsilon_x}/n_1)$) we have an evanescent wave decaying into medium 2.

2.2.2 Transforming optical momentum

In conventional TIR, the evanescent wave penetrates considerably into medium 2. Here, we show how to transform the optical momentum of evanescent waves leading to a reduced penetration depth in medium 2 after TIR. The argument in the previous

sub-section about relaxed-TIR opens up a fundamentally new degree of freedom for confining evanescent waves penetrating in medium 2: the component of the dielectric tensor parallel to the interface. The evanescent wave decay constant for TM polarized waves in medium 2 is given by

$$k_x^\perp = \sqrt{\frac{\varepsilon_z}{\varepsilon_x}} \sqrt{\varepsilon_x (k_0)^2 - (k_z^\parallel)^2} \quad (2.3)$$

The penetration depth of evanescent fields into the second medium is thus governed by the ratio of permittivity components $\sqrt{\varepsilon_z/\varepsilon_x}$. We thus arrive at the condition $\varepsilon_z \gg 1$ to increase the momentum of evanescent waves i.e. make them decay faster confining them very close to the interface. Note that since we have decoupled the total internal reflection criterion ($n_1 > \sqrt{\varepsilon_x}$) from the momentum confinement condition ($\varepsilon_z \gg 1$) both can be simultaneously achieved leading to a fundamentally new approach to light confinement in transparent media (Fig. 2.1b).

2.2.3 Controlling optical momentum with dielectric anisotropy

In essence, our non-resonant transparent medium alters the momentum of light entering it. The upper limit to the momentum tangential to the interface is set by the dielectric constant perpendicular to the interface while the perpendicular momentum is increased by the dielectric constant parallel to the interface. This non-intuitive concept of controlling wave momentum in a given direction by the dielectric constant perpendicular to the phase propagation is depicted in Fig. 2.1c It is seen that for plane wave propagation along the symmetry axes of anisotropic media, the field direction and the relevant dielectric tensor component are perpendicular to the wavevector. (k_x governed by ε_z and k_z governed by ε_x).

2.3 Sub-diffraction light confinement without metal

We now show how the previous momentum transformations can be used for sub-diffraction confinement of light without metallic plasmons. Note that our approach

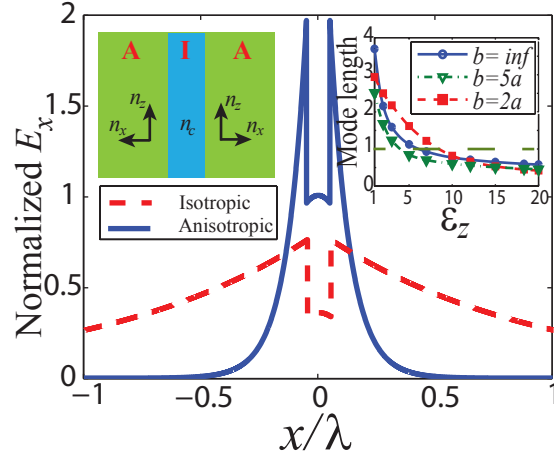


Fig. 2.2. **Subdiffraction light confinement without metal.** Normalized tangential electric field of the TM mode for a glass slab waveguide with a size of 0.1λ surrounded with all-dielectric metamaterial cladding. The metamaterial has dielectric constants of ($\epsilon_x = 1.1$ and $\epsilon_z = 15$). On comparison with a conventional mode which has air as the surrounding medium, a rapid decay of the evanescent fields is observed. The plots are normalized to the same input electric energy. (inset) As the anisotropy of the cladding is increased the mode length decreases significantly below the diffraction limit with completely transparent media. This can be achieved with a cladding size (width b), three times that of the core (width a)

can be applied to multiple devices across the visible, THz and microwave regimes but for the sake of elucidation, we consider a waveguide geometry.

As the core size of a conventional slab waveguide is decreased, all modes are cut-off except the lowest order TE and TM modes. Even though these modes exist, most of the power actually lies outside the core and decays very slowly in air (cladding). We propose to use metamaterial claddings which transform the momentum of evanescent waves and confine the light within the core of the waveguide (Fig. 2.1d and e). We call such waveguides as transformed cladding waveguides. We emphasize the counter-intuitive nature of the waveguiding since the index of the cladding averaged over all directions is greater than that of the core. The relaxed-TIR condition still allows the

lowest order mode to propagate similar in principle to the conventional case. Note that the confinement is achieved for the TM_0 mode since the dispersion relation is anisotropic only for TM waves.

In Fig. 2.2, we show the field plots for the fundamental mode in a conventional waveguide and a 1D transformed cladding waveguide. This engineered anisotropy allows us to control the evanescent field outside the core. For the same input energy, we note the increased power in the core and striking difference between the evanescent decay in the cladding for the two waveguides.

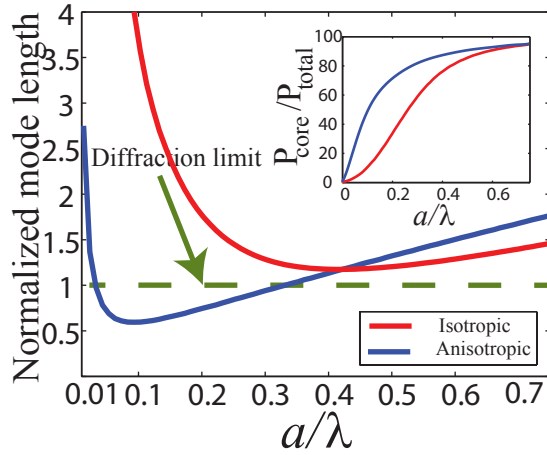


Fig. 2.3. **Mode length comparison of slab waveguides with core size.** It shows that the anisotropic cladding ($\varepsilon_x = 1.1$ and $\varepsilon_z = 15$) can confine the TM mode to sub-diffraction values. (inset) We emphasize that the net power in the core is also higher for the TCW as compared to conventional waveguides.

We follow the conventional definition of mode length adopted from the concept of mode volume in quantum optics and widely used in nanoscale waveguide theory [51, 78]. For the lowest order TM_0 waveguide mode it is given by $L_m = \int_{-\infty}^{\infty} W(x) dx / \max\{W(x)\}$, where $W(x)$ is the energy density of the mode [51, 78]. It is clear from the inset of Fig. 2.2 that the mode length is diffraction limited (above $\lambda/2n_{\text{core}}$) for conventional waveguides. However, once the cladding is made

anisotropic, the mode length achieves sub-diffraction values. We plot the role of the component of the dielectric tensor (ε_z) which is responsible for confining the evanescent waves. The increase of this constant helps to compress the evanescent waves in the cladding decreasing the mode length below the diffraction limit when the index crosses $n_z = \sqrt{\varepsilon_z} \approx 3$. We emphasize that this is within reach at optical communication wavelengths. The anisotropic metamaterial cladding also achieves a significantly better power confinement in the core as compared to the conventional waveguide (Fig. 2.3 (inset)). This increase in power confinement is accompanied by a proportionate decrease in mode length as compared to the conventional waveguide. For any given core irrespective of its subwavelength size, we can achieve sub-diffraction confinement of light and extreme power concentration in the core if the cladding anisotropy is increased. Note the diffraction limit is defined as per convention with respect to the core index where most of the power is confined. This shows that optical mode volumes can also be governed by the index felt by the evanescent fields outside of the core.

The optimum performance occurs when $\varepsilon_x \rightarrow 1^+$ and $\varepsilon_z \gg 1$. In the supplementary information we show a detailed study that the cladding anisotropy and cladding size are degrees of freedom that can be exploited to confine the mode irrespective of core index and core size.

We have decoupled the momentum of the propagating mode in the core (related to effective mode index) from the momentum of the evanescent wave in the cladding (related to confinement). This implies that the enhanced confinement does not require a high effective mode index contrary to conventional approaches. We expect this fundamental difference to be a major design advantage for mode-matching in various devices and couplers.

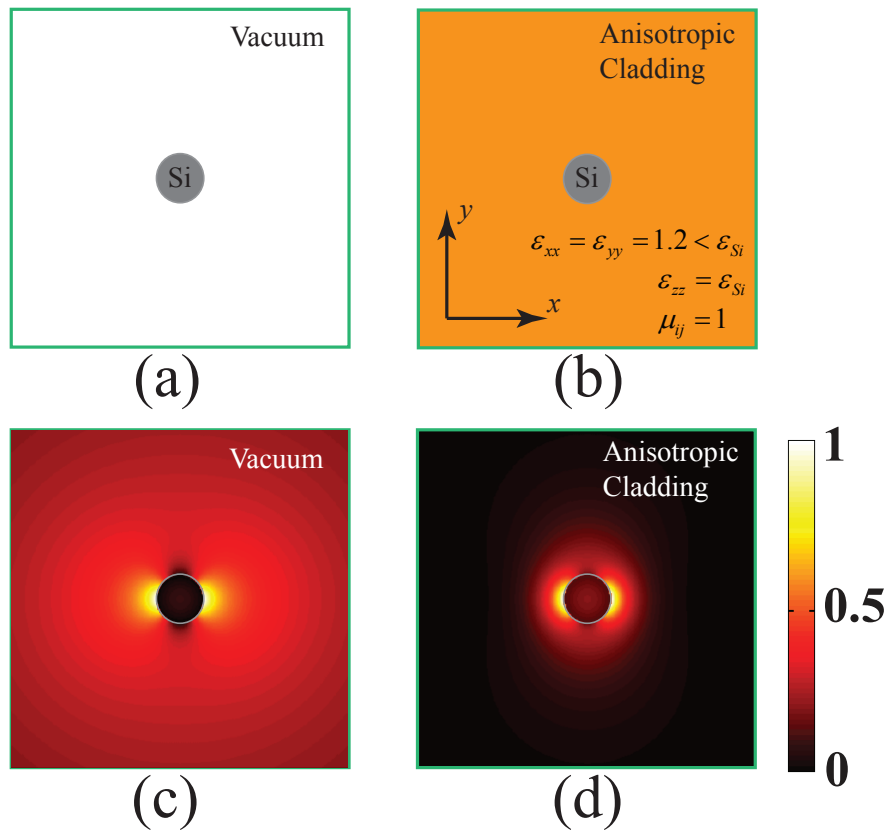


Fig. 2.4. **Is the transparent anisotropic cladding better than vacuum cladding for confinement?** (a) It is known that a silicon waveguide in vacuum is the best waveguide for low loss power confinement at optical frequencies. (b) However, we conclusively prove that if the cladding is strongly anisotropic, light confinement can be increased substantially. (c) The x-component of the electric field of HE_{11} mode for silicon waveguide in vacuum. The core radius is $r = 0.07\lambda$. Less than 2% of the power is confined inside the silicon core. (d) The x-component of the electric field of HE_{11} mode for the same waveguide surrounded by an anisotropic cladding ($\epsilon_x = \epsilon_x = 1.2 < \epsilon_{Si}$ and $\epsilon_z = \epsilon_{Si} = 12$). The cladding helps to confine up to 30% of the total power inside the core.

2.4 Better than vacuum?

It is commonly believed that to confine light inside dielectric waveguides, we should increase the contrast between indices of the core and the surrounding medium.

At optical communication wavelengths, silicon has one of the highest refractive indices among lossless dielectrics. Thus it is widely accepted that a silicon waveguide in vacuum can confine light better than any other lossless waveguide (Fig. 2.4a). However, if we cover the silicon core with a transparent anisotropic dielectric as demonstrated in Fig. 2.4b, the waveguide can confine the first HE mode better than the conventional waveguide. To satisfy relaxed-TIR condition, we must have $\varepsilon_x = \varepsilon_y < \varepsilon_{Si}$ and for strong confinement, ε_z should be as large as possible ($\varepsilon_z = \varepsilon_{Si}$ in this case). The x component of the electric field of the two waveguides is compared in Fig. 2.4c and d. It is seen that the transparent anisotropic cladding outperforms the vacuum cladding waveguide by a factor of 15 in terms of the mode area. The radius of silicon core for the both waveguides is the same ($r = 0.07\lambda$). The anisotropic cladding causes increased power confinement from below 2% to 30%.

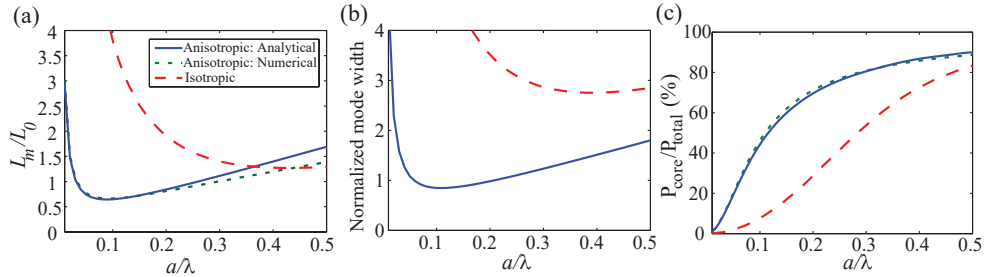


Fig. 2.5. **Figures of merit for 1D e-skid waveguides.** (a) mode length, (b) mode width, and (c) power confinement. The core is glass. The isotropic cladding is air and the anisotropic cladding has a permittivity of $\varepsilon_x = 1.2$ and $\varepsilon_z = 15$.

2.5 Figures of merit

We use three figures of merit for measuring confinement in 1D e-skid waveguides: mode length, power in the core, and mode width. Here, we show that if the core size is smaller than the skin depth, the confinement in all figures of merit is proportional to the skin depth in the cladding ($\delta_{\text{cladding}} = 1/k_{2x}$), where k_{2x} is the decay constant

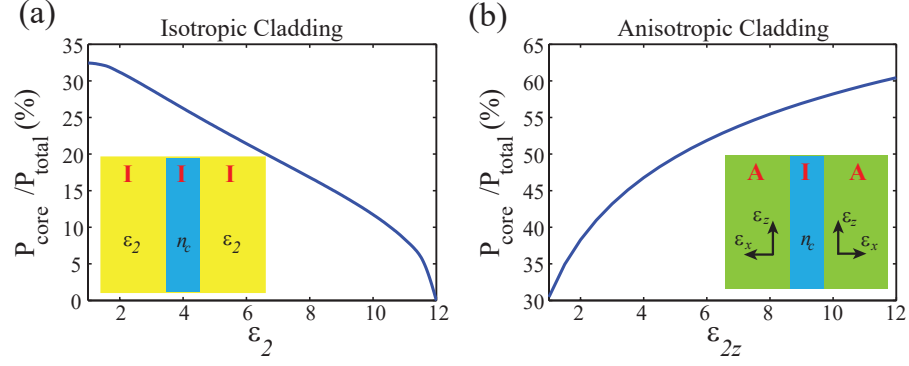


Fig. 2.6. **Power confinement versus cladding index.** The core is silicon ($\epsilon_c = n_c^2 = 12$) with a size of 200 nm operating at $\lambda = 1550\text{nm}$. (a) The cladding is isotropic. If the contrast between the core and cladding index increases, a larger fraction of the total power is confined inside the core. (b) The cladding is anisotropic with $\epsilon_x = 1.2$. As the anisotropy of the cladding is enhanced, more power is confined inside the core. Thus the conventional waveguide and e-skid waveguide show fundamentally different behavior with increasing cladding index. The power is defined through the electromagnetic energy density defined in Appendix B and can be obtained by solving for the fields of a slab waveguide with anisotropic cladding.

of the first TM mode in the cladding. These three FOMs clearly show that e-skid waveguides exhibit a larger confinement than conventional waveguides.

2.5.1 Mode-length

Mode length is derived from the concept of mode volume in quantum optics for 1D structures. It is commonly used for plasmonics and slot waveguides. Mode length is defined as the ratio of the total mode energy and mode energy density peak [51] as $L_m = \int_{-\infty}^{\infty} W(x)dx / \max\{W(x)\}$, where $W(x)$ is the time-averaged electromagnetic energy density. If $k_0a \ll 1$, the mode length can be approximated as:

$$L_m \cong \frac{2\delta_{cladding} + a(1 + \epsilon_{2x}/\epsilon_1)}{1 + \epsilon_{2x}/\epsilon_1} \quad (2.4)$$

The mode length for an e-skid waveguide with glass core and anisotropic cladding of $\epsilon_x = 1.2$ and $\epsilon_z = 15$ is plotted in Fig. 2.5a in comparison with a conventional glass

slab waveguide and air cladding. The mode length is normalized to the diffraction limit of light in the core ($\lambda/2n_{core}$). It is clearly seen that the diffraction limit is surpassed due to the extremely small skin depth in the anisotropic cladding. The numerical calculation of the mode length for the e-skid waveguide is also plotted and there is an excellent agreement with the analytical calculations when the core size is small enough. If the core size is smaller than the skin depth, the second term in the numerator vanishes and the mode length becomes proportional to the skin depth.

2.5.2 Mode-width

Although the mode length is a good measure of confinement for comparing waveguides with similar field profiles, it is not a fair figure of merit to compare different classes of waveguides, since mode length strongly depends on the peak energy density. If the field profile is not uniform, the mode length does not give any information about the size of the mode. For example, in slot-waveguides the energy density peaks in a very tiny gap surrounded by high index dielectrics, so the mode length for slot-waveguides achieves sub-diffraction values ($L_m \sim 0.1\lambda/2n_{core}$). However, the mode decays very slowly outside. Thus it cannot be used in dense photonic integrated circuits due to the cross-talk. Berini [79] has defined mode width as a measure of confinement for applications where the size of the mode is important, e.g. photonic integration. Mode width is the width at which the field intensity falls to $1/e$ of the maximum field intensity:

$$\delta_w = a + 2/k_{2x} = a + 2\delta_{cladding} \quad (2.5)$$

If the skin depth reduces, the mode decays faster in the cladding and the mode width decreases. The mode width of the e-skid waveguide is compared with the conventional slab waveguide in Fig. 2.5b. The results are normalized to the diffraction limit of light in glass. E-skid waveguides have a smaller mode width and can surpass the diffraction limit.

2.5.3 Power in the core

Another figure of merit for confinement is the fraction of power in the core. An ideal confinement is when all of the power is in the core area and the cladding carries no power. If $k_0 a \ll 1$, the ratio of power in the core and power in the cladding can be approximated as:

$$\frac{P_{core}}{P_{cladding}} \cong \frac{a}{2\delta_{cladding}} \left(1 + \frac{\varepsilon_{2x}}{\varepsilon_1} \right) \quad (2.6)$$

As the skin depth decreases, a larger fraction of the total power is confined inside the core. The ratio of power in the core and total power (in percent) is plotted in Fig. 2.5c for the e-skid waveguide and slab waveguide. The numerical calculation of the power is also plotted for comparison and an excellent agreement is observed.

As it is shown in Fig. 2.6, if we decrease the contrast between the core and cladding indices of a conventional slab waveguide, the power confined in the core is significantly lower. However, if we increase the cladding index only in the z direction, we can enhance the confinement. Note that ε_{2z} can even be larger than ε_1 .

2.6 1D Practical Realization

We discuss how to practically achieve these momentum transformations. Firstly, we argue that no naturally occurring medium has a strong anisotropy and the maximum contrast between permittivity tensor components is low for natural dielectrics (e.g. TiO_2) as well as artificial polymers [80]. Thus we cannot use natural dielectrics to preserve total internal reflection with a glass or silicon waveguide core interface while simultaneously increasing the momentum of evanescent waves. However, we can realize this extreme anisotropy by artificially structured media using available lossless dielectrics.

One practical approach consists of a multilayer structure consisting of two materials with a high index contrast and layer thicknesses far below the wavelength of light [81]. Effective medium theory for this super-lattice predicts a homogenized

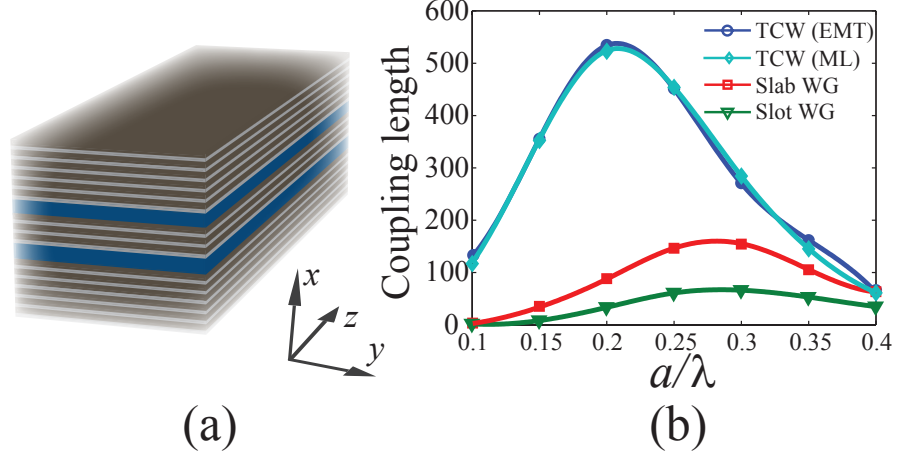


Fig. 2.7. **Dense photonic integration at optical telecommunication wavelength** ($\lambda = 1550nm$). **a**, The transformed cladding with low cross-talk between closely spaced waveguides. This can be achieved by surrounding the waveguide cores (blue) with multilayer all-dielectric metamaterials. The multilayer metamaterial consisting of alternating sub-wavelength layers Germanium (26 nm) and Silica (14 nm). This all-dielectric structure achieves the anisotropy of ($\epsilon_x = 4.8$ and $\epsilon_z = 11.9$) **b**, Comparison of coupling length (cross-talk) for conventional slab waveguides, slot waveguides and transformed cladding waveguides. It is seen that the TCW improves the cross-talk by an order of magnitude and the practical multilayer structure result is in excellent agreement with the effectively anisotropic cladding. The core is silicon with a center to center separation of 0.5λ between waveguides. Each slot-waveguide has the same net size as the core of the other waveguides, the slot size is 0.01λ and is filled with glass. If the slot size is larger or the slot index is lower, the cross talk performance is worse than that shown above. Also note that the slot waveguide cross-talk is in fact always more than the conventional waveguide.

medium with an anisotropic dielectric tensor given by $\epsilon_{\parallel} = \epsilon_{high}\rho + \epsilon_{low}(1 - \rho)$ where ϵ_{\parallel} is the dielectric constant parallel to the layers and $1/\epsilon_{\perp} = \rho/\epsilon_{high} + (1 - \rho)/\epsilon_{low}$ is the dielectric constant perpendicular to the layers. ρ is the fill fraction of the high index material ϵ_{high} .

2.7 Application to Photonic integration

The major advantage of our approach for practical applications is the reduction in cross-talk once the metamaterial is introduced in the region between any conventional dielectric waveguides. This is because our approach relies on altering the evanescent field outside the core for confinement, the fundamental origin of cross-talk. This is a key figure of merit for photonic integration [82] and we outperform state of the art structures by an order of magnitude taking into account non-idealities.

Fig. 2.7a shows schematic for two coupled slab waveguides where the cladding has been transformed to allow total internal reflection but cause fast decay of evanescent waves in the cladding to reduce the cross-talk. We consider two silicon slab waveguides ($n_{Si} = 3.47$) with a center-to-center separation of $s = 0.5\lambda$. A periodic multilayer combination of a high-index and low-index dielectric shows extreme effective anisotropy needed for the optical momentum transformation. The metamaterial claddings are made of high index ($n_1 = 4.3$) and low index thin films ($n_2 = 1.5$) at the operating wavelength of 1550 nm. Two representative materials with such indices are Germanium and Silica. We emphasize that the band edge loss at 1.55 microns in Germanium is not a fundamental impediment. For a medium 1 filling fraction of $\rho = 0.6$, multilayer effective medium theory predicts anisotropic dielectric constants of $\varepsilon_x = 4.8$ and $\varepsilon_z = 11.9$. Fig. 2.7b shows the coupling length of the fundamental mode in the waveguide with increasing core-size. For comparison, we also show the coupling length when the surrounding medium is simply silica. A dramatic impact of the anisotropy is clearly evident in the coupling length which shows an order of magnitude increase for various core sizes for the transformed cladding structure. For completeness, we have also compared the cross talk performance of our waveguide with another state of the art structure slot waveguides [53, 56]. Higher index cores in slot waveguides and photonic crystals can lead to enhanced power confinement however the cross-talk of our extreme skin-depth waveguides always outperforms them by an order of magnitude.

The anisotropic cladding can be exploited for designing bends and splitters as well. The dielectric constant of the cladding perpendicular to the core governs total internal reflection and can be minimized or altered to decrease power loss. A detailed analysis of quasi-2D waveguides, splitters and bends with transformed claddings and their performance will be presented in the next chapter but we now focus on showing how our approach can be generalized to 2D waveguides.

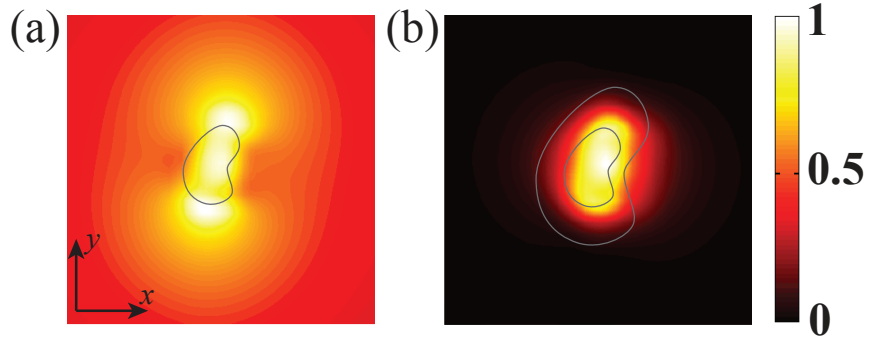


Fig. 2.8. **2D extreme skin-depth waveguides.** **a**, Simulated distribution of the electric energy density inside a low-index 2D dielectric waveguide with arbitrary cross section using metamaterial claddings. **a**, The waveguide without cladding, **b**, the waveguide with all-dielectric non-magnetic cladding ($\varepsilon_x = \varepsilon_y = 1.2$ and $\varepsilon_z = 15$). When the anisotropic cladding is added, the mode area of the waveguide is decreased from about $80A_0$ to $0.7A_0$, and the fraction of power inside the core to the total power is increased from less than 1% to about 36%.

2.8 2D Extreme Skin-depth Waveguides

The momentum transformation can be used to strongly confine light in an infinitely long glass rod with arbitrary shaped cross section ($A \ll \lambda^2$). The cladding has to be anisotropic to allow for the lowest-order mode (HE₁₁) to travel inside the glass core and bounce off by total internal reflection but simultaneously decay away rapidly causing sub-diffraction confinement of the mode (Fig. 2.8). The set of

non-magnetic media which can cause the momentum transformation are anisotropic homogenous dielectric materials with $1 < \varepsilon_x = \varepsilon_y < \varepsilon_{glass}$ and $\varepsilon_z \gg 1$.

The simulated electric energy density of the arbitrary shaped waveguide with an all-dielectric anisotropic cladding ($\varepsilon_x = \varepsilon_y = 1.2$ and $\varepsilon_z = 15$) is shown in Fig. 2.8b. The shape of the cladding is chosen to be the same shape as the arbitrary core but with twice the local radius. The numerical calculation shows that about 36% of the total power is inside the low refractive index core and the mode area for this waveguide is about $0.7A_0$, ($A_0 = (\lambda/2n_{core})^2$). Note that without the momentum transformed cladding, the fundamental mode of the subwavelength core is weakly guided and most of the power lies outside the core (Fig. 2.8a). The calculated mode area for the bare waveguide is about $80A_0$ and only 1% of the total power lies inside the core. Availability of high index building blocks for metamaterials at lower frequencies can lead to better performance specifically for the 2D designs [83]. Nanowire metamaterials in the cladding can achieve the desired anisotropy (see supplementary information).

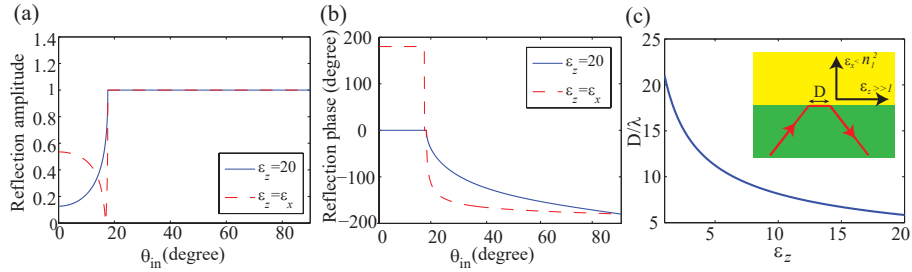


Fig. 2.9. **Goos-Hänchen effect in anisotropic media.** (a) Reflection amplitude and (b) reflection phase versus the incident angle. The first medium is glass and for the second medium $\varepsilon_x = 1.2$. (c) Goos-Hänchen phase shift versus ε_z of the second medium. We assume the center of angular spectrum of the incident beam is 1% above the critical angle and all of the angular spectrum components are greater than the critical angle. As the anisotropy increases (i.e. skin depth decreases), the Goos-Hänchen phase shift decrease.

2.9 Goos-Hänchen phase shift

The key building block for e-skin photonics are transparent anisotropic metamaterials. Designs for transparent metamaterials utilizing only semiconductors. Here, we outline how to verify the concept of extreme skin depth using the Goos-Hänchen phase shift.

Total internal reflection of a beam causes a lateral displacement which is known as Goos-Hänchen phase shift [84]. If the skin depth at total internal reflection decreases, the Goos-Hänchen phase shift decreases as well.

If the entire angular spectrum of the beam is above the critical angle and the center of spectrum is at θ_0 , the Goos-Hänchen phase shift can be calculated as [85]:

$$D = -\frac{\lambda}{2\pi} \frac{d\varphi(\theta)}{d\theta} \Bigg|_{\theta = \theta_0} \quad (2.7)$$

where $\varphi(\theta)$ is the reflection phase of an incident plane wave at the incident angle of θ . The reflection coefficient is $r = H_y^r / H_y^i = (k_{1x}\varepsilon_{2z} - k_{2x}\varepsilon_1) / (k_{1x}\varepsilon_{2z} + k_{2x}\varepsilon_1)$, where k_{1x} and k_{2x} are optical momenta normal to the interface between two dielectrics, H_y^i and H_y^r are total magnetic field of the incident and reflected waves, respectively. The reflection amplitude and phase at the interface of glass and a transparent anisotropic metamaterial ($\varepsilon_{2x} = 1.2$ and $\varepsilon_{2z} = 20$) boundary are compared with that at the interface of glass with an isotropic low-index dielectric in Fig. 2.9a and b, respectively. Above the critical angle where k_{2x} is imaginary, if ε_{2z} increases, the reflection phase reduces because the imaginary part of reflection coefficient becomes negligible in comparison with the real part. Thus according to (2.7), the Goos-Hänchen phase-shift decreases with the skin-depth. The Goos-Hänchen phase shift of a light beam versus ε_{2z} is plotted in Fig. 2.9c. We assume the center of the incident beam's angular spectrum is 1% above the critical angle and all of the angular spectrum components are greater than the critical angle.

2.10 Summary

In conclusion we have introduced a paradigm shift in light confinement strategy which rests on transforming the momentum of evanescent waves. Our transformations can be achieved by all-dielectric media fundamentally overcoming the foremost challenge in the field of plasmonics and metamaterials: optical absorption. We showed that for practical device applications the introduction of our engineered anisotropy in the space between conventional waveguides confines evanescent waves and always decreases the cross talk irrespective of core index or size. The approach of altering the momentum of evanescent waves can be utilized all across the spectrum for electromagnetic waves leading to a new class of devices which work on controlling evanescent field momentum.

3. ON-CHIP ALL-DIELECTRIC METAMATERIALS FOR DENSE PHOTONIC INTEGRATION

Ultra-compact, densely integrated optical components manufactured on a CMOS-foundry platform are highly desirable for optical information processing and electronic-photonic co-integration. However, the large spatial extent of evanescent waves arising from nanoscale confinement, ubiquitous in silicon photonic devices, causes significant cross-talk and scattering loss. Here, we demonstrate that anisotropic all-dielectric metamaterials open a new degree of freedom in total internal reflection to shorten the decay length of evanescent waves. We experimentally show the reduction of cross-talk by greater than 30 times and the bending loss by greater than 3 times in densely integrated, ultra-compact photonic circuit blocks. Our prototype all-dielectric metamaterial-waveguide achieves a low propagation loss of approximately 3.67 ± 1 dB/cm, comparable to those of silicon strip waveguides. Our approach marks a departure from interference-based confinement as in photonic crystals or slot waveguides, which utilize nanoscale field enhancement. Its ability to suppress evanescent waves without substantially increasing the propagation loss shall pave the way for all-dielectric metamaterial-based dense integration.

3.1 Outline of the problem

One of the long-standing goals of nanophotonics is the integration of electronic and photonic circuitry on a single CMOS chip for applications ranging from information processing and data centers to massively parallel sensing [46, 86–97]. This necessarily requires miniaturization with low power consumption in optical interconnects, active as well as passive photonic devices. There are two major figures of merit in designing photonic devices for a densely integrated circuit. One is the cross-talk, which occurs

due to the field overlap of two adjacent photonic waveguides, and the second is the radiation loss at sharp bends which limits the integration density [90].

Plasmonic waveguides can strongly reduce cross-talk and bending loss due to the sub-diffraction nature of light coupling to the free electrons of metals [48, 50, 51, 98–102]. However, the large ohmic loss of metals restricts the application of plasmonic structures for photonic integration [103, 104]. Over the last decade, many efforts have been made to miniaturize photonic components using all-dielectric structures [105–120]. Figure 3.1 illustrates a few classes of dielectric waveguides for light confinement in photonic chips. Strip waveguides, the most common type of waveguides for routing light in a silicon chip, are composed of a silicon channel surrounded by silicon oxide [90] (Fig. 3.1a). Due to the high contrast between the refractive index of the core and the cladding, light is confined inside the core as a result of total internal reflection. However, the mode size is seen to increase as we reduce the core size which hampers the use of strip waveguides to further miniaturize photonic circuits [44]. Photonic crystal waveguides can confine light inside a line defect due to Bragg reflection [34, 121, 122] (Fig. 3.1b). These waveguides perform efficiently at very sharp bends [123], however, the integration density is limited as the periodicity of Bragg reflectors is on the order of the wavelength and it cannot be perturbed by another waveguide nearby [56]. Additionally, slot waveguides have been proposed to confine light inside a sub-wavelength low index gap surrounded by high index dielectric rods [53] (Fig. 3.1c). To satisfy the continuity of the normal component of the displacement current at the high contrast interface, the electric field peaks inside the gap, leading to light confinement but at the cost of skin-depth expansion in the cladding. This causes cross-talk between adjacent waveguides and radiation loss at sharp bends in dense photonic integrated circuits.

Several alternative approaches inspired from atomic physics [124, 125], transformation optics [126], and inverse-design algorithms [127, 128] have also been proposed to minimize the cross-talk and the bending loss. However, these techniques add design complexity often required modification of the core as well as cladding [126]. They

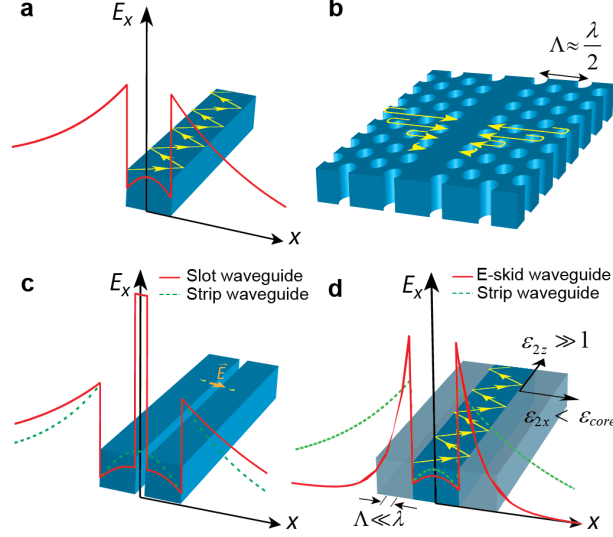


Fig. 3.1. **Fundamental differences between dielectric waveguides on an SOI platform.** **a**, strip waveguide; **b**, photonic crystal waveguide; **c**, slot waveguide; **d**, e-skid waveguide. The skin-depth in the cladding of e-skid waveguide is shorter compared to the other structures due to the strong effective anisotropy of the multilayer cladding. This counterintuitive approach can have a cladding with a higher average index than the core and marks a departure from interference based confinement as in photonic crystal waveguides or slot waveguides which utilize nanoscale field enhancement.

are not implementable on a large scale and cause propagation loss fundamentally limiting device performance. Thus, a new low-loss and scalable platform is needed for CMOS foundry compatible dense photonic integration with low cross-talk and reduced bending loss.

In this chapter, we demonstrate a platform which is fundamentally different from the existing approaches for designing CMOS compatible, ultra-compact, and low loss waveguides using all-dielectric anisotropic metamaterials. Our approach works based on photonic skin-depth engineering of evanescent waves in the cladding using a recently proposed degree of freedom in total internal reflection (TIR) [44, 129]. To describe the light confinement mechanism in our waveguides, first, we experimentally demonstrate the phenomenon of relaxed-total internal reflection in anisotropic meta-

Table 3.1.

Performance comparison between an e-skid waveguide and other dielectric waveguides. It is seen that the cross-talk is significantly reduced in e-skid waveguides at the negligible cost of propagation loss in comparison with other approaches.

Reference	Cross-talk	Propagation loss
Superlattice [124]	-20 dB	> 20 dB/cm
Adiabatic elimination [125]	-21.9 dB	N/A
Inverse design [128]	-22.9 dB	> 300 dB/cm
Dissimilar waveguides [134]	-20 dB	N/A
Sinusoidal waveguides [135]	-26.8 dB	> 600 dB/cm
This work (e-skid)	-30 dB	3.67 dB/cm

materials. These relaxed conditions allow the control of evanescent wave decay which is the fundamental origin of cross-talk and bending loss in silicon photonic devices. As illustrated in Fig. 3.1d, we use these anisotropic metamaterials as a cladding for on-chip dielectric waveguides fabricated on a monolithic silicon-on-insulator (SOI) platform. As a result, cross-talk is reduced down to -30 dB in the photonic circuit. Furthermore, we use a transformation optics approach to show that the radiation loss at sharp bends is strongly influenced by the skin-depth in the cladding. We experimentally show that the anisotropic metamaterial cladding can simultaneously reduce the bending loss at sharp bends up to 3 times compared to conventional silicon strip waveguides. We clarify the counter-intuitive nature of light confinement in our approach compared to existing photonic crystal, slot waveguide, and graded index waveguide methods [34, 53, 130–133]. Our work shows that all-dielectric anisotropy on-chip presents a scalable route to simultaneously improve cross-talk and bending loss with propagation loss as low as ≈ 3.67 dB/cm. For completeness, we show the improvements in figures of merit of our achieved platform with recent state-of-the-art photonic designs (See Table 3.1).

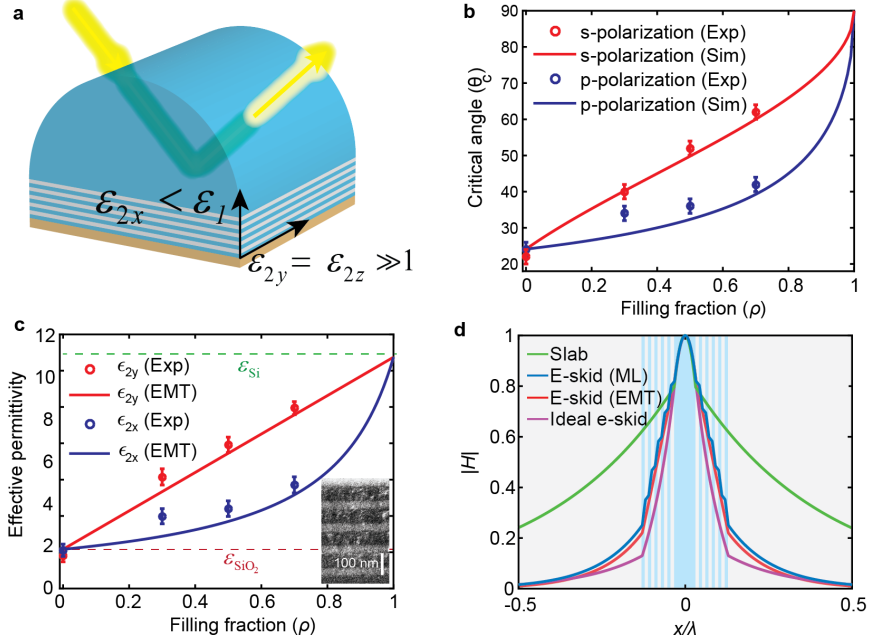


Fig. 3.2. **Relaxed total internal reflection.** **a**, Schematic of the relaxed-TIR experiment. We measure the reflection from the Si prism and Si/SiO₂ multilayer interface for both *s* and *p* polarizations at $\lambda = 1550$ nm. Multiple samples with different ρ have been fabricated. The periodicity for all samples is 100 nm and the total thickness of the multilayer is 500 nm. A 200 nm layer of tungsten is deposited on top of the multilayer (brown) to suppress the reflection from the air interface. **b**, The measured critical angle for *s* and *p* polarizations versus the silicon filling fraction in comparison with effective medium theory (EMT) calculations. Error bars represent the instrument limit of the measuring device. In contrast with the conventional phenomenon of TIR, observable differences between the critical angles is seen for different polarizations in agreement with relaxed-TIR theory. **c**, Retrieved effective permittivity of the multilayer from the critical angle measurements show strong anisotropy in agreement with EMT. The refractive index of Si and SiO₂ are taken to be 3.4 and 1.47, respectively, for the theoretical calculations. The inset shows the SEM image of an Si/SiO₂ multilayer with $\rho = 0.5$. **d**, Normalized calculated magnetic field profile for the TM mode of a conventional slab waveguide compared to extreme skin-depth (e-skid) waveguides with Si/SiO₂ multilayer cladding. The blue and grey regions represent Si and SiO₂, respectively. The core size, Λ , and ρ are 100 nm, 30 nm, and 0.5, respectively. The multilayer anisotropic claddings strongly affect the decay of the evanescent wave in the cladding. The practical multilayer structure performs close to an ideal anisotropic case ($\epsilon_{2,x} = \epsilon_{SiO_2}$ and $\epsilon_{2,z} = \epsilon_{Si}$).

3.2 Relaxed total internal reflection

We demonstrate that only a single component of the dielectric tensor governs total internal reflection (TIR) in anisotropic media opening a new degree of freedom to control evanescent waves. In conventional TIR, if $n_1 > n_2$ and the incident angle is greater than the critical angle ($\theta_c = \sin^{-1}(n_2/n_1)$), light is reflected back to the first medium and decays evanescently in the second medium. However, we have recently found that the TIR conditions at the interface of an isotropic and an anisotropic dielectric are relaxed to [44,136]:

$$\begin{aligned} n_1 &> \sqrt{\varepsilon_{2x}}, & p \text{ polarization} \\ n_1 &> \sqrt{\varepsilon_{2y}}, & s \text{ polarization} \end{aligned} \quad (3.1)$$

where $\begin{bmatrix} \varepsilon_{2x} & \varepsilon_{2y} & \varepsilon_{2z} \end{bmatrix}$ is the permittivity tensor of the second medium, and the interface between the two media lies on the yz plane. As a result, the critical angle for s and p polarizations differ:

$$\begin{aligned} \theta_c &= \sin^{-1}(\sqrt{\varepsilon_{2x}}/n_1), & p \text{ polarization} \\ \theta_c &= \sin^{-1}(\sqrt{\varepsilon_{2y}}/n_1), & s \text{ polarization} \end{aligned} \quad (3.2)$$

We emphasize that these relaxed conditions for p polarized incident light allow us to arbitrarily increase or decrease the permittivity in the z direction while still preserving TIR. This hitherto un-utilized degree of freedom can thus be used to control the skin depth of evanescent waves. If $\varepsilon_{2z} \gg 1$, evanescent waves decay faster than in vacuum allowing for strong light confinement inside dielectric waveguides [44,129]. In this limit, note that the averaged index in anisotropic medium 2 can be larger than the refractive index in isotropic medium 1 yet the light will be totally reflected above the critical angle.

We implement this anisotropy using Si/SiO₂ multilayers with subwavelength thicknesses (Fig. 3.2a) at the telecommunication wavelength ($\lambda = 1550$ nm). Figure 3.2 highlights the contrast between relaxed-TIR and conventional TIR, showing the

measured light reflection at the interface of a hemi-cylindrical Si prism and the anisotropic multilayer metamaterial. The periodicity of the multilayer is $\Lambda = 100$ nm and 5 periods have been deposited on the prism. The Maxwell-Garnett effective medium theory (EMT) [137] predicts that the multilayer with subwavelength periodicity demonstrates strong anisotropy [44, 138–141] at the operating wavelength ($\epsilon_{2y} = \epsilon_{2z} = \epsilon_{\text{Si}}\rho + \epsilon_{\text{SiO}_2}(1 - \rho)$ and $1/\epsilon_{2x} = \rho/\epsilon_{\text{Si}} + (1 - \rho)/\epsilon_{\text{SiO}_2}$ where ρ is the fill fraction of silicon). Note we are in the effective medium metamaterial limit ($\Lambda \ll \lambda$) away from the photonic crystal regime ($\Lambda \sim \lambda$). Reflection occurs on two interfaces, the primary silicon-metamaterial interface and the secondary metamaterial-air interface. We have deposited a thin tungsten layer on top of the multilayer metamaterial to attenuate the unwanted reflection from the secondary metamaterial/air interface. Figure 3.2b displays different measured critical angles for s and p polarizations. Various samples with different fill fractions have been fabricated. As ρ deviates from 0 and 1, the multilayer displays effective anisotropy and the critical angle for s and p polarized incidences are separated in agreement with relaxed-TIR theory in equation (3.2). The effective permittivity of the multilayer structure (extracted from the critical angle) shows strong anisotropy and is in good agreement with EMT (Fig. 3.2c). It is clearly seen that the critical angle depends on only one component of the permittivity tensor for each polarization irrespective of the fill-fraction. With the extra degree of freedom afforded by the other components of the dielectric tensor, this anisotropic structure can be used as a cladding for conventional dielectric waveguides to control the evanescent waves and skin-depth in the cladding [44, 142–144]. Figure 3.2d displays the effect of the multilayer anisotropic cladding on reducing of the evanescent wave skin-depth as compared to a conventional slab waveguide. Note that this evanescent wave engineering approach in extreme skin-depth (e-skid) waveguides is due to the fast variation of the evanescent fields in a subwavelength high-index-contrast super-lattice (Fig. 3.2d). This is fundamentally different from other light confinement strategies which function on interference of propagating waves (photonic crystals) or field enhancement in a slot [34, 53, 131–133].

3.3 On-chip e-skid waveguides

To impact the field of silicon photonics, the one-dimensional e-skid waveguide (Fig. 3.2d) has to be implemented on an SOI platform. This places stringent restrictions on monolithic fabrication, minimum feature sizes, and deviations in field profiles due to quasi-2D behavior. Our design to adapt relaxed TIR and skin-depth engineering ($\delta \ll \lambda$) on-chip is shown in Fig. 3.3. Here the conventional quasi-2D strip waveguide is surrounded by a cladding made of alternating vacuum-silicon sub-wavelength ridges which achieves strong anisotropy ($\varepsilon_{2x} < \varepsilon_{\text{core}}$ and $\varepsilon_{2z} \gg 1$). Our goal is to confine the TE-like mode (its dominant electric field component is E_x) used in conventional silicon strip waveguides. Since the TM-like mode is polarized in the y direction, the electric field does not probe/feel the anisotropy of the cladding. Hence, the metamaterial cladding does not play any role in TM-mode confinement. For more details about the polarization effect, see Appendix B.

Figure 3.3a emphasizes the counter-intuitive nature of the confinement caused by anisotropic media which beats the confinement of conventional high index contrast interface consisting of silicon surrounded by vacuum (blue curve in Fig. 3.3a). As it is seen in Fig. 3.3a, if we increase the index of the cladding only in the z direction while the index in the other directions are fixed, the evanescent wave decays faster in the cladding and the skin-depth reduces drastically. Note, the average cladding index increases but the mode decay length decreases. This behavior is in fundamental contrast to confinement in conventional strip waveguides with isotropic claddings or graded index claddings [133] where decreasing the contrast between the core index and cladding index results in slow decay of evanescent waves, not faster decay [129].

Figure 3.3b shows the field profile of a practical e-skid waveguide with the multi-layer metamaterial cladding ($\Lambda \ll \lambda$). We can see the practical multilayer cladding shows strong effective anisotropy to ensure the fast decay of the evanescent wave in the cladding. The 2D field profiles in a plane perpendicular to the propagation direction and comparison of the practical e-skid waveguide with a homogeneous anisotropic

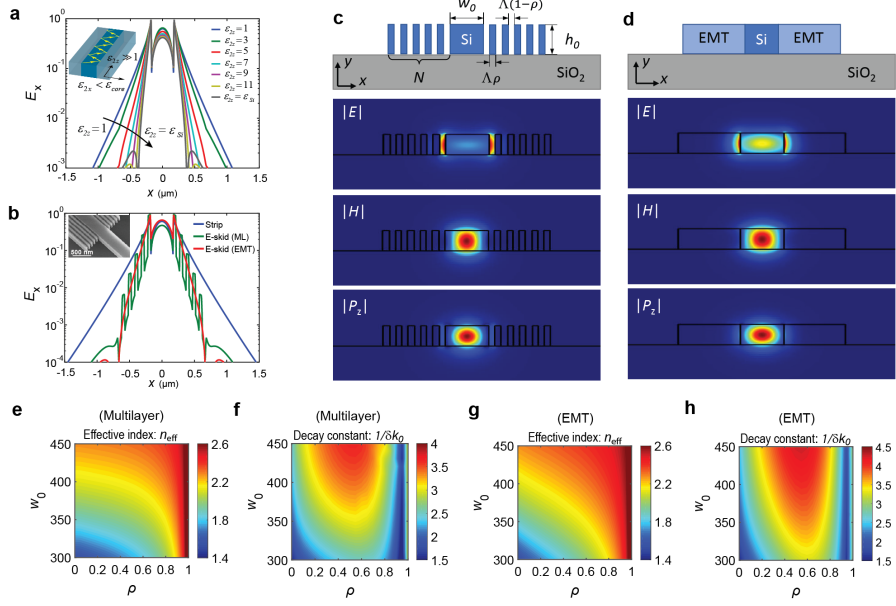


Fig. 3.3. **On-chip extreme skin-depth waveguides.** **a**, Ideal on-chip e-skid waveguide; light is confined by total internal reflection inside the core and as the effective anisotropy of the multilayer metamaterial cladding is increased, evanescent waves of TE-like modes decay faster in the cladding in comparison with the field in strip waveguides ($\varepsilon_{zz} = 1$). Note that $\varepsilon_{2x} = 1$ for all cases. **b**, The simulated electric field profile at the center of the e-skid waveguide with multilayer (green) and homogenized metamaterial ($\varepsilon_{2x} = 1.85$ and $\varepsilon_{2z} = 6.8$) (red) claddings, in comparison with a strip waveguide (blue). Inset shows the SEM image of the fabricated e-skid to strip waveguide transition. **c**, **d**, Schematic and field profiles of **(c)** realistic e-skid waveguide with multilayer claddings and **(d)** its equivalent model with EMT claddings. **e**, **f**, Effective refractive indices ($n_{\text{eff}} = k'_z/k_0$) and **g**, **h**, normalized decay constants ($k''_x/k_0 = 1/\delta k_0$) of the e-skid waveguide as functions of the core width w_0 and filling fraction ρ : with **(e, g)** multilayer and **(f, h)** EMT claddings, respectively. Geometric parameters are $h_0 = 220$ nm, $w_0 = 350$ nm, $\Lambda = 100$ nm, $\rho = 0.5$, and $N = 5$, unless otherwise indicated. The free space wavelength is $\lambda = 1550$ nm. Simulations confirm that the cladding achieves effective all-dielectric anisotropy as well as the increased decay constant of evanescent waves outside the core.

cladding are shown in Fig. 3.3c and 3.3d. A good agreement with the effective medium approximation is seen. Figure 3.3e-3.3h illustrate the effective modal index and the decay constant in the cladding for a wide range of core sizes and the fill fractions of silicon in the multilayer cladding. First, a strong agreement is seen between EMT and practical multilayer structures indicating that the cladding indeed achieves effective all-dielectric anisotropy. Secondly, the effective modal index is below the core index indicative of relaxed total internal reflection as the mechanism of confinement. As expected, simulations prove that the primary role of the on-chip multi-layer cladding is to increase the decay constant of evanescent waves (k_x''/k_0), as shown in Figs. 3.3f and 3.3h, and it does not significantly change the effective modal index of propagating waves (k_z'/k_0), as shown in Figs. 3.3e and 3.3g. It is seen that the largest decay constant is achieved at $\rho \approx 0.5$ where the strongest anisotropy is attained. Note that $\rho = 0$ corresponds to the case of no cladding. We also emphasize that the power in the core is not compromised by the presence of the skin-depth engineering cladding and increased anisotropy causes an enhancement in power confinement.

This light confinement strategy in e-skid waveguides is fundamentally different from that in photonic crystal waveguides. Our multilayer structures function in the deep subwavelength limit ($\Lambda \ll \lambda$), not the photonic crystal limit ($\Lambda \sim \lambda$) and the performance of the e-skid waveguide is independent of the multilayer periodicity or disorder (see Appendix B). Furthermore, there are no Dyakonov wave solutions in e-skid waveguides as the optical axis of the anisotropic cladding is perpendicular to the interface and the direction of propagation [105, 145–149]. It is also important to note that the main goal of the anisotropic multilayer cladding is to control the decay constant of evanescent waves on-chip, not to achieve birefringence in the effective modal index of propagating waves as achieved previously in sub-wavelength grating structures [110, 130, 131, 150], multi-slotted waveguides [132], or nonlinear phase matching applications [81].

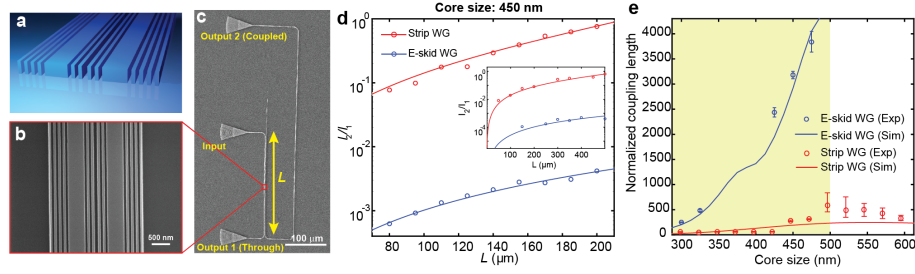


Fig. 3.4. **Cross-talk in e-skid waveguides.** **a**, Schematic of coupled e-skid waveguides on an SOI platform. The waveguide height, center-to-center separation between the two waveguides (s), and Λ are 220 nm, 1000 nm, and 120 nm, respectively. A cladding oxide is also added on the top of the waveguides. The number of ridges between the waveguides is dictated by the waveguide core size **b**, Top view SEM image of the coupled e-skid waveguides. **c**, The experimental setup to measure the cross-talk between the two waveguides at the telecommunication wavelength ($\lambda = 1550$ nm). Light is in-coupled to the first waveguide through the middle grating coupler. The second waveguide is coupled to the first waveguide for a length of L . In this experiment, the bending radius is $5 \mu\text{m}$, hence, we can ignore the bending loss. **d**, The ratio between the measured output powers for strip waveguide and e-skid waveguide versus L at the telecommunication wavelength, respectively. The ratio for the e-skid waveguide is two orders of magnitude lower, indicating that far less power is coupled to the second waveguide. The inset shows the ratio for the waveguides without the top cladding oxide. In this case, the metamaterial cladding can increase the coupling length up to 30 times or reduce the cross-talk -30 dB. See Supplementary Figure 8 for more details. **e**, Comparison of the simulated and measured coupling length for e-skid waveguides and strip waveguides. The coupling length is normalized to the wavelength. Error bars represent the standard deviation of the fitting curves. The optimum match between the simulation and experiment is achieved when $\rho = 0.6$ for the cladding of e-skid waveguides. The coupling length for e-skid waveguides is an order of magnitude larger in comparison with strip waveguides (shaded region). The coupling length for strip waveguides with larger core size decreases because the overlap between the evanescent tails is increased although more power is confined inside the core (unshaded region).

3.4 Cross-talk in e-skid waveguides

The skin-depth of evanescent waves is the fundamental origin of cross-talk between waveguides that hinders dense photonic integration. Cross-talk, or power coupling between photonic devices, arises due to the perturbation of the optical mode when the evanescent tail of one waveguide overlaps with a nearby waveguide. However, if we control the skin-depth in the cladding, we can reduce the perturbation due to the adjacent waveguide, subsequently reducing the cross-talk to surpass the integration limit in current silicon photonics.

We now demonstrate this drastic reduction in the cross-talk made possible with the anisotropy in the cladding (Fig. 3.4a). The top view image of coupled e-skid waveguides fabricated on an SOI chip is shown in Fig. 3.4b. The power exchanged between two identical lossless coupled waveguides is:

$$\begin{aligned} I_1 &= I_0 \cos^2 \left(\frac{\pi}{2L_c} L \right), \\ I_2 &= I_0 \sin^2 \left(\frac{\pi}{2L_c} L \right), \end{aligned} \quad (3.3)$$

where I_0 is the input power, L is the distance for which the two waveguides are coupled, and L_c is the coupling length. Note L_c is defined such that if the waveguides are coupled for a distance $L = L_c$, complete power transfer occurs from the first waveguide to the adjacent waveguide. Figure 3.4c illustrates the experimental setup to measure the coupling length. Light is in-coupled to the first waveguide through the grating coupler [151] and the second waveguide is coupled to the first waveguide over a distance of L . The center-to-center separation between the two waveguides is only 1000 nm. The output power of the two waveguides is out-coupled by the two grating couplers at the ends of each waveguide. Note that we can ignore the propagation loss in this experiment as the total length does not exceed a few hundred microns whereas the propagation loss is 3.67 dB/cm at the operating wavelength $\lambda = 1550$ nm (see Appendix B for details about the characterization of the propagation loss). The ratio between the measured powers for strip waveguides and e-skid waveguides are shown

in Fig. 3.4d. This highlights that the analytical expression ($I_2/I_1 = \tan^2(\pi L/2L_c)$) matches the experimental data. It is clearly seen that the coupled power to the second waveguide is almost two orders of magnitude lower for the e-skid waveguide. The measured and simulated [152] coupling length normalized to the wavelength for different core sizes is plotted in Fig. 3.4e for waveguides with the same separation distance of 1000 nm. It is seen that the coupling length for the TE-like mode of e-skid waveguides is an order of magnitude higher than that for strip waveguides allowing miniaturization of photonic integrated circuits without considerable cross-talk between the waveguides. Note that increasing the core size in conventional strip waveguides, which corresponds to higher power confinement inside the core, does not guarantee the reduction in cross-talk (unshaded region Fig. 3.4e) as the evanescent tails are not controlled. These drastically increased L_c are due to the reduced skin-depth with a higher anisotropy, reducing the waveguide cross-talk significantly in comparison with other dielectric structures which have been proposed to reduce the cross-talk (Table 3.1). Note that since the TM-like mode has a negligible electric field component in the x direction, it does not probe/feel the dielectric anisotropy of the cladding. As expected, this results in higher cross-talk for TM-modes compared to strip waveguides (see Appendix B for more details about the polarization effect and the proposed design to control the skin-depth of the TM-like mode).

3.5 Bending loss in e-skid waveguides

The critical phenomenon of bending loss [153–155] can also be reduced by adding the anisotropic metamaterial cladding. The counterintuitive connection of bending loss and skin-depth is revealed by an approach adapted from transformation optics [153, 156]. Here, we consider a curved waveguide in the xz plane with a 90° bend and a bending radius of R ($R \gg \delta$). The center of the curved waveguide is at the origin (Figs. 3.5b and 3.5d (inset)). If we apply the transformation: $u + iw = R \ln \frac{x+iz}{R}$, $v = y$ [153, 156], the curved waveguide is mapped to a straight

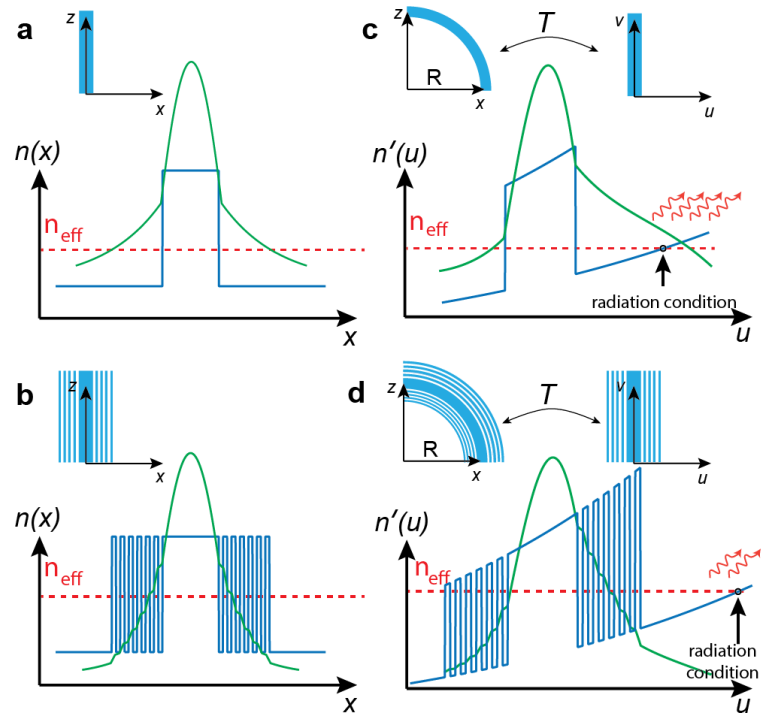


Fig. 3.5. **Curved waveguides and skin-depth engineering.** **a, b,** Refractive index profile (blue) and the magnetic field profile (green) of (a) a straight strip waveguide and (b) a straight e-skid waveguide. **c,** The corresponding bent waveguides (c,d) can be transformed to straight waveguides with inhomogeneous refractive index profiles in a new coordinate system. If the local refractive index of the cladding exceeds the effective modal index ($n'(u_0) > n_{\text{eff}}$), the waveguide mode starts radiating. This occurs at the radiation condition point denoted by $u = u_0$ (red arrows). The multilayer metamaterial cladding in e-skid waveguides suppresses the evanescent wave field beyond this radiation condition point. Thus, in comparison with conventional bent waveguides, lesser power is radiated due to curvature effects.

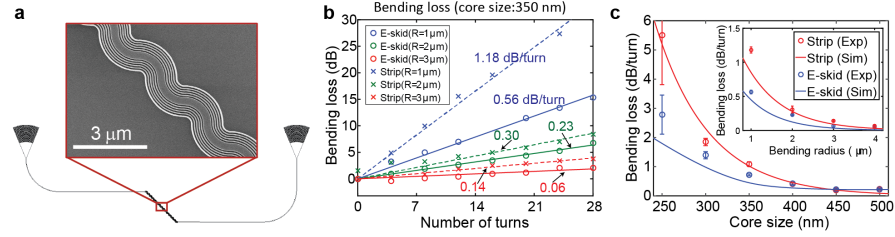


Fig. 3.6. **Bending loss in e-skid waveguides.** **a**, Layout and zoomed-in SEM images of the test devices to characterize the bending loss. **b**, Measured bending losses with different number of turns; circles and crosses are the e-skid and strip waveguides, respectively, and blue, green, and red are at different bending radii of $R = 1, 2,$ and $3 \mu\text{m}$. Each experimental result is fitted with a linear line: e-skid (solid) and strip (dashed) lines. The core size is $w_0 = 350 \text{ nm}$. **c**, Characterized bending loss vs. core size ($R = 1 \mu\text{m}$): e-skid (red) and strip (blue) waveguides. Inset shows the characterized bending loss vs. bending radius ($w_0 = 350 \text{ nm}$). Red and blue lines are the simulated bending losses of the e-skid and strip waveguides, respectively. Error bars represent the standard deviation of the fitting curves. Other parameters ($h_0, \Lambda, \rho, N,$ and λ) are the same as in Fig. 3.3. Confinement of the evanescent waves in e-skid waveguides due to the metamaterial cladding helps to reduce the bending loss at sharp bends in photonic integrated circuits. This effect is stronger for waveguides with smaller core sizes, as a considerable amount of the power lies outside the core and decays slowly.

waveguide in the uw plane (Figs. 3.5b and 3.5d). This causes the refractive index of the transformed waveguide to become inhomogeneous in the new coordinate system as [153, 156]: $n'(u) = n(x(u)) e^{u/R}$, where $n(x(u))$ is the refractive index of the straight waveguide as shown in Figs. 3.5a and 3.5b. Bending loss or radiative power leakage from the core occurs in this straight inhomogeneous index waveguide when the local index of the cladding exceeds the effective modal index (n_{eff}). Hence, if we suppress the field near and beyond this radiation condition point (Fig. 3.5b and 3.5d), we can reduce the bending loss. Note that due to the spatial transformation of coordinates, the electromagnetic fields are also transformed causing the expansion of the skin-depth (δ) on the right-hand side of the waveguide and shrinkage of it on the left-hand side (Figs. 3.5b and 3.5d):

$$\begin{aligned}\delta_{\text{right}} &\approx \delta + 2\delta^2/R, \\ \delta_{\text{left}} &\approx \delta - 2\delta^2/R.\end{aligned}\tag{3.4}$$

However, if we add the anisotropic metamaterial cladding, we can reduce the skin-depth. As a result, less power will be radiated at the radiation condition point, leading to reduced bending loss.

To confirm the effect of the anisotropic metamaterial claddings on the bending loss, we have investigated the bending losses of the e-skid and strip waveguides, both experimentally and numerically [157]. To characterize the bending losses, we have cascaded 90° bent waveguides sequentially with different numbers of turns (Fig. 3.6a and Appendix B), then characterized the bending loss per turn by comparing the transmissions. Figures 3.6b and 3.6c shows the measured bending losses vs. the core size and the bending radius. In all cases, the bending losses with the e-skid waveguide is lower than that with the strip waveguide, which is due to the reduced skin-depth with the anisotropic metamaterial claddings. Note that if the fabrication advancements on the CMOS platform allowed us to reduce the feature size and approach an ideal anisotropic cladding ($\Lambda \rightarrow 0$), we would achieve further reduction of the bending loss for TE-like modes in e-skid waveguides (See Appendix B for more details as well

as the bending loss calculation for TM-like modes). Our simulations account for all sources of bending loss including radiation and mode-mismatch.

3.6 Methods

Si/SiO₂ multilayers were fabricated using magnetron sputtering and magnetron reactive sputtering, respectively. Silicon and silica were both deposited at a power of 150 W using a pulsed power supply at a frequency of 150 kHz and off time of 0.5 μ s for silicon and 0.8 μ s for silica. A special substrate holder was built to hold the prisms during deposition. With the new substrate holder and the large thickness of the prism, the film properties would change as the substrate was much closer to the target, producing films with higher loss. Reducing the deposition power produced lower loss films. A 200 nm thick layer of tungsten was deposited at 300 W, 150 kHz and 0.5 μ s on top of the multilayer structure at each fill fraction. The prism was illuminated with a 1530 nm narrow line width laser. A broadband linear polarizer placed in the beam path created *s* and *p* polarized light. The incident angle was increased in increments of 2° from 10° to 80°. A Newport Optics Optical Power Meter calibrated to a wavelength of 1530 nm was then used to measure the reflected power. The two reflections at the prism/air interface in the optical path were accounted for when comparing experiment to EMT simulations.

The on-chip devices for measuring cross-talk in the main text and bending loss in Figure B.9 were fabricated using a JEOL JBX-6300FS Electron Beam Lithography system [158] operated at 100 keV energy, 8 nA beam current, and 500 μ m exposure field size. A silicon-on-insulator wafer (220 nm thick silicon on 3 μ m thick silicon dioxide) has been used. A solvent rinse and hot-plate dehydration baked. Then, hydrogen silsesquioxane resist (HSQ, Dow-Corning XP-1541-006) was spin-coated at 4000 rpm, and then hotplate baked at 80 °C for 4 minutes. Shape placement by the machine grid, the beam stepping grid, and the spacing between dwell points during the shape writing, were 1 nm, 6 nm, and 6 nm, respectively. An exposure

dose of $2800 \mu\text{C}/\text{cm}^2$ was used. The resist was developed by immersion in 25% tetramethylammonium hydroxide for 4 minutes, followed by a flowing deionized water rinse for 60 s, an isopropanol rinse for 10 s. Then blown dry with nitrogen. The inductively coupled plasma etching in an Oxford Plasmalab System 100 was used to remove silicon from unexposed areas, with a chlorine gas flow of 20 sccm, ICP power of 800 W, pressure of 12 mT, bias power of 40 W, and a platen temperature of 20 °C, resulting in a bias voltage of 185 V. During etching, perfluoropolyether vacuum oil was used to mount chips on a 100 mm silicon carrier wafer. Cladding oxide was deposited using plasma enhanced chemical vapor deposition (PECVD) in an Oxford Plasmalab System 100 with nitrous oxide (N_2O) flow of 1000.0 sccm, a silane (SiH_4) flow of 13.0 sccm, high-purity nitrogen (N_2) flow of 500.0 sccm, high-frequency RF power of 120 W, pressure at 1400 mT, and a platen temperature of 350 °C. Chips rest directly on a silicon carrier wafer during deposition and are buffered by silicon pieces on all sides to aid uniformity.

To characterize the on-chip devices, a custom-built automated test setup was used [90]. An Agilent 81635A optical power sensor was used as the output detector and Agilent 81600B tunable laser as the input source. The wavelength was swept in 10 pm steps from 1500 to 1600 nm. To maintain the polarization state of the light, a polarization maintaining fiber was used for coupling the TE polarization into the grating couplers [151]. A polarization maintaining fiber array was used to couple light in/out of the chip.

For the bending loss experiment in the main text, the cross-talk experiment in Figure B.8, the insertion loss experiments in Figure B.13, and the propagation loss experiment in Figure B.14, a standard SOI wafer is used as a substrate with 2 μm buried oxide (BOX) and 220 nm top silicon layer. Diluted hydrogen silsesquioxane (HSQ) with methyl isobutyl ketone (MIBK) was spun on the substrate as a negative-tone electron beam resist layer. The resist layer was exposed by a 100 kV electron-beam lithography system, VB6-UHR (Raith), which is capable of 2 nm beam step resolution. After the development of the resist, the top silicon layer was etched

by Cl_2/O_2 based reactive-ion plasma etching tool (Panasonic P610) to transfer the waveguide pattern from the resist to the silicon layer.

3.7 Summary

In summary, we have introduced a photonic platform which can add the critical but overlooked functionality of controlling evanescent waves to the CMOS foundry. We have shown that high index contrast grating structures in the deep sub-wavelength limit can act as an all-dielectric metamaterial cladding for simultaneously achieving total internal reflection and controlling the skin-depth of evanescent waves. The coupling length is improved more than an order of magnitude and the bending loss is improved three times compared to conventional on-chip waveguides with an average propagation loss of 3.67 dB/cm at telecommunication wavelengths. The decreased photonic skin depth regime has not been realized till date but has been attempted in initial studies [159]. This is because anisotropic all-dielectric metamaterial response requires more than one period of the unit cell to control evanescent wave decay [44, 129, 136]. Although we use Electron Beam Lithography (EBL) as a convenient prototyping technique for the sub-wavelength structures, these devices can in principle be fabricated using deep ultraviolet (DUV) CMOS foundries; specifically, advanced 193 nm immersion lithography technology has been used to fabricate silicon photonic devices with feature sizes down to 50 nm [160]. Our work paves the way for all-dielectric metamaterials to enter the practical realm of CMOS foundry photonics to achieve improved photonic integrated circuits.

4. SWITCHING PURCELL EFFECT WITH NONLINEAR EPSILON-NEAR-ZERO MEDIA

An optical topological transition is defined as the change in the photonic iso-frequency surface around epsilon-near-zero (ENZ) frequencies which can considerably change the spontaneous emission of a quantum emitter placed near a metamaterial slab. Here, we show that due to the strong Kerr nonlinearity at ENZ frequencies, a high-power pulse can induce a sudden transition in the topology of the iso-frequency dispersion curve, leading to a significant change in the transmission of propagating as well as evanescent waves through the metamaterial slab. This evanescent wave switch effect allows for the control of spontaneous emission through modulation of the Purcell effect. We develop a theory of the enhanced nonlinear response of ENZ media to s and p polarized inputs and show that this nonlinear effect is stronger for p polarization and is almost independent of the incident angle. We perform finite-difference time-domain (FDTD) simulations to demonstrate the transient response of the metamaterial slab to an ultrafast pulse and fast switching of the Purcell effect at the sub-picosecond scale. The Purcell factor changes at ENZ by almost a factor of three which is an order of magnitude stronger than that away from ENZ. We also show that due to the inhomogeneous spatial field distribution inside the multilayer metal-dielectric superlattice, a unique spatial topological transition metamaterial can be achieved by the control pulse induced nonlinearity. Our work can lead to ultra-fast control of quantum phenomena in ENZ metamaterials.

4.1 Outline of the problem

Structures with epsilon-near-zero (ENZ) response have emerged as a unique nanophotonic platform for controlling light because of field enhancement and spatially coher-

ent wave behavior in these media [57, 105, 161, 162]. This has led to many interesting phenomena and applications such as controlling thermal emission [163], observation of Ferrel-Berremann modes [164], super-coupling [165], and enhanced dipole-dipole interaction [7, 166]. Recently, strong nonlinearity in ENZ media has become a domain of interest because of significant change in the refractive index around the ENZ frequencies as well as the field enhancement due to boundary effects at the high contrast interfaces [58, 59, 167], phase mismatch-free propagation [168], and strong nonlocality at ENZ [169, 170].

In this chapter, we propose a hyperbolic metamaterial (HMM) slab operating around ENZ frequencies, in which a nonlinear gate signal controls and switches the decay rate of light emitted by a dipole emitter above the slab (Fig. 4.1.(a)). This can give rise to a modulation approach for spontaneous emission through switching the Purcell effect. First, we develop a theory of nonlinear light propagation in anisotropic ENZ media for s and p polarized light. We report on the formation of a unique ENZ-transition metamaterial induced by nonlinear wave interactions and inhomogeneity of the field distribution inside the medium. As a result, the spontaneous decay rate of a quantum emitter close to the slab is considerably changed. We propose experiments to verify our predictions taking into account the role of dispersion, absorption, and finite unit-cell size in practical metal-dielectric nonlinear HMMs. Furthermore, to understand the response of the metamaterial to ultra-fast pulses, we carry out finite-difference time-domain (FDTD) simulations. We propose optimum gate pulse widths to open up the possibility for switching Purcell effect with sub-picosecond response times using ENZ media.

4.2 Linear and nonlinear response of hyperbolic metamaterials at ENZ

HMMs are a class of non-magnetic uniaxial metamaterials with double-sheeted (type I) or single-sheeted (type II) hyperbolic iso-frequency dispersion curves [60, 171, 172]. There are two well-known approaches for practical realization of HMMs:

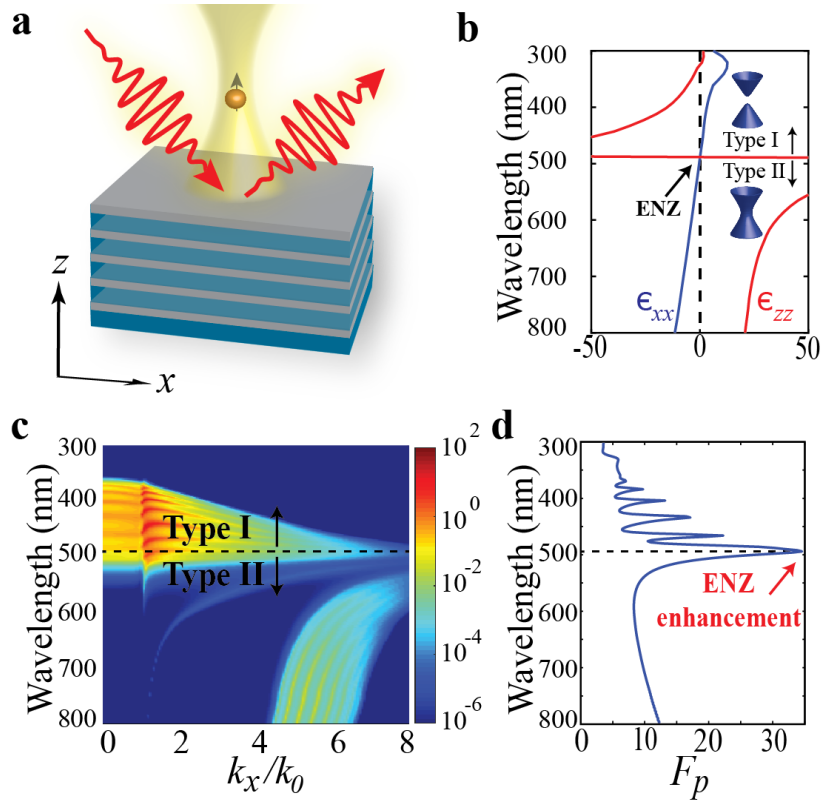


Fig. 4.1. **Switching of Purcell effect.** (a) A nonlinear gate signal controls the transmission of evanescent waves emitted by a quantum emitter above HMM around the ENZ frequencies. (b) The real part of effective permittivity of the Ag/TiO₂ multilayer metamaterial with Silver filling fraction of $\rho = 0.5$. The inset illustrates the iso-frequency dispersion curve of type I and type II HMMs. An optical topological transition is observed at ENZ. (c) Transmission of propagating and evanescent p-polarized waves through an Ag/TiO₂ multilayer with a total thickness of 400 nm and a periodicity of $\Lambda = 50$ nm. The transmission of high-k modes in both regions is high, but in type I region, the effect is stronger, especially close to the ENZ wavelengths. Due to the finite thickness of the unit-cell, the ENZ wavelength is redshifted in multilayer structure in comparison with EMT. (d) Purcell factor for a vertically oriented dipole above the slab modeled by EMT. A rapid change in the Purcell factor is observable at ENZ due to the optical topological transition. Other peaks in type I correspond to slow-light modes of the HMM slab.

metallic nanowires in a dielectric host matrix [173–175], and metal-dielectric multilayers [164, 176]. Here, we emphasize the second approach due to ease of fabrication and experimental verification. Figure 4.1.(b) displays the parallel ($\epsilon_{xx} = \epsilon_{yy}$) and normal (ϵ_{zz}) components of the effective dielectric tensor of an Ag/TiO₂ multilayer metamaterial derived from Maxwell-Garnett effective medium theory (EMT) [137]. An optical topological transition from type I to type II is seen at the ENZ wavelength. HMMs show interesting characteristics due to their open dispersion surfaces and the coupling of high-k modes (evanescent waves in vacuum) to the metamaterial modes [60]. Figure 4.1.(c) shows the transmission of low-k ($k_x < k_0$) and high-k ($k_x > k_0$) modes through the multilayer using transfer matrix method. The peaks correspond to the coupling of evanescent waves to the metamaterial modes with large wave vectors. We emphasize that even though the linear properties of HMMs have been studied extensively, the “evanescent wave switch” we introduce in the paper using nonlinear interactions has not been studied till date.

If a quantum emitter is placed near an HMM slab, the non-radiative evanescent waves of emitter are coupled to the high-k modes of metamaterials. As a result, spontaneous emission rate is enhanced [177–179]. Figure 4.1.(d) displays the spontaneous emission rate spectrum of a quantum emitter above the multilayer structure modeled by EMT. The dipole emitter is assumed vertically polarized which is placed 20 nm above the metamaterial slab, and the emission rate is normalized to the emission of emitter in free space. This enhancement factor is known as Purcell factor (F_p) [60]. Enhanced Purcell effect is obtained in both regions, but larger enhancement is observed in type I region due to the high transmission of low-k as well as high-k modes. The strongest peak around $\lambda = 500$ nm corresponds to the coupling of power to the resonating mode of the slab when ENZ response is achieved along the direction perpendicular to the layers. Other peaks in type I region correspond to slow-light modes of HMMs [180]. We now show that the strong nonlinearity at ENZ can help to effectively change the type of HMMs. This opens up the possibility of switching the Purcell effect.

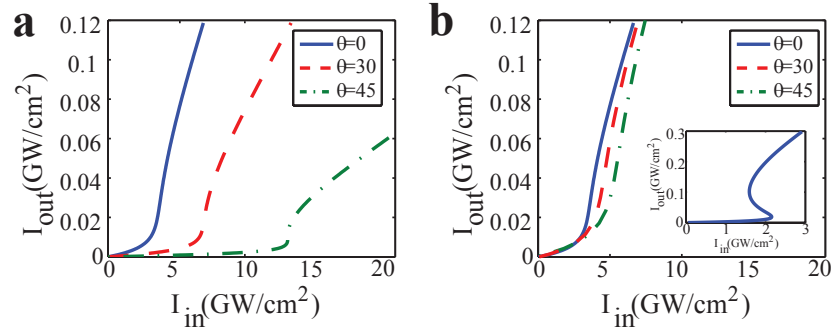


Fig. 4.2. **Nonlinear response at ENZ.** Nonlinear response of (a) *s* polarized and (b) *p* polarized incidences at different incident angles for the multilayer structures in Fig. 4.1 at $\lambda = 522$ nm which is slightly longer than the ENZ wavelength. As the input power increases, the transmission increases due to the change in effective permittivity of the multilayer slab. The power level is independent of the incident angle for the *p*-polarization. It is important to note that ENZ media show bistable behavior in the presence of low loss (inset). This bistability does not exist if we take into account nonlinear absorption i.e. imaginary part of $\chi^{(3)}$.

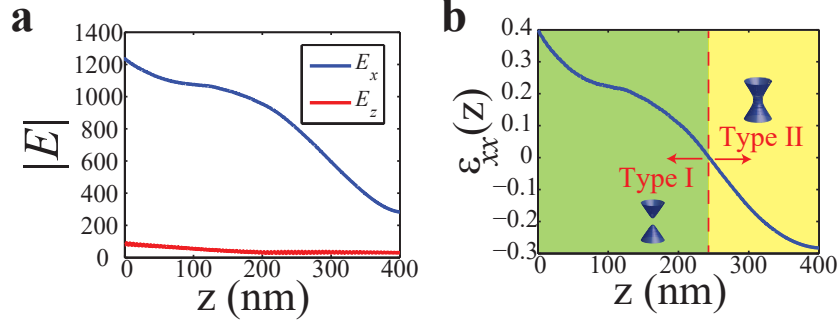


Fig. 4.3. **Optically induced ENZ transition metamaterial.** (a) Electric field distribution for the p polarized incidence when $I_{in}=8$ GW/cm^2 and the incident angle is 45° . Since the operating wavelength is close to the ENZ and epsilon-near-pole (ENP) resonance, ϵ_z is very large which causes the electric field E_z to become very small in comparison with E_x . (b) Nonlinear ENZ transition metamaterials: The nonlinear effective permittivity of the HMM slab when the pump is on. We can see the topological transition from type II to type I occurs as a function of distance (as opposed to wavelength) due to the inhomogeneous power distribution inside the multilayer slab. This shows a unique regime of the multi-layer super-lattice functioning as a transition metamaterial.

Metals have very large Kerr nonlinearity ($\epsilon_{NL} = \epsilon_L + 12\pi\chi^{(3)}|E|^2$ [181, 182] where ϵ_L , $\chi^{(3)}$, and $|E|$ are linear permittivity, Kerr susceptibility, and the electric field amplitude, respectively) which is orders of magnitude larger than that of dielectrics [182]. However, since they are strongly reflective at optical frequencies, the electric field decays very fast inside the bulk metals, so their nonlinearity is not easily accessible [183–185]. Enhancing the nonlinear response of metals in inhomogeneous structures at transparent window has been proposed for applications such as optical limiting [186] and switching of propagating waves [187, 188]. As illustrated in Fig. 4.1.(c), metal/dielectric multilayer structures are transparent in HMM type I region where $\epsilon_{xx} > 0$. Thus, the nonlinear response in that range of frequencies can considerably be enhanced. Furthermore, a small change in permittivity around the ENZ point can lead to a topological transition in HMMs from type II to type I.

To calculate the nonlinear response, we use a finite difference method to discretize the wave equation in structures which are inhomogeneous only in one direction i.e. stratified structures [183]. Nonlinear wave propagation within a stratified medium has been analytically studied only for s polarized incidences [183] and has been approximated for p polarized incidences [188–190]. However, the recent observation of strong nonlinearity at the ENZ wavelengths for p polarized incidences [59] raises the need for a robust analytical formulation to study full-wave nonlinear wave propagation for p polarization as well. We have modified the method proposed by [183] to solve the nonlinear response for p polarized waves.

For an s polarized plane wave propagating through a multilayer structure which is inhomogeneous only in the z direction, the wave equation can be written as: $d^2 E_y(z)/dz^2 + [k_0^2 \epsilon_{NL}(z) - k_x^2] E_y(z) = 0$. This equation can be solved backward by applying appropriate boundary conditions [183]. The nonlinear response of the output power for the multilayer structure is plotted in Fig. 4.2.(a) as a function of the input power. We assume $\chi^{(3)}$ is $2.49 \times 10^{-8} + i7.16 \times 10^{-9}$ esu for silver [187] and it is negligible for TiO_2 . As the input power increases, the transmission increases slowly up to a point and then the transmission soars rapidly. At this threshold, the electric field enhancement effectively flips the sign of ϵ_{NL} from negative to positive. Thus, the structure behaves like a type I HMM. As the incident angle increases, we need higher input power to pass the threshold. If we ignore the imaginary part of $\chi^{(3)}$, which corresponds to the two-photon absorption [181], the nonlinear response at the ENZ threshold is bistable: there are two stable results for the same input (Fig. 4.2.(b) inset). But the bistability does not occur in practice if we take the two-photon absorption into account.

The wave equation for p polarized incidences is more complicated and can be written as:

$$\frac{d^2 E_x(z)}{dz^2} + (k_0^2 \epsilon_{NL}(z) - k_x^2) \frac{k_x^2}{k_0^2 \epsilon_{NL}(z)} \frac{d}{dz} \left[\frac{1}{k_0^2 \epsilon_{NL}(z) - k_x^2} \right] \frac{dE_x(z)}{dz} + (k_0^2 \epsilon_{NL}(z) - k_x^2) E_x(z) = 0, \quad (4.1)$$

$$E_z = \frac{ik_x}{k_0^2 \epsilon_{NL}(z) - k_x^2} \frac{dE_x(z)}{dz}. \quad (4.2)$$

Since ϵ_{NL} depends on both E_x and E_z , the wave equation for the p polarized incidence cannot be solved explicitly as what we did for the s polarization case. However, with a recursive algorithm, accurate result is achievable. The nonlinear response for the p polarized case is plotted in Fig. 4.2.(b). It is seen that the response is almost independent of the incident angle, contrary to the s polarized cases.

Figure 4.3.(a) displays the electric field distribution inside the EMT structure at $\lambda = 500$ nm when $I_{in} = 8$ GW/cm². Since the transmission is not significantly high, the electric field intensity is larger around the input interface. Due to the inhomogeneous field distribution, the permittivity changes inhomogeneously inside the structure. Hence, we can see a transition point at which the effective permittivity sign is flipped (Fig. 4.3.(b)). This type of inhomogeneous metamaterials in which the iso-frequency dispersion curve changes from type II to type I HMMs is known as “transition ENZ metamaterials” [191–193]. This phase change is controlled by the electromagnetic field and is fundamentally different from the natural phase change materials like VO₂ [194]. Note that the operating wavelength of the structure is tunable by changing layers thickness or changing the layer materials.

4.3 Switching of evanescent waves

Propagation of a nonlinear light passing through a multilayer metamaterial slab not only modifies the transmission of the propagating waves, but also changes the tunneling of the evanescent waves through the metamaterial slab. This allows us to control spontaneous emission rate of an emitter near the slab. Figure 4.4 compares

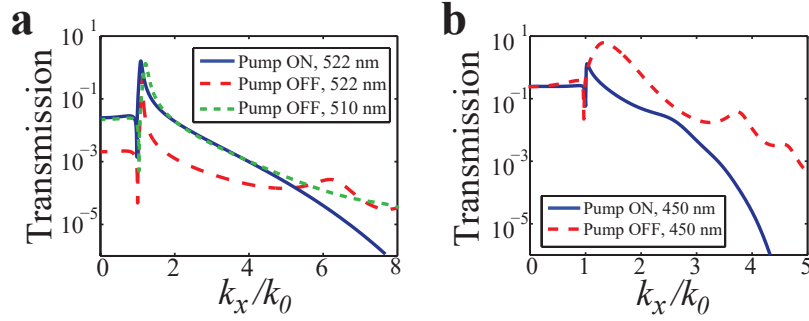


Fig. 4.4. **Effect of nonlinear gate pulse on the linear transmission (a) around and away from the ENZ point.** (a) Transmission of signal through the multilayer medium in the presence of the pump in comparison with that when the pump is off at $\lambda = 522$ nm. The nonlinearity allows us to suppress or enhance transmission of evanescent waves. The nonlinear pulse suppresses the Purcell factor from 41 to around 15. (b) Comparison of the transmission away from the transition point. The nonlinear pulse does not change the transmission for a wide range of wave-vectors. Thus the pump signal does not change the Purcell factor considerably.

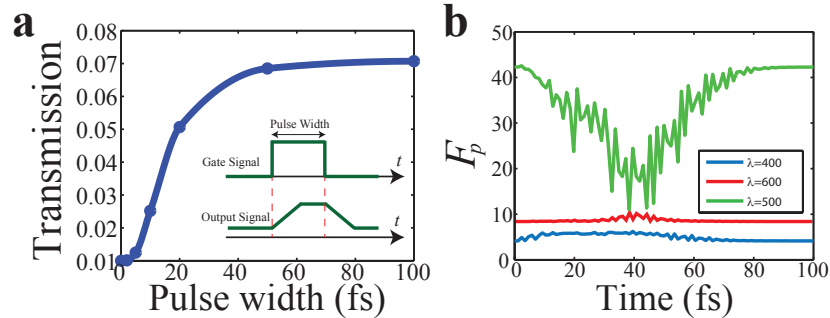


Fig. 4.5. **Nonlinear response of the HMM slab to a finite pulse width.** (a) Nonlinear transmission versus the pulse width at $\lambda = 500$ nm using FDTD method. The electric field amplitude is 10^4 V/m. When the pulse-width is very short, the electric field cannot be distributed in the entire space of the slab, so the pump cannot increase the transmission considerably. As the pulse-width increases, the transmission increases, and it approaches to the steady-state response when the pulse width is longer than 50 fs. (b) The Purcell factor at $\lambda = 500$ nm versus time in the presence of the gate signal. The nonlinear gate signal can switch the Purcell effect. We can see that the change in Purcell factor far away from the ENZ wavelength is negligible.

transmission through the slab with and without the presence of the nonlinear signal near ($\lambda = 522$ nm) and away ($\lambda = 450$ nm) from the ENZ wavelength. The control signal is a p polarized wave at $\lambda = 522$ nm with $I_{in} = 8$ GW/cm² and $\theta = 45^\circ$. An observable change in transmission of both propagating and evanescent waves is seen around the ENZ, and it looks similar to the transmission at a shorter wavelength ($\lambda = 510$ nm) when the pump signal is off. This shows how the nonlinear response due to the control pulse effectively shifts the dispersion of the metamaterial slab around the ENZ. Away from the ENZ, the control pulse does not change the topology of the dispersion curve and hence the change in transmission is not significant for a wide range of wave vectors (Fig. 4.4.(b)). For the case at ENZ, the gate control signal changes the Purcell factor from 41 to around 15. This observable change allows us to control the coupling of the emitted power by a quantum source to the high-k modes of HMMs.

To demonstrate the transient response of the switching process, we have simulated the nonlinear response of the metamaterial in presence of a gate signal with a finite pulse width using a commercial FDTD software [157]. For simplicity, we consider homogenized metamaterial modeled by EMT, and we ignore two photon absorption and the dispersion of $\chi^{(3)}$. The input signal is p polarized and $I_{in} = 8$ GW/cm². The central wavelength of the pulse is at $\lambda = 500$ nm. Figure 4.5.(a) shows the transmission of a normal incident wave as a function of the pulse width. If the pulse width is very short, the electric field cannot influence the entire structure. Thus, the change in the dielectric constant and the nonlinear effect in the transmission is not considerable. Thus, the rise time of the nonlinear response is limited by the material response and the velocity of wave propagation through the HMM slab. As we increase the pulse-width, the transmission increases gradually (Fig. 4.5.(a) inset) and the steady state response is reached when the pulse width is longer than 50 fs. It means that 50 fs is enough for the wave to pass and be distributed in the metamaterial slab and simultaneously change the nonlinear permittivity of the slab. Note that if we consider $\chi^{(3)}$ to be dispersive, the nonlinear dielectric response is

not instantaneous, but the response to the nonlinear pulse can still occur at sub-picosecond scale [58, 59, 195].

Figure 4.5.(b) shows the switching of the Purcell effect as a function of time when the pulse width is 50 fs using the time-dependent nonlinear permittivity derived from the FDTD simulations. More than two-fold Purcell factor reduction is seen near the transition point when the gate pulse is on. The numerical simulations are in good agreement with the analytical calculations. The change in the Purcell factor far away from the transition point is less than 10%. The change in Purcell factor for isotropic media at ENZ is also negligible [196] (See Supplemental Materials). This means that switching of the Purcell effect is only possible around the ENZ wavelength.

4.4 Summary

In conclusion, we have proposed an all-optical nonlinear approach to control the transmission of propagating waves as well as the tunneling of the evanescent waves through an HMM slab around ENZ wavelengths. We have shown that the nonlinear effect is strong enough to change the topology of the HMM slab. This can lead to a significant change in the Purcell factor of a quantum emitter near the slab. We have performed full-wave FDTD simulations to show the effect of pulse-width on the nonlinear response of the slab. The switching can happen at sub-picosecond time scales. Our predicted nonlinear effect is spectrally sensitive and can lead to control of quantum and nonlinear photonic phenomena in the ENZ regime.

5. SUPERCONDUCTING NANOWIRE SINGLE-PHOTON DETECTORS: QUANTUM TIMING JITTER AND SPECTRAL DEPENDENCE OF QUANTUM EFFICIENCY

Superconducting nanowire single-photon detectors have emerged as a promising technology for quantum metrology at mid-infrared to ultra-violet frequencies. Despite the recent experimental improvements, the microscopic mechanism of the detection event in these detectors is not completely known. Here, we propose new criteria for single-photon detection based on single-vortex (flux quanta) crossing the width of the nanowire. Our finite-difference calculations demonstrate that a change in the bias current distribution as a result of the photon absorption significantly increases the probability of single-vortex crossing even if the vortex potential barrier has not vanished completely. We show that the timing uncertainty of this vortex tunneling process corresponds to a fundamental limit in timing jitter of the click event. We demonstrate a trade-space between the timing jitter, quantum efficiency, and dark count rate for three different superconducting materials and different experimental conditions. Our detection model can explain the experimental observation of exponential decrease in the quantum efficiency at lower energies, which leads to a pulse-width dependency in the quantum efficiency. This can be further used as an experimental test to compare across different detection models.

5.1 Outline of the problem

Advancements in quantum technologies strongly depends on improvement in the detection of light at single-photon level. This requires near-unity quantum efficiency, sub-picosecond timing uncertainty (timing jitter), sub-milihertz dark count rate [197],

large bandwidth, and fast recovery [198]. Superconducting nanowire single photon detectors (SNSPDs or SNSPDs) are highly promising detectors in a broad range of frequencies from mid-infrared to ultraviolet [64,65,199–201] with near unity quantum efficiency [202], picosecond-scale timing jitter [67,68,203,204], fast reset time [205], and milihertz dark count rate [2]. They are composed of a thin narrow superconducting wire which is biased slightly below the phase transition critical current and shunted by a readout circuit. To improve the performance of these single-photon detectors, it is required to understand the microscopic mechanism and the trade-space of the photon detection event in these detectors.

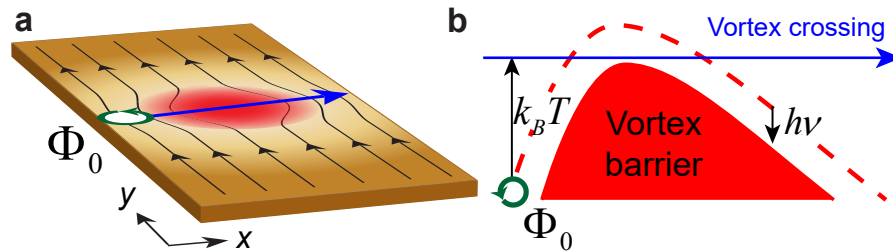


Fig. 5.1. **Superconducting nanowire single photon detectors (SNSPDs).** **a**, When a photon falls on the detector, quasi-particles (QPs) are multiplied and the bias current is redistributed. Vortices are the topological defects of a thin superconductor and are nucleated at the nanowire edge. They can move to the other edge due to the force exerted by the bias current. **b**, Before the photon absorption, the vortex potential barrier does not allow them to move easily. However, due to the QP multiplication and current redistribution, the barrier reduces and vortices can be thermally excited and escape the barrier and cross the width of the nanowire. This process generates a voltage pulse propagating to the two ends of the detector.

Over the past two decades, a few detection models have been proposed to explain the microscopic mechanism of the formation of the first resistive region in SNSPDs [65,66,199,206–208]. In the simplest model, it is assumed that the energy of the absorbed photon increases the temperature at the absorption site leading to the nucleation of a hot-spot which causes the current to bypass to the sides [199,209,210]. This may cause the current at the edge to surpass the critical depairing current and the

formation of a normal conducting region across the width. In another model, the depletion of superconducting electrons around the absorption site is responsible for the formation of the resistive region [211]. Recently, some models have suggested that the motion of vortices or vortex-antivortex pairs can also induce a phase transition at a lower applied bias current [206,208,212–214]. Although each of these models explain some macroscopic behaviors of SNSPDs, none of the current models can explain or predict all experimental observations. Hence, a robust model is needed to address the fundamental limits of SNSPDs and the trade-off between the quantum efficiency, timing jitter, and dark counts.

In this chapter, we demonstrate new criteria for single-photon detection corresponding to the single-vortex crossing from one edge of the nanowire to the other edge. First, we numerically calculate the time-dependent current distribution after the photon absorption and its effect on the vortex potential. We propose that due to the change in the distribution of the conducting electrons, the probability of the vortex crossing is significantly enhanced even if the vortex potential barrier is not vanished completely. Then, we define the detection probability based on the probability of the single-vortex crossing, because the energy released by one vortex moving across the width is enough to induce a phase transition in the superconducting nanowire. We show that the probabilistic behavior of the single-vortex crossing results in a timing jitter on the click event. This timing jitter cannot be eliminated even if the position of photon absorption is known, however, it can be reduced by engineering the structure and the experimental conditions at the cost of a degradation of the quantum efficiency and/or an increase in the dark count rate. Finally, We calculate the quantum efficiency spectrum and show that the quantum efficiency does not suddenly drop to zero when the photon energy is below a threshold. We propose that the response of the detector to the photon pulse-width can be different for different detection models, and the quantum efficiency in our model can strongly be changed as the pulse-width is reduced. This effect has not been predicted by the previous detection models. An experimental test can verify the validity of our model.

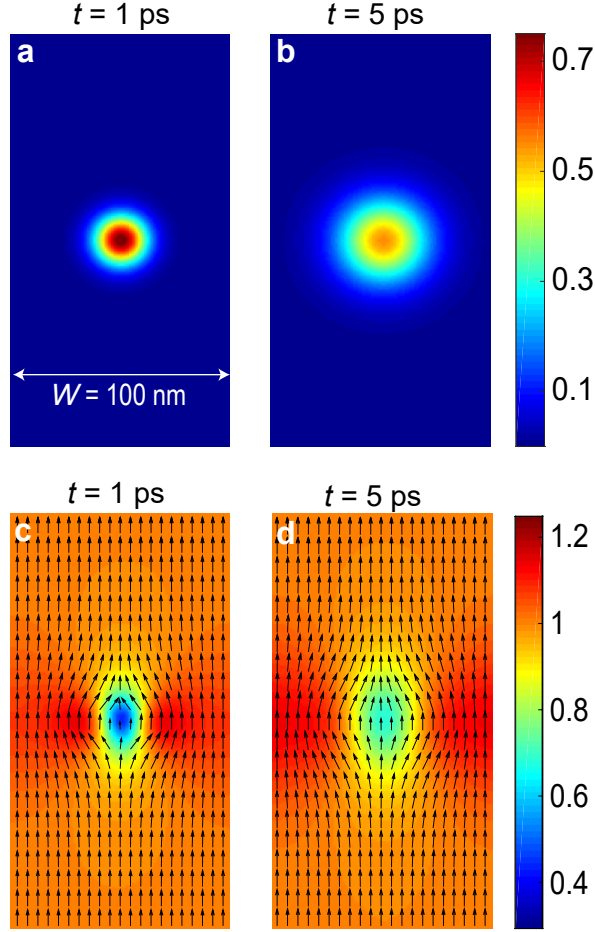


Fig. 5.2. **a**, and **b**, QP distribution, $C_{qp}(\vec{r}, t)$, normalized to the Cooper pair density, $n_{se,0}$, in a TaN SNSPD at $t = 1$ ps and $t = 5$ ps, respectively. It is assumed the photon is absorbed at $t = 0$. $T = 0.6$ °K. The photon energy is $h\nu = 1.5$ eV. The nanowire width, length, and thickness are 100 nm, 1000 nm, and 5 nm, respectively. **c**, and **d**, Normalized Current density in the y direction at $t = 1$ ps and $t = 5$ ps, respectively. The current density is normalized to the applied bias current. The arrows represent the current density vector, $\vec{j}(\vec{r}, t)$. Due to the hot-spot formation, current is redistributed and directed to the side walls.

5.2 Detection mechanism

Detection mechanism in SNSPDs consists of three steps: photon absorption and breaking the superconducting electron pairs (known as Cooper pairs) to quasi-particles

(QPs) and forms a hot-spot; the current density in the detection location is suppressed and directed to the sides as illustrated in Fig. 5.1a; the vortex potential barrier is reduced and vortices can move across the nanowire and release a measurable voltage pulse (Fig. 5.1b). In the following sub-sections, we quantitatively describe these steps.

5.2.1 Quasi-particle multiplication

To find the time-dependent current and QP distributions, we use a modified semi-classical diffusion model which has been originally proposed by Semenov et. al [215] and developed by Engel and Schilling [208, 216]. In this model, we assume the photon energy ($h\nu$) is considerably larger than the superconducting bandgap (Δ), yet not large enough to form a normal conducting core at the position of the photon absorption. Hence, when the photon is absorbed, a hot electron pair with a probability density of $C_e(\vec{r}, t)$ is created and diffuses. Since the photon energy is usually orders of magnitude larger than the bandgap, this hot electron pair breaks a large number (> 100 in the visible range) of Cooper pairs to QPs with a distribution density of $C_{qp}(\vec{r}, t)$. This causes the hot electrons to lose their energy, and as a result, the multiplication process slows down with a life-time of τ_{qp} due to electron-phonon interaction [208]:

$$\frac{\partial C_e(\vec{r}, t)}{\partial t} = D_e \nabla^2 C_e(\vec{r}, t), \quad (5.1)$$

$$\begin{aligned} \frac{\partial C_{qp}(\vec{r}, t)}{\partial t} &= D_{qp} \nabla^2 C_{qp}(\vec{r}, t) - \frac{C_{qp}(\vec{r}, t)}{\tau_r} \\ &+ \frac{\zeta h\nu}{\Delta \tau_{qp}} \left(\frac{n_{se,0} - C_{qp}(\vec{r}, t)}{n_{se,0}} \right) e^{-t/\tau_{qp}} C_e(\vec{r}, t), \end{aligned} \quad (5.2)$$

where D_e , D_{qp} , τ_r , and $n_{se,0}$ are the hot-electron diffusion coefficient, quasi-particles diffusion coefficient, recombination time, and density of superconducting electron pairs (Cooper pairs) before the photon absorption, respectively. ζ is the QP conversion efficiency which has been assumed constant, but the term $(n_{se,0} - C_{qp}(\vec{r}, t))/n_{se,0}$ has been added to include the saturation of QP multiplication. The exact solution of the

above equation in a general form is not easy to derive. Hence, to find the solution numerically, we have used a Finite-Difference Crank-Nicolson method. Since, the hot-electrons diffuse quickly ($D_e \gg D_{qp}$), to speed-up the simulations, we have used the analytical solution of eqn. (5.1) for the case of an infinite 2D superconductor [208]. A grid size of $\Delta x = \Delta y = 1 - 3$ nm and a time step of $D_{qp}\Delta t/\Delta x^2 = 0.01$ is used in our simulations. Neumann boundary condition for the side-walls and zero-flux at the two ends of the nanowire have been considered. The material parameters can be derived from experimental measurements [216, 217]. Figures 5.2a and 5.2b show the distribution of QPs at $t = 1$ ps and $t = 5$ ps, respectively, after a photon with an energy of $h\nu = 1.5$ eV falls at the center of a TaN SNSPD. The nanowire width and length are $W = 100$ nm and $L = 1000$ nm, respectively.

5.2.2 Current redistribution

The current distribution can be calculated by combining superconducting phase coherence condition and continuity equation [218]:

$$\nabla \cdot (\vec{j}(\vec{r}, t)) = \nabla \cdot \left(\frac{\hbar}{m} n_{se}(\vec{r}, t) \nabla \varphi(\vec{r}, t) \right) = 0, \quad (5.3)$$

where $n_{se}(\vec{r}, t) = n_{se0} - C_{qp}(\vec{r}, t)$ is the density of superconducting electrons after the photon absorption, φ is the phase of the superconducting order parameter, m and \hbar are the electron mass and reduced Planck constant, respectively. Figures 5.2c and 5.2d display the current density normalized to the bias current. It is seen that due to the hot-spot formation at the center, the current is directed to the side-walls of the nanowire.

5.2.3 Single vortex crossing

Vortices and antivortices are the topological defects in thin superconducting films which exist even if there is no applied magnetic field [218]. Vortices are usually nucleated and enter into the nanowire from the edge where the superconducting order

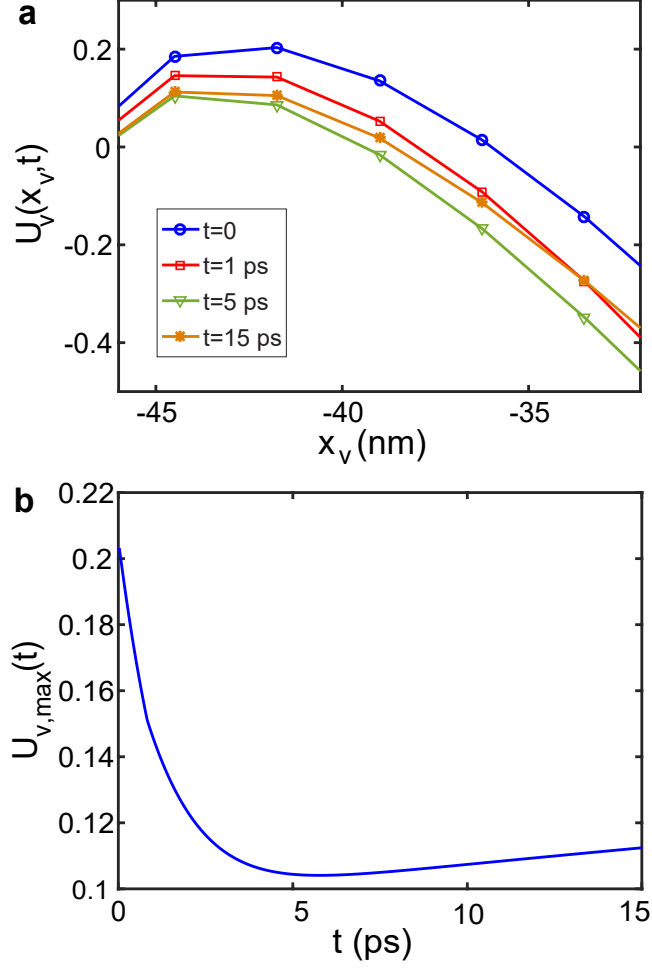


Fig. 5.3. **Vortex barrier dynamics** **a**, Vortex potential as a function of the vortex location (x_v) around the saddle point after the photon absorption for a TaN SNSPD. The photon energy and structure parameters are the same as those in Fig. 5.2. **b**, Potential barrier peak as a function of time. A change in the Cooper pairs density and current distribution reduce the barrier height.

parameter is suppressed. London equation in the presence of a static vortex in a superconducting thin film in xy plane can be written as [218, 219]:

$$\vec{H}(r) + 2\pi\frac{\Lambda}{c}\nabla \times \vec{j}(r) = \hat{z}\Phi_0\delta(\vec{r} - \vec{r}_v), \quad (5.4)$$

where $\Lambda = 2\lambda^2/d$ is the Pearl length [220], λ is the London penetration depth, d is the film thickness, $\Phi_0 = hc/2e$ is the magnetic flux quantum due to the presence of

a single-vortex at the position \vec{r}_v , \vec{H} is the magnetic field, \vec{j} is the current density ignoring the effect of the vortex on the current, and c is the speed of light in vacuum. Since the thickness of the nanowire is significantly smaller than λ , we have averaged the field and the current in the z direction. For nanoscale SNSPDs ($L \ll \lambda$), the first term can be neglected [219], and because of the current continuity ($\nabla \cdot \vec{j} = 0$), we can write the current density in the form of a scalar function as $\vec{j}(r) = \nabla \times G(r)\hat{z}$. Thus, Eqn. (5.4) is reduced to [219]:

$$\nabla^2 G(r) = -\frac{c\Phi_0}{2\pi\Lambda} \delta(\vec{r} - \vec{r}_v), \quad (5.5)$$

which is equivalent to the 2D Poisson's equation for a charged particle. For an infinite superconducting film case, the interaction energy between vortices and antivortices for distances shorter than the Pearl length is logarithmic. This allows Berezinskii-Thouless-Kosterlitz (BKT) transition and the formation of vortex-antivortex pairs below the BKT critical temperature [219, 221]. However, for a thin superconductor with finite width ($-W/2 < x < W/2$), the long range interaction between vortices and antivortices is eliminated and single vortices can be found. For a single vortex, eqn. (5.5) is reduced to the equation for a charge sandwiched between two parallel grounded plates. The problem is well-known in electrostatics and can be solved using conformal mapping with $z' = e^{i\pi z/W}$ transformation and using image theory [219]:

$$G(x, y) = \frac{c\Phi_0}{8\pi\Lambda} \ln \frac{\cosh(y\pi/W) + \cos((x+x_v)\pi/W)}{\cosh(y\pi/W) - \cos((x-x_v)\pi/W)}, \quad (5.6)$$

where we have assumed the vortex is placed at $x = x_v$ and $y = 0$. The phase of the order parameter, φ , can also be derived from G since the gradient of φ is also proportional to the current [213]:

$$\varphi(\vec{r}, \vec{r}_v) = \tan^{-1} \frac{\cos\left(\frac{\pi x}{W}\right) \sinh\left(\pi \frac{y-y_v}{W}\right)}{\sin\left(\frac{\pi x}{W}\right) - \cosh\left(\pi \frac{y-y_v}{W}\right) \sin\left(\frac{\pi x_v}{W}\right)}. \quad (5.7)$$

The free energy in presence of a vortex consists of the field energy and the kinetic energy inside the nanowire and the field energy outside [218, 219]. If we assume the

vortex core radius is ξ and we neglect the core energy of the vortex, the self-energy of the vortex can be written as [207]:

$$\begin{aligned} U_v^0(x_v) &= -\frac{\Phi_0}{2c}G(|x - x_v| \rightarrow \xi, 0) \\ &= \frac{\Phi_0^2}{8\pi^2\Lambda} \ln\left(\frac{2W}{\pi\xi} \cos\left(\frac{\pi x_v}{W}\right)\right), \end{aligned} \quad (5.8)$$

If we include the work done by the bias current on a single vortex due to the Magnus force (dual of the Lorentz force on a magnetic flux), the total energy of a single vortex is expressed as [213]:

$$U_v(x_v) = \frac{\Phi_0^2}{8\pi^2\Lambda} \ln\left(\frac{2W}{\pi\xi} \cos\left(\frac{\pi x_v}{W}\right)\right) - \frac{\Phi_0}{c} j_y(x_v) x_v. \quad (5.9)$$

The Magnus force tries to move the vortex in the direction perpendicular to the direction of the applied bias current, but it cannot overcome the self-energy of the vortex if the bias current is not high enough. Increasing the bias current at the edges $j_y(x_v, t)$ due to the photon absorption reduces the potential barrier and eases vortex crossing. This barrier finally turns to zero at the vortex critical current which is:

$$I_{c,v} = \frac{c\Phi_0}{4\pi^2 \exp(1)\Lambda\xi} W. \quad (5.10)$$

As seen in eqn. (5.7), the phase of the order parameter depends on the position of the vortex, x_v , and the phase difference at the two ends of a long nanowire ($L \gg W$) away from the vortex position can be approximated as:

$$\varphi(L/2) - \varphi(-L/2) = 2\pi x_v/W. \quad (5.11)$$

Hence, as the vortex moves across the width of the nanowire, it applies a time-dependent phase difference between the two terminals of the detector. If the vortex crosses from one edge at $x_v = -W/2$ to another edge at $x_v = W/2$, it causes a 2π phase-slip at the two ends of the nanowire. This phase evolution generates a voltage pulse which can be described by Josephson effect [222]:

$$V(t) = \frac{\Phi_0}{2\pi c} \frac{d}{dt} (\varphi(L/2) - \varphi(-L/2)) = \frac{\Phi_0}{cW} \frac{dx_v}{dt}. \quad (5.12)$$

This voltage pulse propagates to the two ends [201, 223] and is dissipated in the presence of the bias current. If the bias current is high enough, the released energy is enough to induce a phase transition in the nanowire from the superconducting state to the normal conducting state. Hence, the current $I_{c,v}$, which makes the vortex tunneling barrier reduce to zero, is also the critical current for phase transition in a thin superconducting nanowire. This critical current is less than the depairing critical current in a bulk superconductor, $I_{c,dep}$, [66, 208]. Breaking of the Cooper pairs and redistribution of the bias current due to the photon absorption also changes the potential barrier [208]:

$$\begin{aligned} \frac{U_v(x_v, t)}{\varepsilon_0} = & -\frac{\pi}{W} \int_{\frac{\xi-W}{2}}^{x_v} \frac{n_{se}(x', t)}{n_{se,0}} \tan\left(\frac{\pi x'}{W}\right) dx' \\ & - \frac{2W}{I_{c,v} \exp(1)\xi} \int_{-\frac{W}{2}}^{x_v} \frac{n_{se}(x', t)}{n_{se,0}} j_y(x', t) dx', \end{aligned} \quad (5.13)$$

where $\varepsilon_0 = \Phi_0^2/8\pi^2\Lambda$ is the characteristic vortex energy. As shown in Fig. 5.3, this can reduce the potential maximum as the hot-spot expands.

After the single-photon transduction, several processes compete with each other to form the initial normal conducting cross-section. Depending on which one occurs first, different detection models have been proposed. In hot-spot model, it is assumed that the formation of hot-spot is responsible for the phase transition [199, 210]. Nucleation of the hot-spot causes the bias current to be directed to the side-walls. If the current density at the edge surpasses the depairing critical current ($I_{edge} \geq I_{c,dep}$), it induces a phase transition to the normal conducting state at the edge and the normal conducting region expands across the width.

In QP model, there is no need to destroy the superconductivity by surpassing the critical current [211]. If the Cooper pairs are depleted inside a volume with a thickness of at least one coherence length (ξ -slab), the phase coherence is destroyed which results in a phase transition. This requires the number of QPs inside the ξ -slab (N_{QP}^{slab}) to exceed the number of the superconducting electrons inside the ξ -slab: $N_{QP}^{slab}/N_{se}^{slab} \geq 1 - I_b/I_{c,dep}$, where N_{se}^{slab} is the initial superconducting-electron number inside the slab before applying the bias current (I_b).

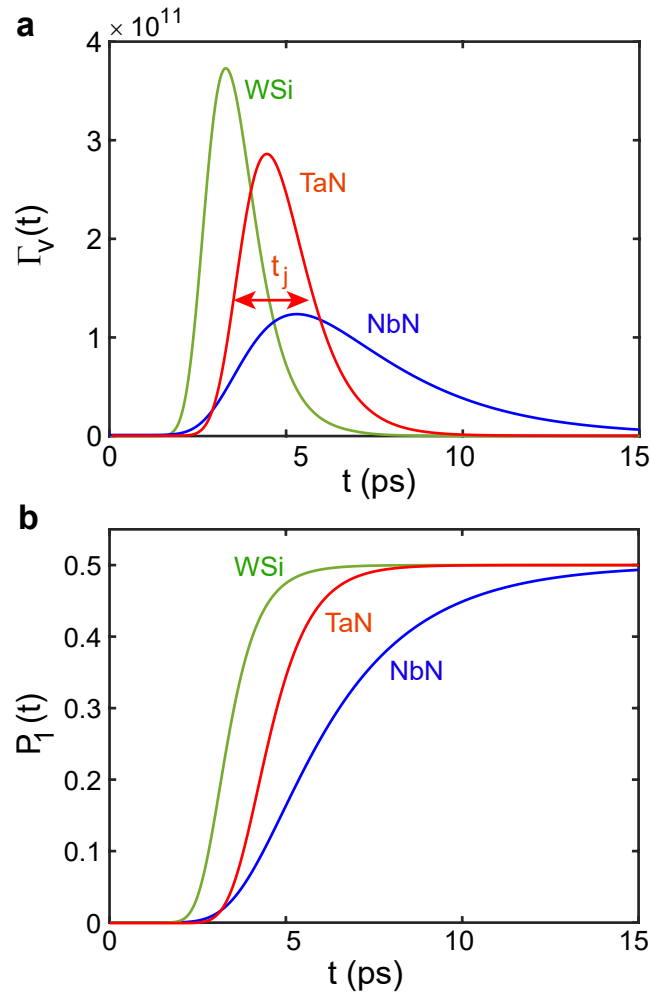


Fig. 5.4. **Vortex crossing rate and probability.** **a**, Single-vortex crossing rate as a function of time for NbN, TaN, and WSi SNSPDs. The bias current has been set to achieve a single photon detection probability of 0.5 for a photon energy of $h\nu = 1.5$ eV. The geometry is the same as that in Fig. 5.2. The enhancement in the vortex crossing rate is as a result of the suppression of the potential barrier. The probability of vortex crossing at the maximum rate is higher. However, there is considerable uncertainty in the vortex crossing time which results in a timing jitter in detection event. **b**, The evolution of vortex crossing probability as the vortex crossing rate changes. There is a step change in the probability as the crossing rate goes up.

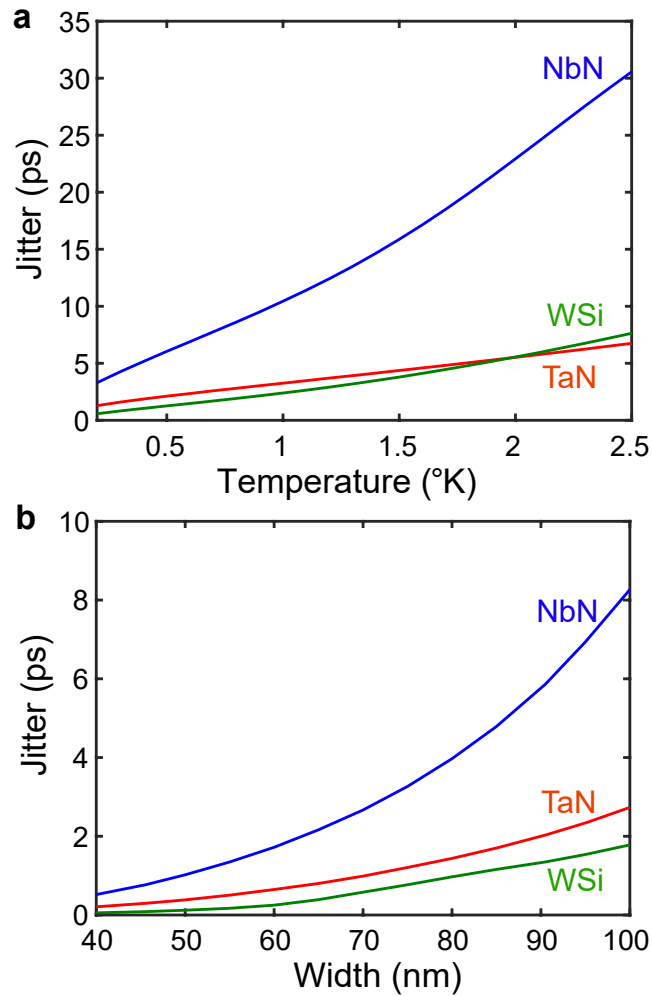


Fig. 5.5. **Timing jitter corresponding to vortex crossing.** Timing jitter in NbN, TaN, and WSi SNSPDs as a function of (a) temperature and (b) nanowire width. The other parameters are the same as that in Fig.5.4. Decreasing the temperature results in a sharper change in the vortex crossing rate. Hence, the uncertainty of vortex crossing reduces. Reducing the width of the nanowire causes that the QPs to distribute faster across the width of the nanowire, and as a result, the potential barrier reduces rapidly.

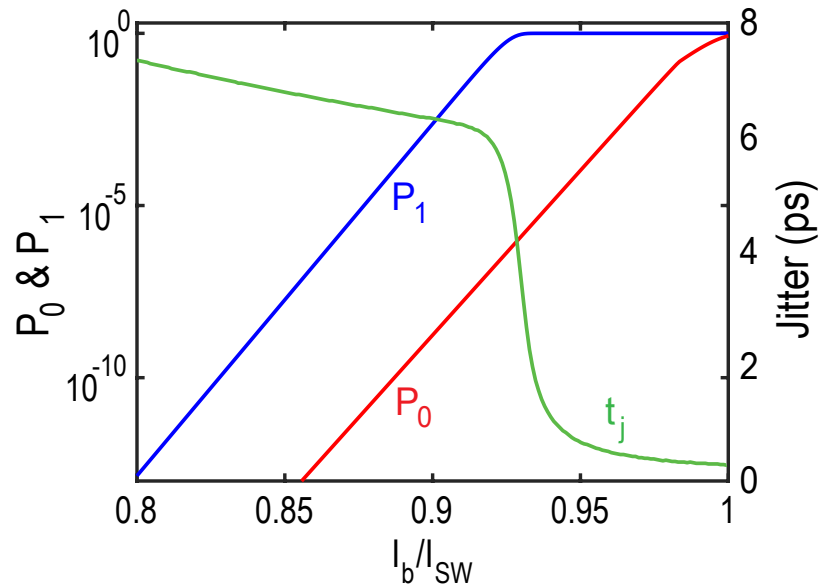


Fig. 5.6. **The effect of bias current on TaN SNSPD performance.** **a**, Timing jitter, dark count probability (P_0), quantum efficiency (P_1) versus the bias current (I_b). I_b is normalized to the switching current (I_{SW}) which is defined as the minimum bias current at which the detector clicks in the time-bin of the single-photon arrival even if the photon is not absorbed. Note that I_{SW} is smaller than $I_{c,v}$. Increasing the bias current helps to improve the detection probability and the timing jitter but at the cost of an increase in the dark count probability. The detector parameters are the same as those in Fig. 5.2.

Vortices can also be responsible for the trigger of a single-photon induced phase transition in SNSPDs. If the photon transduction causes the vortex potential barrier to vanish, vortices move across the width and induce a phase transition [207, 208]. In the next section, we show that even if the barrier is not completely vanished and the kinetic energy of the vortices is not enough to surmount the barrier, there is a considerable probability of single-vortex crossing. This quantum tunneling process causes a new source of timing jitter for the detection event.

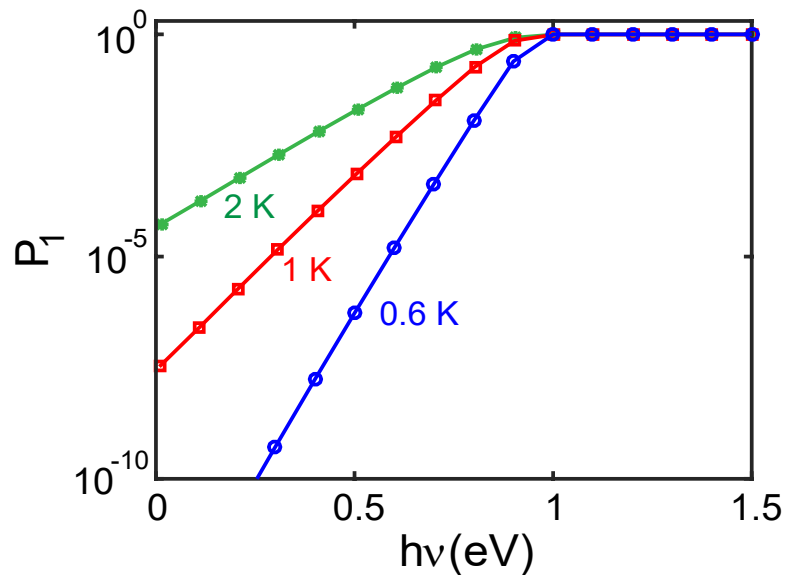


Fig. 5.7. **Single-photon detection probability (quantum efficiency) as a function of single-photon energy in TaN SNSPDs.** The bias current is set to have near unity detection probability when the photon energy is larger than 1 eV. Other parameters are the same as those in Fig. 5.2. The exponential tail corresponds to the vortex escaping rate while the potential barrier has not vanished completely. As the temperature rises, the probability of vortex crossing increases even if the photon energy is not enough to reduce the potential barrier considerably.

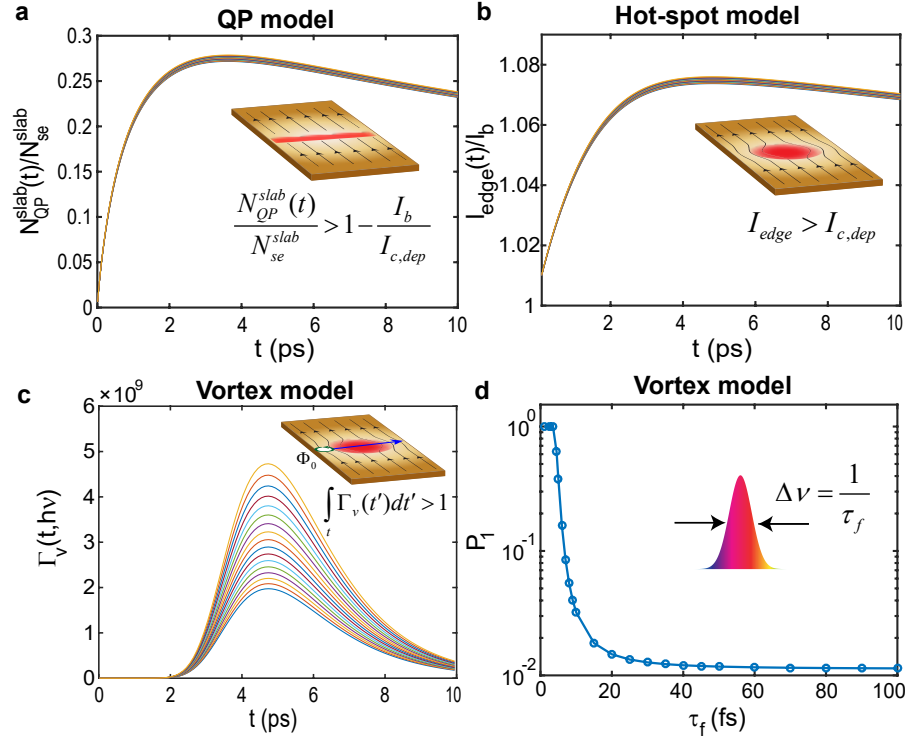


Fig. 5.8. **Pulse-width dependent quantum efficiency in different models.** **a**, Normalized QP numbers inside the ξ -slab, **b**, normalized current density at the edge, and, **c**, vortex crossing rate for different modes in a pulse with pulse width of $\tau_f = 100$ fs and the central energy of $h\nu = 0.75$ eV. It is seen that the number of QPs and current at the edge is not very sensitive to the small change of the photon energy. However, the single-vortex crossing rate is extremely sensitive as a result of a few percent change in the photon energy. **d**, Single-photon quantum efficiency versus the pulse-width in vortex model. The quantum efficiency is considerably increased for the very short pulses.

5.3 Quantum timing jitter corresponding to the single-vortex crossing

Even if there is no photon and the bias current is below the critical current $I_{c,v}$, a vortex can be thermally excited and escape the potential barrier saddle point and forms a normal conducting belt [217]. This false-count rate is known as dark-count rate which deteriorates the performance of a single-photon detector [198]. The time-dependent rate of the vortex crossing can be described as:

$$\Gamma_v(t) = \alpha_v I_b \exp(-U_{v,\max}(t)/k_B T), \quad (5.14)$$

where k_B is the Boltzmann constant and α_v is a constant which is measured experimentally [217]. The reduction of the vortex potential barrier as a result of the photon absorption exponentially increases the rate of the vortex crossing. Figure 5.4a shows the vortex tunneling rate after the photon absorption as a function of time for three different materials. The rate at $t = 0$ corresponds to the dark-count rate [217, 224–226]. However, the rate is enhanced several orders of magnitude when the potential barrier reaches its minimum. This enhancement during the multiplication and recombination of QPs might be enough to guaranty escaping of at least one vortex and crossing across the width of the nanowire. It is seen that the shape of the vortex crossing rate is different in different materials depending on how fast the QPs are multiplied, diffused across the width, and recombined. Since the crossing of vortices occurs independent of the other vortices, the crossing events can be regarded as a Poisson process with distribution function,

$$p(n_v, t) = \frac{\bar{n}_v(t)^{n_v}}{n_v!} e^{-\bar{n}_v(t)} \quad (5.15)$$

characterizing the probability of n_v vortex crossing the nanowire during the time interval $[t_0, t]$. Here, the time-dependent function $\bar{n}_v(t) = \int_{t_0}^t \Gamma_v(t') dt'$ is the mean number of vortices crossing the nanowire. Hence, we can define the single-photon detection probability P_1 after the single-photon absorption ($t_0 = 0$) and before time t as the probability of crossing of at least one vortex as:

$$P_1(t) = 1 - p(0, t) = 1 - \exp\left[-\int_{t_0=0}^t \Gamma_v(t') dt'\right]. \quad (5.16)$$

As seen in Fig. 5.4b, the detection probability increases rapidly around the crossing rate maximum. The time derivative of $P_1(t)$ is proportional to the single-photon count rate (also known as instrument response function) measured in experiments [67]. If the detection efficiency is low, the photon count rate is the same as $\Gamma_v(t)$. The rise time of the quantum efficiency is not instantaneous due to the finite diffusion speed of the QPs and the hot-spot formation. Hence, there is a fundamental uncertainty in time of the quantum vortex tunneling. This causes a quantum timing jitter (t_j) on photon detection event corresponding to the rise time and fall time of the single vortex crossing rate as illustrated in Fig. 5.4a.

This type of timing jitter is because of the probabilistic crossing of vortices [227, 228] and unlike the geometrical and spatial sources of timing jitter, cannot be eliminated if the uncertainty in the position of the transduction event is reduced [229–233]. However, it can be controlled by engineering the structure and controlling the experimental conditions. It is seen in eqn. (5.14) that as the temperature decreases, the change in the vortex crossing rate becomes sharper. This causes the timing jitter to reduce as shown in Fig. 5.5a. However, the temperature cannot go to zero because QPs do not diffuse at zero temperature. Note that smaller vortex energy ε_0 , as seen in eqn. (5.14), causes a slow change in the vortex crossing rate, similar to the effect of rising the temperature. Hence, although the hot-spot formation and relaxation happens faster in WSi due to the smaller bandgap and faster QP diffusion [216], the timing jitter in WSi is comparable with that in TaN because of the smaller ε_0 in WSi nanowires.

Reducing the width of the nanowire results in a faster distribution of the hot-spot across the nanowire width. This leads to a sudden change in the vortex potential barrier, and as a result, the timing jitter decreases considerably as shown in Fig. 5.5b. Reducing the width helps reducing the geometrical timing jitter as well [229], however, at the cost of a decrease in the transduction efficiency of the device.

Increasing the bias current reduces the vortex potential and increases the vortex crossing rate. This causes an increase in the quantum efficiency (P_1) [234, 235], yet

also an increase in the dark count probability (P_0) as shown in Fig. 5.6. P_0 is defined as the probability of the click while there is no interaction between the photon and the detector in the time bin of the photon arrival. I_{SW} is defined as the minimum bias current which is required for at least one vortex to escape the barrier in that time bin. Note that I_{SW} can be smaller than $I_{c,v}$, especially if the temperature is not low enough. The bias current has also a significant impact on the timing jitter corresponding to single-vortex crossing. If the detector is biased very close to the switching current, a small perturbation due to the single-photon absorption suppresses the potential barrier and vortex can across the width. Figure 5.6 displays the effect of the bias current on the timing jitter as well. It is seen that the timing jitter drops remarkably when the quantum efficiency approaches unity. This is because of the significant suppression of the barrier which leads to the vortex crossing even before the rate reaches to its maximum. The same trend has recently been observed in experiment [68]

5.4 Energy-dependence and pulse-width dependence of the quantum efficiency

Figure 5.7 shows the quantum efficiency based on the single-vortex crossing model as a function of the single-photon energy at different temperatures. The quantum efficiency approaches P_0 When the photon energy goes to zero. As the photon energy goes up, more QPs are generated. This causes more suppression of the vortex potential barrier which leads to a higher quantum efficiency. The bias current is set to have a near unity quantum efficiency when the photon energy is larger than 1 eV. Our vortex model by itself can explain both constant efficiency at high energies and exponential decrease of quantum efficiency at lower energies seen in experiments [236,237]. Note that the photon absorption efficiency is assumed to be one. In practice, to increase the absorption efficiency, the detector should be placed inside a high-Q cavity [238–240] or a low-mode volume waveguide [44, 202, 241–243] to enhance the spatial overlap

between the optical mode of the incoming photon and the superconducting electrons of the detector.

Increasing the quantum information processing speed requires to enhance the photon bandwidth. Till now, we have assumed the incoming photon is single-mode. However, in practice, the photon has a finite pulse-width. In Fig. 5.8, we have compared the response of different quantities to different models of superconducting phase transition induced by a single-photon pulse at central energy of $h\nu = 0.75$ eV with a pulse width of $\tau_f = 100$ fs. Number of QPs and current at the edge, are the main quantities to define detection criteria in hard-core model and QP model [208]. As shown in Fig. 5.8a and 5.8b, the detector is not very sensitive when the photon energy is changed around the central frequency of the photon. However, a considerable change in single-vortex crossing rate is seen in Fig. 5.8c because the rate exponentially changes by the potential barrier. Figure 5.8d displays the effect of pulse width on the quantum efficiency in our model. This effect arises due to the exponential tail of the quantum efficiency and clearly differentiates the proposed vortex model from the existing detection mechanisms. A controlled experiment can verify whether our model is correct or not.

5.5 Summary

In summary, we have proposed detection criteria in SNSPDs based on a single-vortex moving across the width of the detector. We have shown that when the photon is absorbed, the Cooper pairs break into QPs and they change the bias current distribution. This causes a potential barrier, which impedes vortices to move, to be reduced but not necessarily to be vanished completely. This can lead to a significant enhancement in the rate of the escaping of vortices over the barrier. We have shown that this non-deterministic process insets a considerable timing jitter to the click event. We have shown the trade-space of the timing jitter, quantum efficiency, and dark counts for different materials and different nanowire structures. We have pre-

sented the quantum efficiency spectrum based on our model, and based on that, we can predict a pulse-shaped dependent quantum efficiency in SNSPDs. This effect is negligible in other proposed models, and it can be verified experimentally to confirm or reject the model.

APPENDICES

A. ADDITIONAL RESULTS FOR TRANSPARENT SUB-DIFFRACTION OPTICS

A.1 Relaxed total internal reflection

We look for the solution for light confinement using the rules of transformation optics (TO) which state that Maxwell's equations written in a transformed coordinate system preserve their original form if the material parameters are renormalized. We introduce the concept of transforming optical momentum- the physical quantity which governs whether a wave propagates or decays in a medium. We emphasize that this approach, in contrast with previous approaches which primarily dealt with propagating waves, allows control over evanescent waves which is necessary for waveguiding. If a Cartesian mesh in a region of empty space is transformed according to $x' = f_1(x)$, $y' = f_2(y)$, $z' = f_3(z)$ the optical momentum of propagating or evanescent waves in the region is then transformed to:

$$\frac{k_{x'}^2}{h_x^2} + \frac{k_{y'}^2}{h_y^2} + \frac{k_{z'}^2}{h_z^2} = k_0^2 \quad (\text{A.1})$$

where $k_0 = 2\pi/\lambda$ is the free space wavevector and the coordinate transformation is characterized by the Jacobian matrix $diag[\partial f_1/\partial x, \partial f_2/\partial y, \partial f_3/\partial z] = diag[h_{x'}, h_{y'}, h_{z'}]$, the transformed wavevector $\vec{k}' = [k_{x'}, k_{y'}, k_{z'}]$. The optical momentum transformation, on comparison with the dispersion relation for vacuum, is found to be $k_{x'} = h_x k_x$, $k_{y'} = h_y k_y$ and $k_{z'} = h_z k_z$. The transformation of optical momentum is a general technique and is valid for arbitrary homogeneous media which support plane wave solutions. However, the boundary conditions related to continuity of tangential momenta are sensitive to the curvature and roughness of the boundary. In this paper, we use the continuity of tangential momenta across smooth interfaces in both the 1D and 2D cases. We now revisit the conventional light guiding mechanism of total in-

ternal reflection at the interface of two dielectrics using momentum transformations. A plane wave travelling in vacuum (region I) is partially reflected back at $x = 0$ because there is a discontinuity in the “electromagnetic grid” representing optical space (Fig. 1). Electromagnetic boundary conditions require the tangential momentum and hence the phase to be continuous across this interface ($k_{z1} = k_{z2}$). For a given wave incident in a particular direction with $\vec{k} = [k_{x1}, k_{y1}, k_{z1}]$, the ray can be completely reflected back if the transformed momentum in the tangential direction k_{z1}/h_z exceeds the maximum possible momentum in the medium ($k_{z1}^2/h_z^2 > k_0^2$) (Fig. 1.a). This causes the wave to decay away along the x -direction in region $x > 0$. Since $k_{z1} < k_0$, we arrive at the condition for the possibility of total internal reflection that the transformation should be such that $h_z < 1$. We note that this condition is different from the well-known condition of $n_1 > n_2$ as a condition for total internal reflection of light moving from medium 1 to 2. When the second medium is uniaxial and the optical axis is perpendicular to the interface, the condition is in fact reduced to

$$n_1 > n_{2x}. \quad (\text{A.2})$$

Eqn. A.2 holds for the incident angle (θ) greater than $\theta_c = \sin^{-1}(n_{2x}/n_1)$, where $\begin{bmatrix} n_{2x} & n_{2z} & n_{2z} \end{bmatrix}$ is the refractive index tensor of the second medium and x axis is normal to the interface. The interface lies in the $y - z$ plane. We termed this condition as relaxed total internal reflection (relaxed-TIR) [10] since it leaves a degree of freedom unexplored: the perpendicular component of the dielectric tensor.

For this set of transformations that cause total internal reflection, the wave extends evanescently into the second medium. Note that the total internal reflection is governed by the momentum transformation only in the z direction and not the x direction. Using this additional degree of freedom, we transform the optical momentum of evanescent waves to lead to enhanced confinement of the wave in the region with $x > 0$ (Fig. A.1b). We choose a transformation that compresses the optical grid along the x direction with $h_x \gg 1$. This increases the momentum of the wave along the x direction and hence causes a faster decay of evanescent waves in region II.

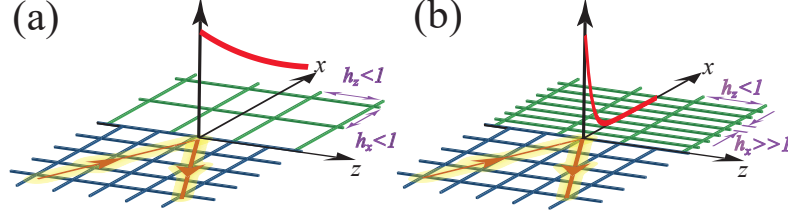


Fig. A.1. **The phenomenon of refraction and reflection revisited using transformation of optical momentum.** Rays of light are reflected and refracted at an interface since the mesh representing electromagnetic space has a discontinuity. (a) Total internal reflection can be viewed as a transformation of optical momentum. When grid sizes in the second medium become large enough, the incident ray is totally reflected and evanescently decays in the second medium. (b) Only one component of the dielectric tensor controls the total internal reflection condition. By transforming the space in the other direction, we can control the momentum of evanescent waves and consequently decrease penetration depth in the second medium.

Note that this momentum transformation is valid for both polarizations but requires optical magnetism which is difficult to achieve. For non-magnetic media and TM polarized light, we can arrive at an all-dielectric condition

$$n_{2z} \gg 1 \quad (\text{A.3})$$

to increase the momentum of evanescent waves i.e. make them decay faster confining them very close to the interface (Fig A.1b). The skin depth for transparent media at TIR in the second medium is defined as:

$$\delta(\theta) = \frac{1}{k_{2x}} = \frac{n_{2x}}{n_{2z}} \frac{1}{2k_0 \sqrt{(n_1 \sin(\theta))^2 - n_{2x}^2}} \quad (\text{A.4})$$

which immediately reveals that by increasing n_{2z} , we can confine the evanescent wave decay in the second medium (k_{2x}) and hence reduce its skin depth (δ).

Note that we have decoupled the total internal reflection criterion ($n_1 > n_{2x} = \sqrt{\varepsilon_{2x}}$) from the momentum transformation condition ($n_{2z} \gg 1$) so they can be achieved simultaneously leading to a fundamentally new approach to light confinement in transparent media (Fig. A.1). In essence, our non-resonant transparent

medium alters the momentum of light entering it and we emphasize that the above set of transformations can be achieved by all-dielectric media ($n > 1$).

A.2 1D Extreme-skin-depth Waveguides

For an infinite slab waveguide in which the wave propagates in the z direction, the conditions to satisfy total internal reflection and fast decaying in the cladding are: $h_z < 1$ and $h_x \gg 1$. Since for the TM modes in slab waveguides only y component of the magnetic field is non-zero, the magnetic field does not feel the anisotropy. Thus we can achieve the momentum transformation with non-magnetic anisotropic metamaterials. The magnetic field is defined as:

$$H_y = \begin{cases} A \cos(k_{x1}x) e^{i\beta z}, & |x| < a \\ B e^{-k_{x2}x} e^{i\beta z}, & |x| > a \end{cases} \quad (\text{A.5})$$

where A and B are constants and obtained by matching boundary conditions and excitation, and k_{xi} ($i = 1, 2$) and β are the wave vector components in the perpendicular and parallel to the propagation direction, respectively. When the second medium is anisotropic dielectric, the electric field components are derived from Maxwell equations as:

$$\begin{aligned} E_x &= \frac{1}{i\omega\varepsilon_0\varepsilon_x} \frac{\partial H_y}{\partial z} = \frac{\beta}{\omega\varepsilon_0} \begin{cases} \frac{A}{\varepsilon_1} \cos(k_{x1}x) e^{i\beta z}, & |x| < a \\ \frac{B}{\varepsilon_{x2}} e^{-k_{x2}x} e^{i\beta z}, & |x| > a \end{cases} \\ E_z &= \frac{-1}{i\omega\varepsilon_0\varepsilon_z} \frac{\partial H_y}{\partial x} = \frac{1}{i\omega\varepsilon_0} \begin{cases} \frac{Ak_{x1}}{\varepsilon_1} \sin(k_{x1}x) e^{i\beta z}, & |x| < a \\ \frac{Bk_{x2}}{\varepsilon_{z2}} e^{-k_{x2}x} e^{i\beta z}, & |x| > a \end{cases} \end{aligned} \quad (\text{A.6})$$

where ε_1 is the first medium permittivity and ε_{x2} and ε_{z2} are the x and z components of second medium permittivity. Since the structure is invariant in the y direction, other field components are zero. The isofrequency dispersion relations for the two mediums are:

$$\begin{cases} \beta^2 + k_{x1}^2 = k_0^2 \varepsilon_1 \\ \beta^2 - \left(\frac{k_{x2}}{\gamma}\right)^2 = k_0^2 \varepsilon_{x2} \end{cases} \quad (\text{A.7})$$

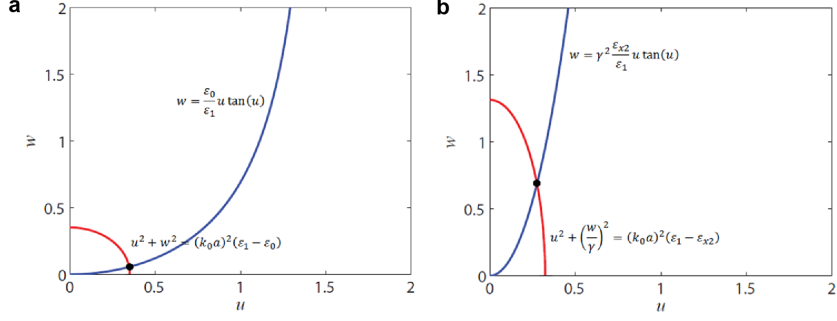


Fig. A.2. The graphical solution of (A.8) for the glass slab waveguide with a size of $\lambda_0/10$ and (a) air cladding (b) anisotropic cladding ($\epsilon_x=1.2$ and $\epsilon_z=20$). The solution moves to higher w (more confinement) without a large change in u .

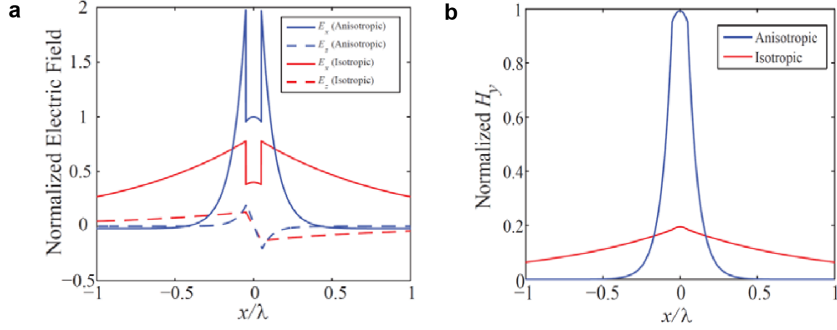


Fig. A.3. Electromagnetic field profile for glass slab waveguide with a size of $\lambda_0/10$ and anisotropic cladding ($\epsilon_x=1.2$ and $\epsilon_z=15$) in comparison with the same waveguide without cladding. (a) Electric field. (b) Magnetic field. Field amplitudes are normalized to the same input energy. Fields decay faster in the anisotropic cladding.

where $\gamma^2 = \frac{\epsilon_{z2}}{\epsilon_{x2}}$. By applying boundary conditions and combining the two equations in (A.7), we obtain two coupled equations for determining wave vectors:

$$\begin{cases} w = \gamma^2 \frac{\epsilon_{x2}}{\epsilon_1} u \tan(u) \\ u^2 + \left(\frac{w}{\gamma}\right)^2 = (k_0 a)^2 (\epsilon_1 - \epsilon_{x2}) \end{cases} \quad (\text{A.8})$$

where $u = k_{x1}a$ and $w = k_{x2}a$. This set of equations can be solved graphically to find components of the wave vectors. Fig. A.2 shows the graphical solution for the first even TM mode. The point where two equations in (A.8) intersect is the result. The

plot in Figs. A.2a and b are for the case in which the core is glass ($\varepsilon_1=2.25$) with size of $2a-\lambda/10$ and the cladding is air and anisotropic dielectric ($\varepsilon_{x2} = 1.2$ and $\varepsilon_{z2} = 20$), respectively. It is clearly observable that the anisotropic cladding leads upscaling of w without a noticeable change in u . An increase in w means faster decaying of the fields in the cladding and consequently more energy confinement inside the core. The electric and magnetic field profiles are plotted in Fig. A.3 in comparison with the same waveguide without cladding. It is seen that the fields decay fast in the anisotropic cladding.

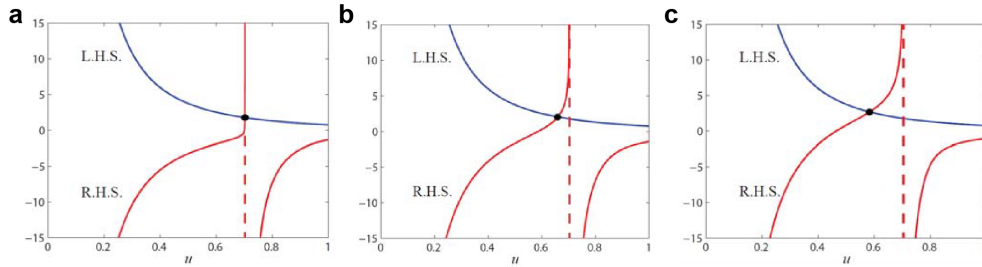


Fig. A.4. The graphical solution by intersecting the left and right hand side of (A.13) and (A.17) for a cylindrical waveguide with glass core whose radius is $\lambda_0/10$ and the cladding is (a) air (b) anisotropic non-magnetic dielectric ($\varepsilon_{\perp} = 1$ and $\varepsilon_z = 20$) (c) dual-anisotropic dielectric ($\varepsilon_{\perp} = \mu_{\perp} = 20$ and $\varepsilon_z = \mu_z = 20$). It is seen that the waveguide mode shifts to lower values of u (higher w) denoting faster decay in the cladding.

A.3 2D Extreme-skin-depth Waveguides

A.3.1 Dual-anisotropic cladding

Assume an infinitely long isotropic dielectric cylinder oriented in the z direction with relative permittivity and permeability of (ε_1, μ_1) surrounded by a dual-anisotropic uniaxial dielectric with optical axis parallel to the cylinder axis and relative permittivity and permeability of $(\varepsilon_{\rho 2} = \varepsilon_{\varphi 2} = \mu_{\rho 2} = \mu_{\varphi 2} = n_{\perp 2}, \varepsilon_{z 2} = \mu_{z 2} = n_{z 2})$.

The Helmholtz wave equation for longitudinal field components inside a uniaxial anisotropic magneto-dielectric is:

$$\begin{cases} \nabla_t^2 E_z + \left(k_0^2 \varepsilon_z \mu_\perp - \frac{\varepsilon_z}{\varepsilon_\perp} \beta^2 \right) E_z = 0 \\ \nabla_t^2 H_z + \left(k_0^2 \varepsilon_\perp \mu_z - \frac{\mu_z}{\mu_\perp} \beta^2 \right) H_z = 0 \end{cases} \quad (\text{A.9})$$

where ∇_t^2 is tangential component of Laplacian. The time-harmonic solutions of the above equations in cylindrical coordinate system for the core and cladding are

$$\begin{aligned} E_z &= \begin{cases} A J_n(k_{\rho 1} \rho) \cos(n\varphi) e^{i\beta z}, & |\rho| < a \\ B K_n(k_{\rho 2} \rho) \cos(n\varphi) e^{i\beta z}, & |\rho| > a \end{cases} \\ H_z &= \begin{cases} C J_n(k_{\rho 1} \rho) \sin(n\varphi) e^{i\beta z}, & |\rho| < a \\ D K_n(k_{\rho 2} \rho) \sin(n\varphi) e^{i\beta z}, & |\rho| > a \end{cases} \end{aligned} \quad (\text{A.10})$$

where A , B , C , and D are constants and defined from boundary conditions and excitations; J_n and K_n are n^{th} -order of the Bessel function of the first type and the modified Bessel function of the second type, respectively; β is the propagation constant, and $k_{\rho 1}$, $k_{\rho 2}$ are defined as

$$\begin{cases} \beta^2 + k_{\rho 1}^2 = k_0^2 \varepsilon_1 \mu_1 \\ \beta^2 - \left(\frac{k_{\rho 2}}{\gamma} \right)^2 = k_0^2 n_{\perp 2}^2, \quad \left(\gamma^2 = \frac{\varepsilon_{z2}}{\varepsilon_{\perp 2}} = \frac{\mu_{z2}}{\mu_{\perp 2}} = \frac{n_{z2}}{n_{\perp 2}} \right) \end{cases} \quad (\text{A.11})$$

The other field components are derived from the Maxwell's equations easily:

$$\begin{aligned}
E_r &= \frac{-1}{i\omega\varepsilon_0\varepsilon_\rho} \left(\frac{\partial H_z}{\rho\partial\varphi} - \frac{\partial H_\varphi}{\partial z} \right) = \frac{i}{(k_0^2\varepsilon_\rho\mu_\varphi - \beta^2)} \left(\beta \frac{\partial E_z}{\partial\rho} + \frac{\omega\mu_0\mu_\varphi}{\rho} \frac{\partial H_z}{\partial\varphi} \right) \\
&= \cos(n\varphi) e^{i\beta z} \times \begin{cases} \frac{i}{k_{\rho 1}^2} \left[A\beta k_{\rho 1} J_n(k_{\rho 1}\rho) + C \frac{\omega\mu_0\mu_{1n}}{\rho} J_n(k_{\rho 1}\rho) \right], & |\rho| < a \\ \frac{-i}{(k_{\rho 2}/\gamma)^2} \left[B\beta k_{\rho 2} K_n(k_{\rho 2}\rho) + D \frac{\omega\mu_0\mu_{\perp 2n}}{\rho} K_n(k_{\rho 2}\rho) \right], & |\rho| > a \end{cases} \\
E_\varphi &= \frac{-1}{i\omega\varepsilon_0\varepsilon_\varphi} \left(\frac{\partial H_\rho}{\partial z} - \frac{\partial H_z}{\partial r} \right) = \frac{i}{(k_0^2\varepsilon_\varphi\mu_r - \beta^2)} \left(\frac{\beta}{r} \frac{\partial E_z}{\partial\varphi} - \omega\mu_0\mu_\rho \frac{\partial H_z}{\partial\rho} \right) \\
&= \sin(n\varphi) e^{i\beta z} \times \begin{cases} \frac{-i}{k_{\rho 1}^2} \left[A \frac{\beta n}{r} J_n(k_{\rho 1}\rho) + C\omega\mu_0\mu_1 k_{\rho 1} J_n(k_{\rho 1}\rho) \right], & |\rho| < a \\ \frac{i}{(k_{\rho 2}/\gamma)^2} \left[B \frac{\beta n}{\rho} K_n(k_{\rho 2}\rho) + D\omega\mu_0\mu_{\perp 2} k_{\rho 2} K_n(k_{\rho 2}\rho) \right], & |\rho| > a \end{cases} \\
H_\rho &= \frac{1}{i\omega\mu_0\mu_\rho} \left(\frac{\partial E_z}{\rho\partial\varphi} - \frac{\partial E_\varphi}{\partial z} \right) = \frac{i}{(k_0^2\varepsilon_\varphi\mu_\rho - \beta^2)} \left(\beta \frac{\partial H_z}{\partial\rho} - \frac{\omega\varepsilon_0\varepsilon_\varphi}{r} \frac{\partial E_z}{\partial\varphi} \right) \\
&= \sin(n\varphi) e^{i\beta z} \times \begin{cases} \frac{i}{k_{\rho 1}^2} \left[A \frac{\omega\varepsilon_0\varepsilon_{1n}}{\rho} J_n(k_{\rho 1}\rho) + C\beta k_{\rho 1} J_n(k_{\rho 1}\rho) \right], & |\rho| < a \\ \frac{-i}{(k_{\rho 2}/\gamma)^2} \left[B \frac{\omega\varepsilon_0\varepsilon_{\perp 2n}}{r} K_n(k_{\rho 2}\rho) + D\beta k_{\rho 2} K_n(k_{\rho 2}\rho) \right], & |\rho| > a \end{cases} \\
H_\varphi &= \frac{1}{i\omega\mu_0\mu_\varphi} \left(\frac{\partial E_\rho}{\partial z} - \frac{\partial E_z}{\partial\rho} \right) = \frac{i}{(k_0^2\varepsilon_\rho\mu_\varphi - \beta^2)} \left(\frac{\beta}{\rho} \frac{\partial H_z}{\partial\varphi} + \omega\varepsilon_0\varepsilon_\rho \frac{\partial E_z}{\partial\rho} \right) \\
&= \cos(n\varphi) e^{i\beta z} \times \begin{cases} \frac{i}{k_{\rho 1}^2} \left[A\omega\varepsilon_0\varepsilon_1 k_{\rho 1} J_n(k_{\rho 1}\rho) + C \frac{\beta n}{\rho} J_n(k_{\rho 1}\rho) \right], & |\rho| < a \\ \frac{-i}{(k_{\rho 2}/\gamma)^2} \left[B\omega\varepsilon_0\varepsilon_{\perp 2} k_{\rho 2} K_n(k_{\rho 2}\rho) + D \frac{\beta n}{\rho} K_n(k_{\rho 2}\rho) \right], & |\rho| > a \end{cases}
\end{aligned} \tag{A.12}$$

By applying the boundary conditions and subtracting dispersion relations, two coupled equations are obtained:

$$\begin{cases} \frac{J'_n(u)}{uJ_n(u)} = - \left(\frac{\mu_{\perp 2}}{\mu_1} + \frac{\varepsilon_{\perp 2}}{\varepsilon_1} \right) \frac{\gamma^2 K'_n(w)}{2wK_n(w)} \pm \\ \left[\left(\frac{\mu_{\perp 2}}{\mu_1} - \frac{\varepsilon_{\perp 2}}{\varepsilon_1} \right)^2 \left(\frac{\gamma^2 K'_n(w)}{2wK_n(w)} \right)^2 + \frac{n^2\beta^2}{\varepsilon_1\mu_1 k_0^2} \left(\frac{1}{u^2} + \left(\frac{\gamma}{w} \right)^2 \right)^2 \right]^{\frac{1}{2}} \\ u^2 + \left(\frac{w}{\gamma} \right)^2 = (k_0 a)^2 (\varepsilon_1\mu_1 - \varepsilon_{\perp 2}\mu_{\perp 2}) \end{cases} \tag{A.13}$$

where $u = k_{\rho 1}a$ and $w = k_{\rho 2}a$. This set of equations can yield two independent solutions according to the sign of the second term in the first equation. For $n > 1$, the solutions are conventionally known as HE and EH modes for negative and positive signs respectively, for the conventional optical fibers. The first HE mode can propagate without any cut-off.

A.3.2 Non-magnetic anisotropic cladding

To verify that the transformed momentum of light can indeed lead to sub-diffraction confinement even without using dual anisotropic cladding, we solved Maxwell's equations in an arbitrary shaped glass core surrounded by all-dielectric nonmagnetic anisotropic metamaterials that transform momentum. Assume that the core and anisotropic cladding is nonmagnetic ($\mu_1 = \mu_2 = 1$) in (A.9). The longitudinal field components in the core and cladding are:

$$\begin{aligned} E_z &= \begin{cases} A J_n(k_{\rho 1} \rho) \cos(n\varphi) e^{i\beta z}, & |\rho| < a \\ B K_n(k_{\rho 2} \rho) \cos(n\varphi) e^{i\beta z}, & |\rho| > a \end{cases} \\ H_z &= \begin{cases} C J_n(k_{\rho 1} \rho) \sin(n\varphi) e^{i\beta z}, & |\rho| < a \\ D K_n\left(\frac{k_{\rho 2}}{\gamma} \rho\right) \sin(n\varphi) e^{i\beta z}, & |\rho| > a \end{cases} \end{aligned} \quad (\text{A.14})$$

where $k_{\rho 1}$, $k_{\rho 2}$ are defined as:

$$\begin{cases} \beta^2 + k_{\rho 1}^2 = k_0^2 \varepsilon_1 \\ \beta^2 - \left(\frac{k_{\rho 2}}{\gamma}\right)^2 = k_0^2 \varepsilon_{\perp 2}, \quad \left(\gamma^2 = \frac{\varepsilon_{z2}}{\varepsilon_{\perp 2}}\right) \end{cases} \quad (\text{A.15})$$

The other field components are derived in the same way:

$$\begin{aligned}
E_\rho &= \frac{-1}{i\omega\varepsilon_0\varepsilon_\rho} \left(\frac{\partial H_z}{\rho\partial\varphi} - \frac{\partial H_\varphi}{\partial z} \right) = \frac{i}{(k_0^2\varepsilon_\rho - \beta^2)} \left(\beta \frac{\partial E_z}{\partial\rho} + \frac{\omega\mu_0}{\rho} \frac{\partial H_z}{\partial\varphi} \right) \\
&= \cos(n\varphi) e^{i\beta z} \times \begin{cases} \frac{i}{k_{\rho 1}^2} \left[A\beta k_{\rho 1} J_n(k_{\rho 1}\rho) + C\frac{\omega\mu_0 n}{\rho} J_n(k_{\rho 1}\rho) \right], & |\rho| < a \\ \frac{-i}{(k_{\rho 2}/\gamma)^2} \left[B\beta k_{\rho 2} K_n(k_{\rho 2}\rho) + D\frac{\omega\mu_0 n}{\rho} K_n\left(\frac{k_{\rho 2}}{\gamma}\rho\right) \right], & |\rho| > a \end{cases} \\
E_\varphi &= \frac{-1}{i\omega\varepsilon_0\varepsilon_\varphi} \left(\frac{\partial H_\rho}{\partial z} - \frac{\partial H_z}{\partial\rho} \right) = \frac{i}{(k_0^2\varepsilon_\varphi - \beta^2)} \left(\frac{\beta}{\rho} \frac{\partial E_z}{\partial\varphi} - \omega\mu_0 \frac{\partial H_z}{\partial\rho} \right) \\
&= \sin(n\varphi) e^{i\beta z} \times \begin{cases} \frac{-i}{k_{\rho 1}^2} \left[A\frac{\beta n}{\rho} J_n(k_{\rho 1}\rho) + C\omega\mu_0 k_{\rho 1} J_n(k_{\rho 1}\rho) \right], & |\rho| < a \\ \frac{i}{(k_{\rho 2}/\gamma)^2} \left[B\frac{\beta n}{\rho} K_n(k_{\rho 2}\rho) + D\omega\mu_0 \frac{k_{\rho 2}}{\gamma} K_n\left(\frac{k_{\rho 2}}{\gamma}\rho\right) \right], & |\rho| > a \end{cases} \\
H_\rho &= \frac{1}{i\omega\mu_0} \left(\frac{\partial E_z}{\rho\partial\varphi} - \frac{\partial E_\varphi}{\partial z} \right) = \frac{i}{(k_0^2\varepsilon_\varphi - \beta^2)} \left(\beta \frac{\partial H_z}{\partial\rho} - \frac{\omega\varepsilon_0\varepsilon_\varphi}{\rho} \frac{\partial E_z}{\partial\varphi} \right) \\
&= \sin(n\varphi) e^{i\beta z} \times \begin{cases} \frac{i}{k_{\rho 1}^2} \left[A\frac{\omega\varepsilon_0\varepsilon_{1n}}{r} J_n(k_{\rho 1}\rho) + C\beta k_{\rho 1} J_n(k_{\rho 1}\rho) \right], & |\rho| < a \\ \frac{-i}{(k_{\rho 2}/\gamma)^2} \left[B\frac{\omega\varepsilon_0\varepsilon_{\perp 2n}}{\rho} K_n(k_{\rho 2}\rho) + D\beta \frac{k_{\rho 2}}{\gamma} K_n\left(\frac{k_{\rho 2}}{\gamma}\rho\right) \right], & |\rho| > a \end{cases} \\
H_\varphi &= \frac{1}{i\omega\mu_0} \left(\frac{\partial E_\rho}{\partial z} - \frac{\partial E_z}{\partial\rho} \right) = \frac{i}{(k_0^2\varepsilon_\rho - \beta^2)} \left(\frac{\beta}{\rho} \frac{\partial H_z}{\partial\varphi} + \omega\varepsilon_0\varepsilon_\rho \frac{\partial E_z}{\partial\rho} \right) \\
&= \cos(n\varphi) e^{i\beta z} \times \begin{cases} \frac{i}{k_{\rho 1}^2} \left[A\omega\varepsilon_0\varepsilon_{1n} k_{\rho 1} J_n(k_{\rho 1}\rho) + C\frac{\beta n}{r} J_n(k_{\rho 1}\rho) \right], & |\rho| < a \\ \frac{-i}{(k_{\rho 2}/\gamma)^2} \left[B\omega\varepsilon_0\varepsilon_{\perp 2n} k_{\rho 2} K_n(k_{\rho 2}\rho) + D\frac{\beta n}{\rho} K_n\left(\frac{k_{\rho 2}}{\gamma}\rho\right) \right], & |\rho| > a \end{cases}
\end{aligned} \tag{A.16}$$

Similar to the dual-anisotropic case, by applying the boundary conditions, two coupled equations are obtained:

$$\left\{ \begin{aligned} \frac{J'_n(u)}{uJ_n(u)} &= - \left(\frac{\gamma K'_n\left(\frac{w}{\gamma}\right)}{2wK_n\left(\frac{w}{\gamma}\right)} + \frac{\varepsilon_{\perp 2}\gamma^2 K'_n(w)}{2\varepsilon_{1n}wK_n(w)} \right) \pm \\ &\left[\left(\frac{\gamma K'_n\left(\frac{w}{\gamma}\right)}{2wK_n\left(\frac{w}{\gamma}\right)} - \frac{\varepsilon_{\perp 2}\gamma^2 K'_n(w)}{2\varepsilon_{1n}wK_n(w)} \right)^2 + \frac{n^2\beta^2}{\varepsilon_{1n}k_0^2} \left(\frac{1}{u^2} + \left(\frac{\gamma}{w}\right)^2 \right)^2 \right]^{\frac{1}{2}} \\ u^2 + \left(\frac{w}{\gamma}\right)^2 &= (k_0a)^2 (\varepsilon_{1n} - \varepsilon_{\perp 2}) \end{aligned} \right. \tag{A.17}$$

Fig. A.4 displays the graphical solution of the equation (A.13) and (A.17) for a cylindrical glass core with radius of $\lambda_0/10$ for air, non-magnetic anisotropic, and dual anisotropic claddings. The plots show the right and left side of the first equation in (A.13) and (A.17) versus u when w is replaced from the second equation in (A.13)

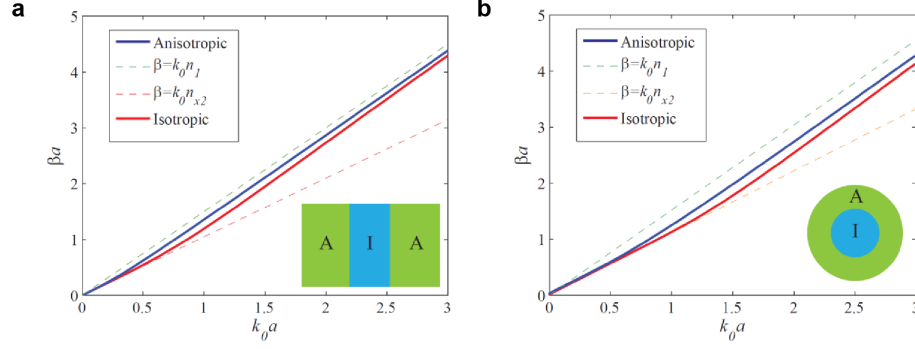


Fig. A.5. The propagation constant of (a) 1D and (b) 2D nonmagnetic extreme-skin-depth (e-skid) waveguides in comparison with a conventional slab waveguide and an optical fiber with cladding permittivity of $\varepsilon = 1.1$. The core core size/ radius is $\lambda_0/10$; $\varepsilon_x = 1.1$ ($\varepsilon_{\perp} = 1.1$) and $\varepsilon_z = 20$. The light line in the core and the cladding is also plotted, which shows the wave propagates inside the core due to the total internal reflection and decays away outside the core. The propagation constant in anisotropic case is larger since the power confinement is more.

and (A.17). The asymptote (shown by the dashed line) is the maximum value for the u where w becomes zero (which means that although the mode propagates without cut-off, the wave does not decay in the cladding and its size must be infinite). It can be seen that anisotropic cladding shifts the intersection to the lower values for u (higher w) without changing the asymptote position, so, anisotropic cladding leads to the faster decaying and consequently more confinement.

The propagation constant dispersion for both 1D and 2D extreme-skin-depth (e-skid) waveguides are displayed in Fig. A.5. Propagation constant is always between the light lines in the core and the cladding. It guaranties that the guided mode bounces off by total internal reflection inside the core and decays away in the cladding. At low frequencies the propagation constant is close to the light line in the cladding. This means that the mode is poorly confined inside the core, but as the frequency increases, more power is confined inside the core and the propagation constant asymptotically meets the light line inside the core. Since the power confinement is better

for extreme-skin-depth (e-skid) waveguides in comparison with conventional dielectric waveguides, the propagation constant is larger in the entire spectrum.

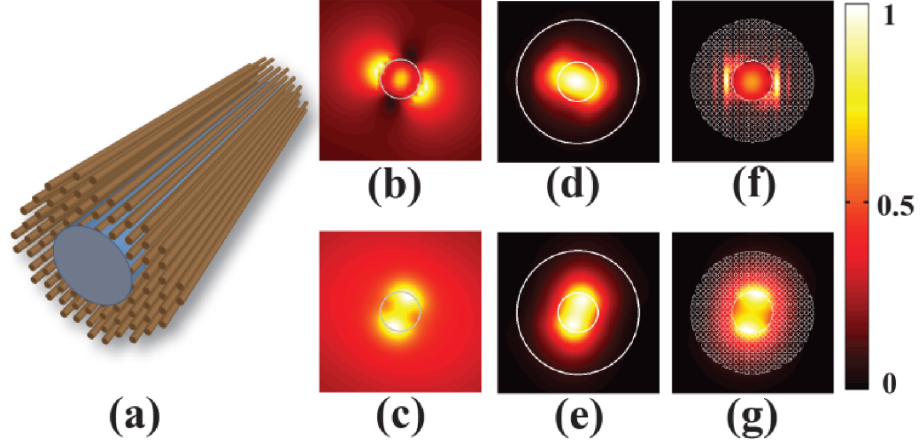


Fig. A.6. (a) Schematic representation of a practical extreme-skin-depth (e-skid) metamaterial fiber at optical telecommunication wavelength ($\lambda = 1550 \text{ nm}$). The metamaterial cladding consisting of germanium nanorods embedded in porous silica surrounding a silicon rod core. (b-g) Normalized simulated distribution of the electric (top plots) and magnetic (bottom plots) energy density of the waveguide when the core diameter is 0.15λ and germanium fill fraction is 62.5%. (b) & (c) Electric and magnetic energy density of the bare waveguide. The fraction of power inside the core to the total power (η) is 3% and the mode area is $43(\lambda/2n_{core})^2$. (d) & (e) Electric and magnetic energy density of the waveguide with anisotropic cladding ($\epsilon_x = \epsilon_y = 3.7$ and $\epsilon_z = 11.8$). In the homogenized limit, the calculated η , mode area, and effective index are 35%, $1.85(\lambda/2n_{core})^2$, and 2.13, respectively. (f) & (g) Electric and magnetic energy density of the practical waveguide surrounded by nanowires which achieves the required anisotropy. According to effective theory, it achieves the effective permittivity of the cladding of part D & E. The simulated results of η , mode area, and effective index are 40%, $1.61(\lambda/2n_{core})^2$, and 2.09, respectively in agreement with the effective medium calculations. Significantly better performance can be achieved by using higher index rods in the nanowire design.

A.4 Metamaterial fiber

We present a practical metamaterial fiber that utilizes extreme-skin-depth (e-skid) waveguides for enhanced confinement at the telecommunication wavelength (1550 nm). We consider a cylindrical core of silicon ($n = 3.47$) with a diameter of 0.15λ and the cladding is composed of germanium ($n = 4.3$) nanowires surrounded by ultra-low index porous silica ($n = 1.05$). The cladding size is three-times bigger than the core (Fig. A.6). The germanium nanowire axis is parallel to the fiber axis and their periodicity as well as diameter is much smaller than the wavelength ($\Lambda = 20$ nm, $D = 18$ nm). Maxwell-Garnett method can be used to approximate the effective permittivity of the cladding. For the germanium filling fraction of $\rho = 0.625$, we can obtain strong anisotropy ($\varepsilon_x = \varepsilon_y = 3.7$ and $\varepsilon_z = 11.8$). It is important to note that the dielectric constant along the propagation direction is large however the transverse dielectric constant is lesser than silicon preserving total internal reflection. A detailed theory of how the fundamental HE_{11} mode of any cylindrical structure is affected by the momentum transformation is presented in the supplementary information.

Fig A.6b & c show the simulation results of the electric and magnetic energy density, respectively, for the bare waveguide. Only 3% of the total power is inside the core and the mode area is $43A_0$. Fig. A.6d & e show the results when the anisotropic cladding is added. In these plots, we consider a homogenous effective medium cladding. In this case, the fraction of power inside the core to the total power (η) increases to 35% and the mode area decreases to $1.85A_0$. The results for the practical nanorod realization ($\Lambda = 20$ nm, $D = 18$ nm) are plotted in Fig. A.6e & g. In this case, $\eta = 40\%$ and the mode area is $1.61A_0$, which is in excellent agreement with the homogenized case.

We note that the nanowire design does not attain deeply subwavelength performance at 1.55 micron wavelength due to limitations in available high index media for the extreme-skin-depth (e-skid). However, we note the excellent agreement between

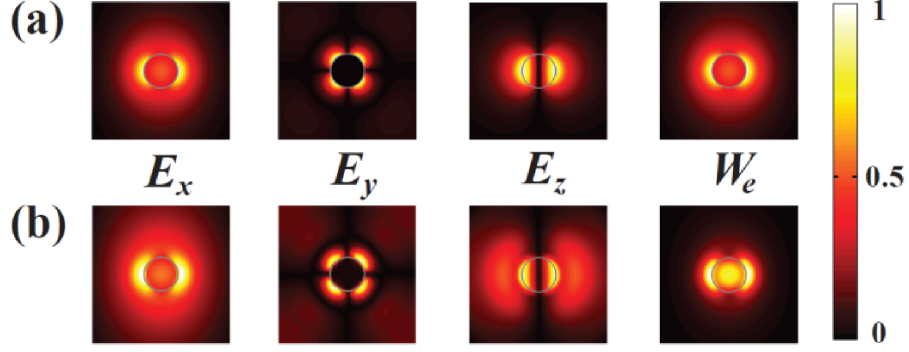


Fig. A.7. Electric field and energy density distribution of a extreme-skin-depth (e-skid) waveguide composed a cylindrical silicon core with a diameter of $0.15\lambda_0$ covered by a nonmagnetic anisotropic cladding ($\varepsilon_{\perp 2}=3.7$ and $\varepsilon_z=11.8$). (a) Analytical calculation. (b) Numerical calculation. The analytical calculation of η , mode area, and effective index are 34.6%, $1.94 (\lambda/2n_{core})^2$, and 2.126, respectively. The simulated results are 26%, $2.58 (\lambda/2n_{core})^2$, and 2.15, respectively. The slight deviations between analytical and simulated results arise due to a finite sized simulation domain.

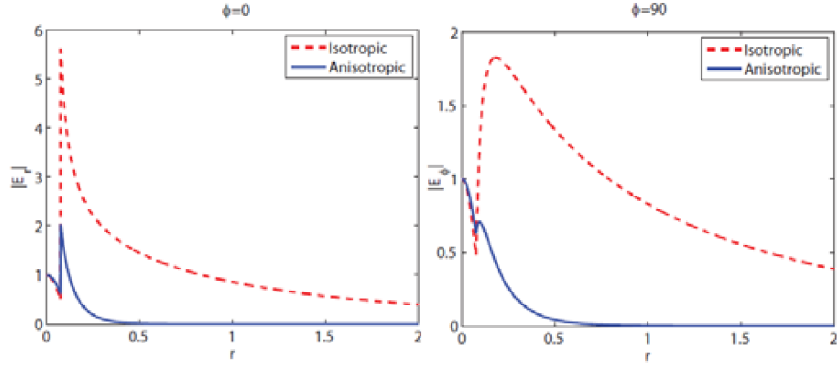


Fig. A.8. Normalized electric field distribution of the waveguide in Fig. A.7 in comparison with the case without cladding. The cladding causes fields to decay fast outside in the cladding signifying the transformation of optical momentum.

the effective medium theory of 2D anisotropic claddings and the practical nanowire design. Therefore the cross-talk reduction over conventional designs presented in the earlier sections will hold true for the 2D design as well. We emphasize that at lower

frequencies readily available high index media [2] can lead to deep subwavelength performance using both 1D multilayer and 2D nanowire designs. Comparison between analytical calculations explained above and the simulation results shown in Fig. A.7. There is a good agreement between the exact solution and numerical calculations. Fig. A.8 shows the effect of anisotropic cladding on decaying of evanescent waves in the cladding for the structure in Fig. A.7.

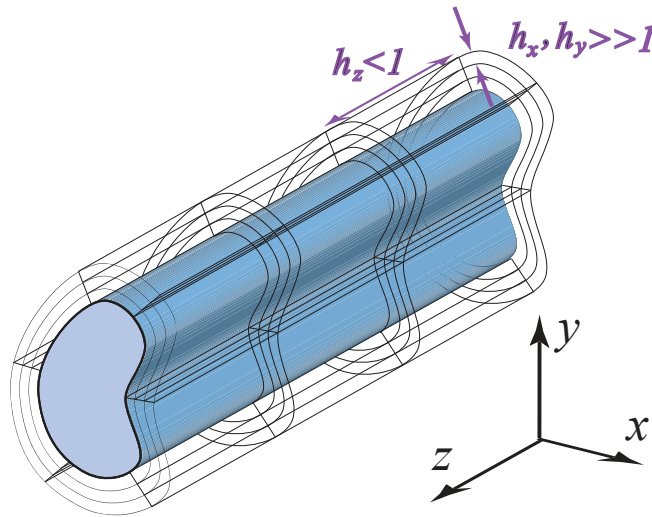


Fig. A.9. **Light confinement inside a low-index 2D dielectric waveguide using metamaterial claddings.** Confining a guided wave inside a transparent low index dielectric with arbitrary cross section. The momentum transforming cladding surrounding the core leads to simultaneous total internal reflection and rapid decay of evanescent waves outside the core.

A.5 Quasi-TEM waveguide

We now apply the momentum transformation to surround an infinitely long glass rod with arbitrarily shaped cross section ($A \ll \lambda^2$). The electromagnetic grid has a finite width and ideally needs to achieve $h_x, h_y \gg 1$ and $h_z < n_{core}$ to allow for the lowest-order mode (HE_{11}) to travel inside the glass core and bounce off by total internal reflection but simultaneously decay away rapidly causing sub-diffraction

confinement of the mode (Fig. A.9). This transformation also causes the longitudinal components of fields, in comparison to the transverse ones, to go zero. Indeed, the electric and magnetic fields for the transformed waveguide can be related to the untransformed ones as

$$\begin{aligned}\frac{E_{x'}}{E_{z'}} &= \frac{h_x}{h_z} \frac{E_x}{E_z} = \gamma \frac{E_x}{E_z} \\ \frac{H_{x'}}{H_{z'}} &= \frac{h_x}{h_z} \frac{H_x}{H_z} = \gamma \frac{H_x}{H_z}\end{aligned}\tag{A.18}$$

and due to the large confinement factor (γ), the longitudinal field components become negligible. Thus the transformed propagating mode is a quasi-TEM mode, and in contrast to conventional waveguides at low-frequencies, it does not need two reflectors or perfect conductor at boundaries. Figs. A.10a and A.10b shows the simulation results of magnetic and electric field vectors, respectively, for a sub-diffraction arbitrarily shaped glass waveguide with average radius of 0.1λ covered by a transformed cladding ($h_x = h_y = 5$ and $h_z = 1.2$). The simulations have been done by Finite Integration Technique (FIT) commercial software CST Microwave Studio [152]. Note that we have used the relaxed condition of $h_z = 1.2$ since the inner medium is glass not air. It can be seen that fields are concentrated in the low-index sub-diffraction dielectric. Furthermore, these fields are almost transverse to the propagation direction which is evident from the vector directions in Fig. A.10.

The class of artificial media that lead to these momentum transformations will have $\varepsilon_x, \varepsilon_y < \varepsilon_{glass}$ and $\mu_x, \mu_y < \mu_{glass}$ while $\mu_z, \varepsilon_z \gg 1$. Note that we also have $\varepsilon_x = \mu_x, \varepsilon_y = \mu_y$ and $\varepsilon_z = \mu_z$ thus allowing single mode propagation inspite of the anisotropy. We term this class of artificial media as dual anisotropic giant birefringent metamaterials. If the waveguide cross-section is circular, the dispersion follows (A.13). Although momentum transformations, unlike conventional TO applications, can be fulfilled by homogenous materials, the cladding must be dual-anisotropic which is very difficult to implement at optical frequencies. However, general dual-anisotropic structures can be implemented at terahertz or microwave frequencies [83]. With a nonmagnetic cladding, we can only transform the electric field momentum in the

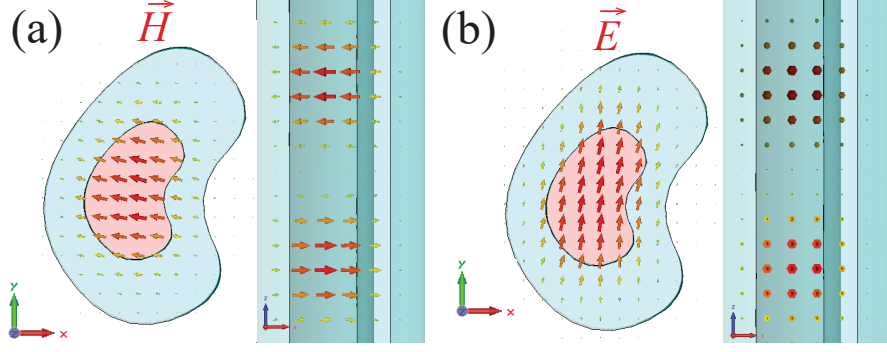


Fig. A.10. **Light confinement inside a low-index 2D dielectric waveguide using metamaterial claddings.** Confining a guided wave inside a transparent low index dielectric with arbitrary cross section. The momentum transforming cladding surrounding the core leads to simultaneous total internal reflection and rapid decay of evanescent waves outside the core.

cladding. However, even this reduced implementation can control the skin depth in the cladding and confine energy inside the core. As we display in the next section, one set of non-magnetic media which can cause the momentum transformation are anisotropic homogenous dielectric materials with $\varepsilon_x = \varepsilon_y < \varepsilon_{core}$ and $\varepsilon_z \gg 1$. The dispersion relation for circular waveguide with non-magnetic anisotropic claddings can be found from (A.17).

A.6 Figures of merit

A.6.1 Mode length/area

To confirm the sub-diffraction nature of waveguide we calculated the mode area for waveguides, a common figure of merit for sub-diffraction devices [51]:

$$A_m = \frac{W_m}{\max\{W(r)\}} = \frac{1}{\max\{W(r)\}} \int_{-\infty}^{\infty} W(r) d^2r \quad (\text{A.19})$$

where W_m and $W(r)$ are electromagnetic energy and energy density, respectively, and the integration is calculated on the surface normal to the propagation direction. In Fig. A.11 and A.12a we compare the mode length/area of the 1D and 2D

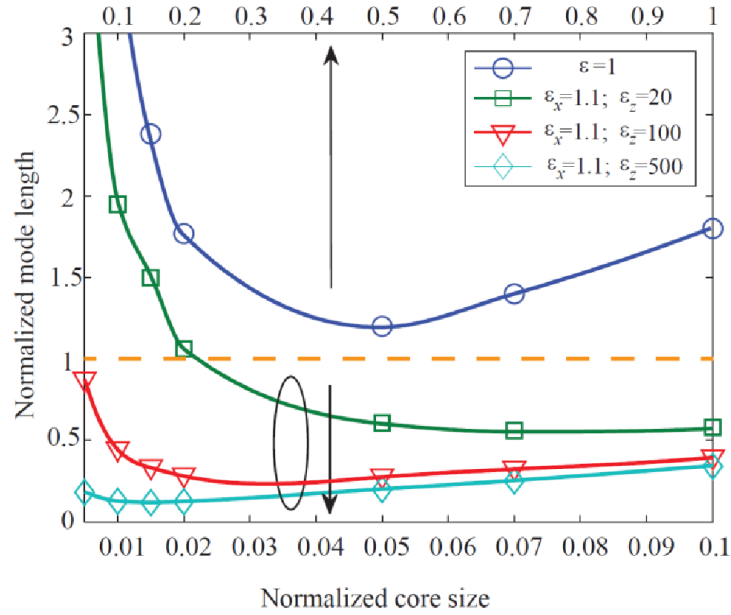


Fig. A.11. Deep sub-diffraction performance: Irrespective of core size made of glass, one can always achieve sub-diffraction mode lengths with access to higher index media. This is difficult at optical frequencies but can be achieved by anisotropic metamaterials at THz and microwave frequencies.

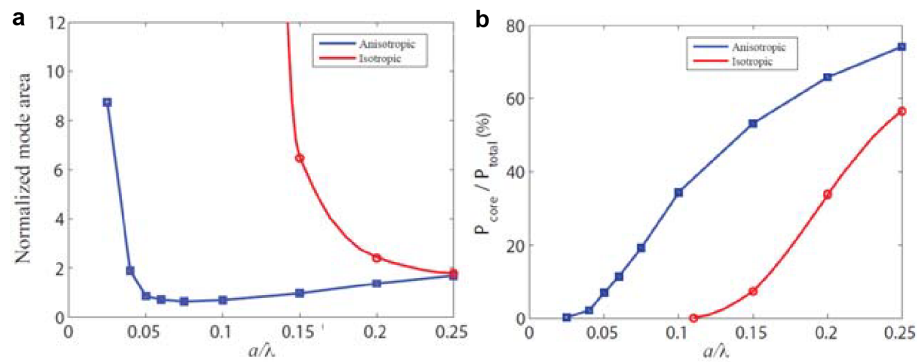


Fig. A.12. Comparison of (a) normalized mode area and (b) power inside the core fraction for the glass 2D waveguide with and without cladding versus core radius. The cladding permittivity in tangential and longitudinal direction is 1 and 20, respectively. It is seen that the metamaterial cladding decreases the mode area and also causes the power in the core to increase.

extreme-skin-depth (e-skid) waveguides with conventional waveguides. The mode size reduction using anisotropic cladding is clearly evident.

A.6.2 Power in the core

Note that the above definition of mode area essentially elucidates the peak power carried for a given input power in the waveguide. However, due to the inhomogeneous profile of the fields it becomes imperative to define the power carried within this mode area. For example, in the case of slot waveguides the evanescent tail carries a significant fraction of the power though the peak power in the slot is quite high. In Fig. A.12b, we have evaluated both the mode area and power in the core for e-skid waveguides.

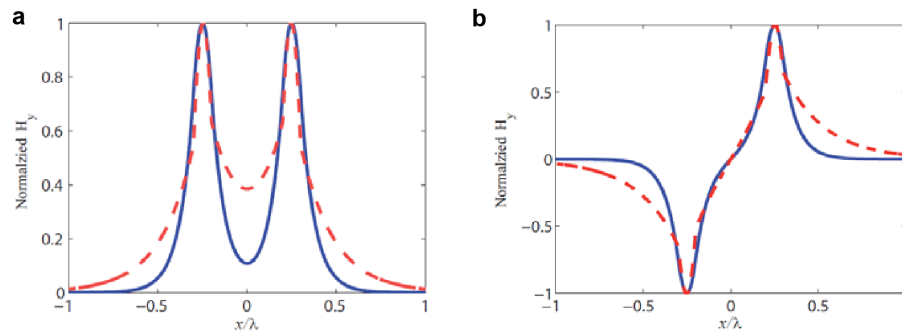


Fig. A.13. The normalized magnetic field amplitude of the first (a) even (b) odd TM mode of coupled silicon slab waveguides with the slab size of 0.1λ and center-to-center separation of 0.5λ for silica (dashed red lines) and germanium-silica multilayer (solid blue lines) cladding with effective permittivity of $\varepsilon_x=4.8$ and $\varepsilon_z=11.9$.

A.6.3 Cross-talk

For dielectric waveguides it also becomes necessary to evaluate the cross talk once the size of the core decreases. This is important for understanding the potential for

dense photonic integration. The major advantage of practical e-skid waveguide is the reduced cross talk.

Magnetic field of even and odd TM mode for a pair of coupled dielectric slab waveguides with size of $2a$ and separation of s surrounded by an anisotropic dielectric can be written as:

$$\begin{aligned}
 H_y^e &= \begin{cases} A^e \cosh(k_{x2}^e x) e^{i\beta^e z} & |x| \leq s \\ [B^e \cos(k_{x1}^e x) + C^e \sin(k_{x1}^e x)] e^{i\beta^e z} & s < |x| \leq s + 2a \\ D^e e^{-k_{x2}^e z} e^{i\beta^e z} & s + 2a < |x| \end{cases} \\
 H_y^o &= \begin{cases} A^o \sinh(k_{x2}^o x) e^{i\beta^o z} & |x| \leq s \\ [B^o \cos(k_{x1}^o x) + C^o \sin(k_{x1}^o x)] e^{i\beta^o z} & s < |x| \leq s + 2a \\ D^o e^{-k_{x2}^o z} e^{i\beta^o z} & s + 2a < |x| \end{cases} \quad (\text{A.20})
 \end{aligned}$$

where momentums are defined similar to the single dielectric slab waveguide case shown in (A.7). By matching boundary conditions and using dispersion relations, propagation constant for the even and odd modes can be calculated. We also analytically calculated propagation constant of the even and odd mode of coupled slab waveguides for half space and using symmetric and antisymmetric boundary conditions, respectively.

Fig. A.13 compares the normalized magnetic field of the even and odd mode of two coupled silicon slab waveguides with a size of $\lambda/10$ and the separation of $\lambda/2$ when the cladding is air (dashed lines) and when it is anisotropic (solid lines). In this case, the anisotropic dielectric permittivity is derived from effective medium theory (EMT) for silica-germanium multilayer at optical telecommunication wavelength (1550 nm) when the germanium fill fraction is 0.6. The EMT formulations for multilayers and nanorods are presented in the next section. The calculated propagation constant for the even and odd mode is $1.73k_0$ and $1.64k_0$, so the coupling length ($L_c \equiv \pi/|\beta^e - \beta^o|$) for silica cladding is less than 0.6λ , but when the waveguides are covered by the anisotropic cladding, the propagation constant of the two modes become closer ($\beta^e = 2.5490k_0$, $\beta^o = 2.5448k_0$) and the coupling length increases dramatically and becomes 119λ .

For the practical multilayer cladding, $\beta^e = 2.5646k_0$ and $\beta^o = 2.5605k_0$ ascertained through full wave numerical simulations shown in Fig. A.13.

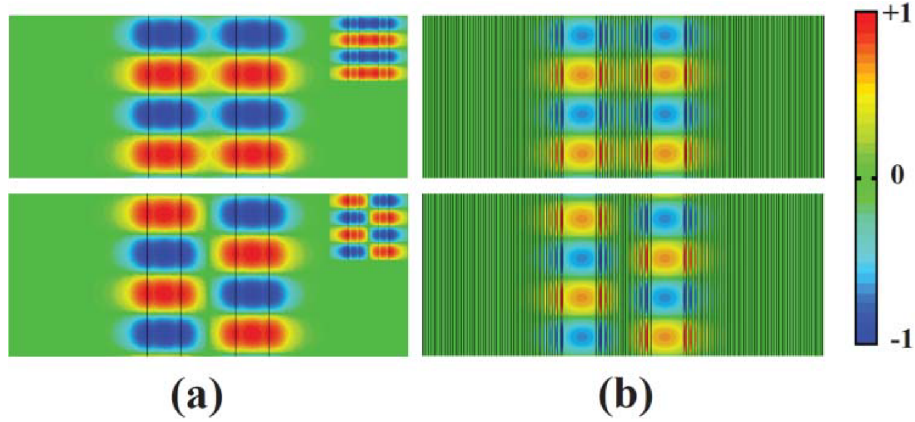


Fig. A.14. (a) Simulation results of the tangential electric field for even (up) and odd (bottom) modes of the coupled silicon waveguides. The core size is 0.1λ and center-to-center separation of 0.5λ . The required anisotropic all-dielectric response can be obtained using a germanium/silica multilayer with germanium fill fraction of 0.6. The inset shows the fields when the cladding is bulk silica. Note that the fields at the midpoint of the waveguide is significantly decreased with the TCW, a necessary condition for low cross talk. The coupling length of the structure with silica cladding is only 6λ , but it becomes more than 132λ with the metamaterial cladding. The power fraction inside the core also increases from 25% to 45%. (b) The simulation results of symmetric (up) and antisymmetric (bottom) modes for the practical structure with germanium/silica multilayer cladding and a unit cell size of 40 nm. The fields show good correspondence with the effective medium approximation and the coupling length is 119λ .

In fact, for large coupling length, the propagation constant and consequently fields amplitude of the even and odd modes should be very close. Note that the magnetic field for odd mode is zero at the center. The coupling length increases if the wave decays fast outside the cores and become negligible at the center for the even mode. As we can see in Fig. A.13 and A.14, the momentum transformation helps to reduce field amplitude at the center and decrease crosstalk.

We have also simulated the coupling length versus the cladding size shown in Fig. A.15. It is seen that the performance approaches the ideal infinite cladding for sizes approximately 3 times the core. The effect of core index on power confinement and crosstalk is displayed in Fig. A.16. As the core index increases, the effect of the anisotropic cladding on power confinement is modest but the cross talk in extreme-skin-depth (e-skid) waveguides is almost two orders of magnitude less than that in conventional waveguides.

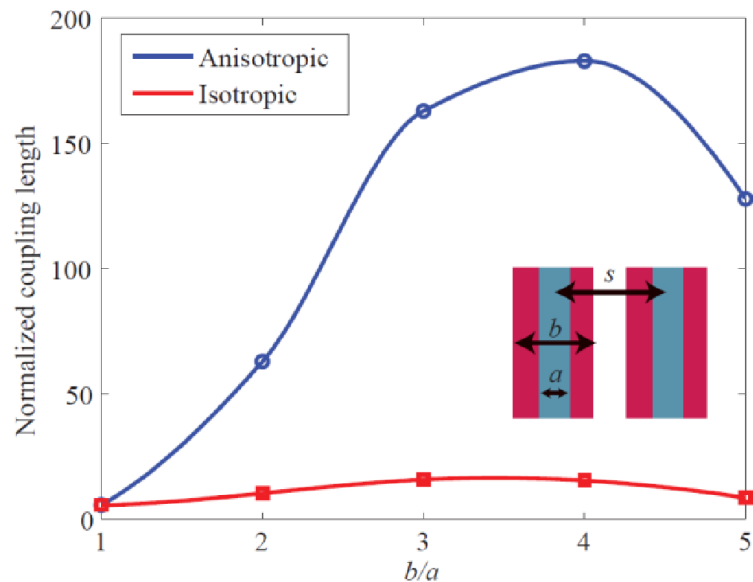


Fig. A.15. Normalized coupling length versus the cladding size. The core is silicon ($n = 3.47$) with a size of 0.1λ and center to center separation of 0.5λ . When the cladding is anisotropic ($\epsilon_x = 4.8$ and $\epsilon_z = 11.9$) the coupling length is much larger than that when the cladding is isotropic ($\epsilon = 4.8$). The waveguides are surrounded by glass.

A.7 Practical realization 1D and 2D

We discuss how to practically achieve these momentum transformations. Firstly, we argue that no naturally occurring medium has a strong anisotropy and the the maximum contrast between permittivity tensor elements is low for natural dielectrics

(e.g. TiO_2) as well as artificial polymers. Thus we cannot use natural dielectrics to preserve total internal reflection with a glass or silicon waveguide core interface while simultaneously increasing the momentum of evanescent waves. However, we can realize this extreme anisotropy by artificially structured media using available lossless dielectrics.

One practical way for realization of extreme anisotropic metamaterials is embedding periodic thin high index nanorods in a low index host dielectric such that the periodicity is much lower than the operating wavelength to ensure that the structure behaves as a homogenous material and it is far away from its band-gap. Effective relative permittivity normal (ε_{\perp}) and parallel (ε_{\parallel}) to nanorods axis for subwavelength conditions is independent to the periodicity and is calculated using Maxwell-Garnett approximation as [137]:

$$\begin{aligned}\varepsilon_{\parallel} &= \rho\varepsilon_d + (1 - \rho)\varepsilon_h \\ \varepsilon_{\perp} &= \frac{(1 + \rho)\varepsilon_d\varepsilon_h + (1 - \rho)\varepsilon_h^2}{(1 - \rho)\varepsilon_d + (1 + \rho)\varepsilon_h}\end{aligned}\tag{A.21}$$

where ε_d and ε_h are permittivity of the dielectric nanorods and host, respectively, and ρ is the fill-fraction of a nanorods in its unit-cell. According to (A.21), thin high index nanorods in a low-index host behave effectively as extreme anisotropic material to transform the desired momentum transformation in the cladding of the proposed cylindrical waveguides.

Another structure for realization of extreme anisotropic metamaterials is multi-layer combination of a high index and low index dielectric. In this case, effective relative permittivity normal and parallel to the layers are calculated as:

$$\begin{aligned}\varepsilon_{\parallel} &= \rho\varepsilon_d + (1 - \rho)\varepsilon_h \\ \varepsilon_{\perp} &= \frac{\varepsilon_d\varepsilon_h}{(1 - \rho)\varepsilon_d + \rho\varepsilon_h}\end{aligned}\tag{A.22}$$

This structure can be used for the momentum transformation in single and coupled slab waveguides as well as silicon strip waveguides.

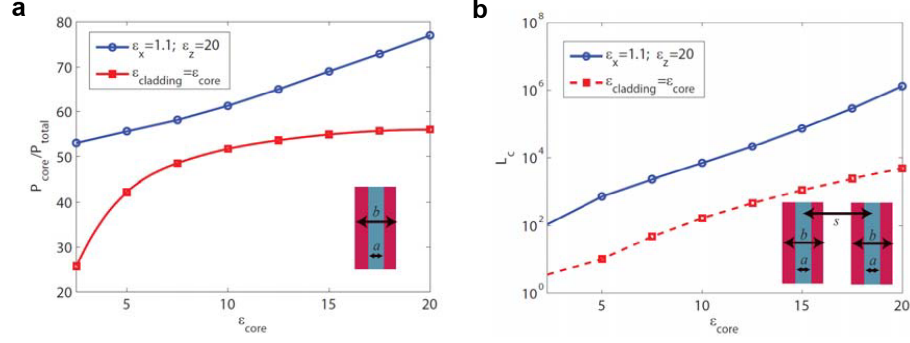


Fig. A.16. Role of core index, core size, cladding anisotropy and cladding size. (a) Comparing power confinement in the slab waveguide with anisotropic cladding ($\epsilon_x = 1.1$ and $\epsilon_z = 20$) as opposed to isotropic cladding. The core size is $a=0.1\lambda$ and the cladding size is three-times bigger than the core. It is seen that the power confinement in the core can be larger for the TCW even for high index cores. (b) Coupling length in the slab waveguide with anisotropic cladding ($\epsilon_x = 1.1$ and $\epsilon_z = 20$) is two orders of magnitude larger when compared to the isotropic cladding. The center-to-center separation of the coupled waveguides is $s = 0.5\lambda$. The cladding size is three-times bigger than the core surrounded by air. The core size is $a = 0.1\lambda$.

A.8 Comparison of different waveguide classes

The main figures of merit for a nano-waveguide is the length of propagation, confinement (mode area), power in the waveguide core (or within the mode area) and cross-talk between waveguides to assess the possibility of dense integration. Now we compare these figures of merit for the most well-known optical waveguides.

A.8.1 Optical fibers

It is almost loss-less and is appropriate for long distances communications, but it is diffraction-limited so energy cannot be confined for sub-diffraction sizes. Moreover, the wave decays slowly inside the cladding thus it is not suitable for photonic integration.

A.8.2 Photonic crystal fibers

It works based on Bragg reflection not total internal reflection. Thus the power does not scatter at bends and power can be confined inside a low index core. However, when the core size and period numbers becomes very small, power leaks outside so photonic integration density and power confinement is limited [34].

A.8.3 Plasmonic waveguides

Metals, in contrast to dielectrics, can confine energy below diffraction limit of light, but metals are too lossy at optical frequencies and even very low-loss metallic waveguides [51] cannot propagate light more than several wavelengths.

A.8.4 Slot waveguides

In this type of dielectric waveguides [53], light can be confined in a low-index sub-diffraction slot surrounded by a high-index dielectric. This kind of waveguide is suitable for nonlinear applications because of its small mode area, but since only a small fraction of power is inside the core (in comparison with optical fibers with similar integrated density) cross-talk for slot-waveguides is higher [56], so they are not suitable for confined photonic circuits.

A.8.5 Extreme-skin-depth waveguides

On the other hand, by transforming the space around a low-index dielectric, it is possible to confine energy inside a sub-diffraction core. Since both peak of energy density inside the core and decaying in cladding increases, photonic integration density increases and it is also suitable for nonlinear processes.

A.9 Method

We have used CST Microwave Studio [152], full-wave commercial software based on a finite integration technique (FIT), to obtain simulation results for the coupled slab waveguides reported in Chapter 2, for the waveguides with arbitrary cross section, and for the metamaterial fibers in Appendix A. Hexahedral meshes with 40 lines per wavelength with lower mesh limit of 10 have been assigned. The simulation area in transverse plane has been $2\lambda \times 2\lambda$ for the waveguides with anisotropic cladding and $10\lambda \times 10\lambda$ for the bare waveguides. The mode area and power ratio have been estimated based on the template-based post-processing 2D integral calculations. The simulation domain for calculation of cross-talk in y direction is only $\lambda/40$, terminated to magnetic boundary conditions to model infinite width for the slab waveguides. The open boundaries in x directions have been assigned one λ away from slab waveguides. The propagation constants have been derived from port information 1D results, and are in good agreement with analytical calculations. The simulations were made to converge with a maximum residual energy inside the calculation domain of 10^{-6} and 10^{-4} for time domain and frequency domain simulations, respectively.

B. ADDITIONAL RESULTS FOR ON-CHIP EXTREME SKIN-DEPTH WAVEGUIDES

B.1 Relaxed total internal reflection

Figure B.1 displays the field profile for p-polarized plane-wave propagation through an Si/SiO₂ multilayer sandwiched between two Si half spaces. The incident angle is $\theta = 10^\circ$ (top) and $\theta = 80^\circ$ (bottom). In both cases, $\Lambda = 100$ nm and $\rho = 0.5$, and light is incident from the left side at $\lambda = 1550$ nm. The gray and yellow regions represent Si and SiO₂ layers, respectively. The critical angle of the effective medium is $\theta_c = 32.33^\circ$ based on relaxed-TIR theory. It is seen that above the critical angle, the electromagnetic wave is totally reflected back to the left side and forms a standing wave on the left side but decays inside the multilayer and negligible power is transmitted to the right half space. However, when the incident angle is below the critical angle, most of the power is transmitted through the multilayer because the total thickness of the slab is thin in comparison with the wavelength.

B.2 Effect of periodicity and disorder on e-skin waveguides

Although practical metamaterial structures for realization of strong effective anisotropy are usually periodic, the effective macroscopic electromagnetic response of metamaterials does not stem from the periodicity (or unit-cell size). As long as the periodicity of the metamaterial building blocks is deeply subwavelength, the change in the periodicity does not change the electromagnetic response of metamaterials. Indeed, according to the effective medium theory (EMT), which has been explained in the main text, the effective constitutive parameters of multilayer metamaterials depend

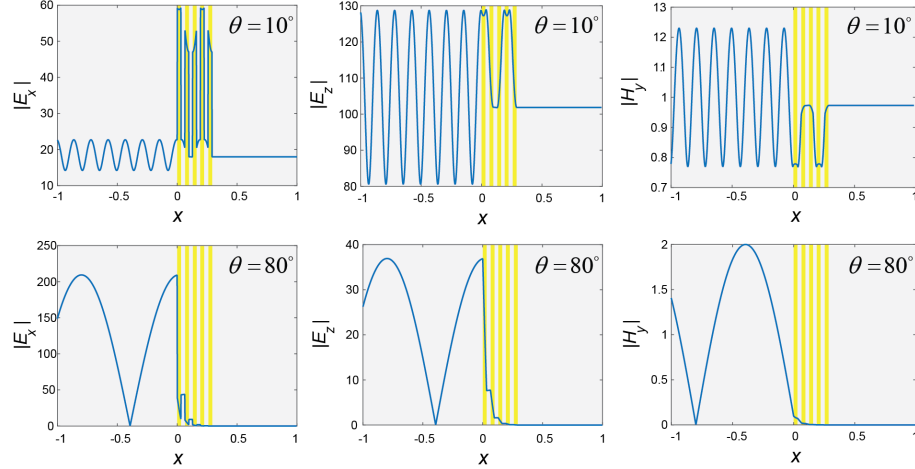


Fig. B.1. Comparison of the field profile for the p-polarized electromagnetic wave propagation through an Si/SiO₂ multilayer anisotropic metamaterial below (top) and above (bottom) the critical angle ($\theta_c = 32.33^\circ$). For both cases, $\Lambda = 100$ nm and $\rho = 0.5$. It is seen that incident light is totally reflected although the total thickness of the metamaterial layer ($t = 500$ nm) is subwavelength ($\lambda = 1550$ nm).

on the permittivity of the building blocks and their filling fraction, not the periodicity of the multilayer.

To demonstrate the effect of periodicity on the performance of e-skid waveguides, we analyzed 1D e-skid waveguides with multilayer claddings of the same total size, but different periodicities as illustrated in Fig. B.2. We also analyzed a case where the multilayer is not periodic. We can see that since the effective permittivity for all three cases is the same, the performance of the waveguides are almost identical. This demonstrates that the light confinement mechanism in e-skid waveguides and photonic crystal waveguides are fundamentally different. In photonic crystal waveguides, the periodicity is a requirement and a change in periodicity strongly affects the performance of the waveguide.

We have also studied the effect of periodicity on the modal effective index (n_{eff}) of TE-like and TM-like modes of a single on-chip e-skid waveguide as a function of core size at $\lambda=1550$ nm. Figure B.3 shows that EMT is an extremely accurate

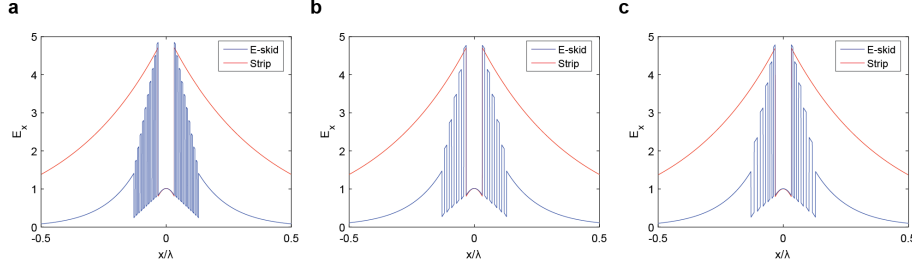


Fig. B.2. Effect of the cladding periodicity on 1D e-skid waveguides. The comparison of the x-component of the electric field at $\lambda=1550$ nm. The core is silicon with a size of 100 nm. The cladding is Si/SiO₂ multilayer with $\rho = 0.5$. (a) The periodicity is $\Lambda=10$ nm. (b) The periodicity is $\Lambda=30$ nm. (c) The periodicity linearly varies from $\Lambda=20$ nm to $\Lambda=45$ nm. The total thickness of the waveguide in all cases is 400 nm. The modal effective index (n_{eff}) for the three cases are 1.9062, 1.8864, and 1.8864, respectively. The ratio between the power confined inside the core and total power (η) for the three cases are 30.98%, 29.79%, and 29.99%, respectively. $n_{\text{eff}}=1.5281$ and $\eta=12.36\%$ when the cladding is removed. It is clearly seen that as long as the periodicity is subwavelength, the performance of e-skid waveguide depends on the effective permittivity of the multilayer cladding not the periodicity or disorder in the cladding. Thus the waveguiding mechanism in e-skid waveguides is fundamentally different from that in photonic crystal waveguides.

approximation to homogenize the cladding when the unit cell size is considerably smaller than the operating wavelength. The effect of the unit-cell size is more obvious on the effective index of the TE-like mode because the field intensity is higher in the cladding region for these modes.

B.3 Cross-talk

In the main text, we have reported the coupled power at a single wavelength. However, the coupling between two waveguides is a function of frequency in general. Figure B.4 displays the spectral response of strip and e-skid couplers. Since multilayer metamaterials are non-resonant broadband structures, multilayers show strong anisotropy for a wide range of wavelengths as long as the period is considerably smaller

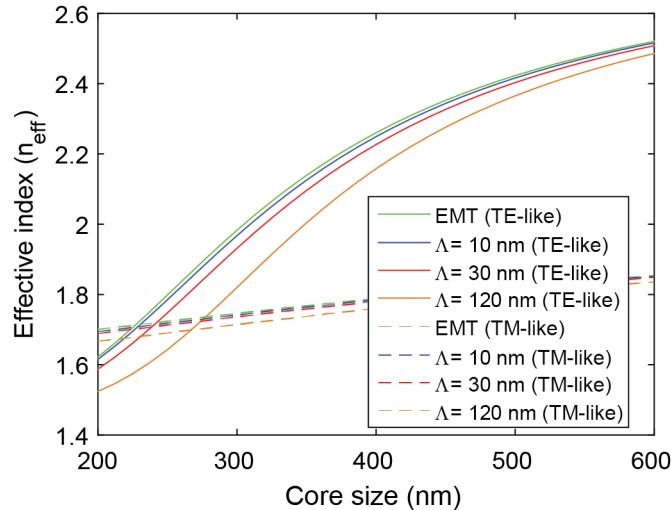


Fig. B.3. **Effect of the cladding periodicity on the modal index.**

than the wavelength. Hence, as shown in Fig. B.4, the multilayer cladding causes the cross-talk to decrease for a broad range of frequencies.

An important challenge of alternative waveguides is mode conversion efficiency from the grating coupler to the waveguide. The comparison of the output level of the through waveguide shows that the coupling efficiency from the grating coupler to the e-skid waveguides is very close to the coupling efficiency in strip waveguides. Moreover, as we explain in Supplementary note 5, the mode conversion efficiency from a strip waveguide to an e-skid waveguide with the same core size is above 98%. This means that e-skid waveguides can easily be integrated to the silicon photonics chip. Figure B.5 illustrates the normalized coupling length versus the center-to-center separation for coupled e-skid and strip waveguides. For a compact photonic circuit, minimum separation with maximum decoupling between adjacent waveguides are required [56]. However, as it is seen in Fig. B.5, the coupling length exponentially decreases as the separation is reduced. This trade-off limits the integration density of photonic circuits. Due to the reduced skin-depth in e-skid waveguides, we can reduce the decoupled separation further and increase the integration density of photonic integrated circuits. We should emphasize that the decoupled separation in

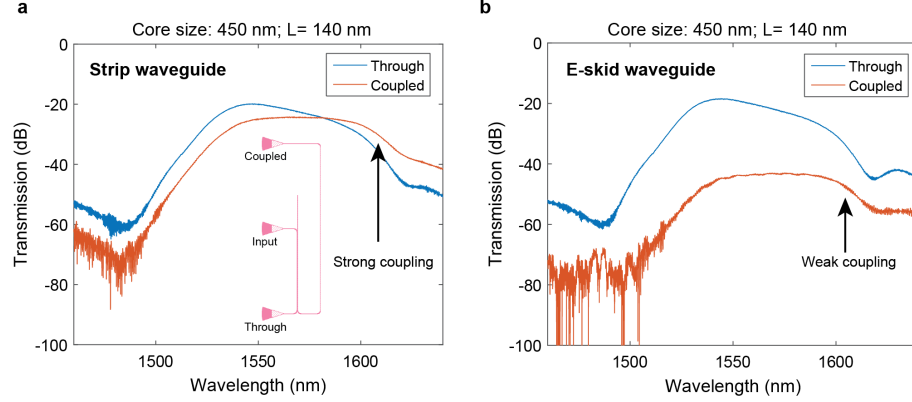


Fig. B.4. **Measured transmission spectra to the through and coupled waveguides.** **a**, Strip waveguide; **b**, e-skid waveguide. (Inset) Schematic representation of the experimental setup to measure the coupling length. Light is in-coupled through the middle grating coupler. The waveguide core size and the coupling distance (L) is 450 nm and 140 nm, respectively, in both cases. The other parameters of the waveguides are the same as the waveguides in Fig. 4 in the main text. The anisotropic cladding causes coupling to the second waveguide to drop almost 20 dB. This helps to reduce the cross-talk in dense photonic integrated circuits.

slot waveguides and photonic crystal waveguides are even more than that in strip waveguides [56].

We also contrast the effect of anisotropy on TE-like and TM-like modes of on-chip e-skid waveguides. Figure B.6 shows the coupling length for TE-like and TM-like modes versus ε_z while ε_x is fixed in the cladding. As the anisotropy increases, we can reduce the skin-depth in the cladding for TE-like mode. Thus, the coupling length between the two coupled waveguides is strongly enhanced because the overlap between evanescent waves of adjacent waveguides is suppressed. On the other hand, since the electric field in the x direction is negligible for TM-like modes, these modes cannot feel the anisotropy of the cladding. Hence, the anisotropic cladding cannot help to control the momentum of evanescent waves for TM-like modes.

To control the evanescent waves of TM-like modes, the cladding must be anisotropic in the yz plane and it must be added beneath or above the waveguide core. Figure

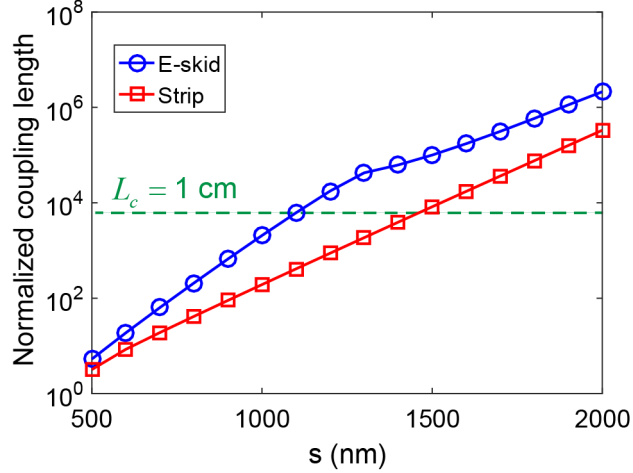


Fig. B.5. **Normalized coupling length (L_c/λ) versus the center-to-center separation between the coupled waveguides (s).** $w_0 = 450$ nm, $\Lambda = 100$ nm, and $\rho = 0.5$. Other simulation parameters are the same as those in Fig. 3 in the main text. $L_c = 1$ cm has been defined as the minimum decoupling length. In this case, the minimal separation length (center-to-center) in e-skid waveguides and strip waveguides are 1104 nm and 1466 nm, respectively. This shows that e-skid waveguides will have higher performance for dense photonic integration than strip waveguides.

B.7a (inset) illustrates a simplified structure to control the skin-depth of TM-like modes. We keep the permittivity in the y direction fixed, but we change it in the z direction to control the anisotropy. As we increase the permittivity in the z direction, the optical mode is confined inside the core and the overlap between the evanescent tails is reduced. Hence, as shown in Fig. B.7a, the coupling length increases. Figure B.7b displays a practical implementation of the anisotropic cladding for the TM-like modes composed of Si/SiO₂ multilayer claddings. In this case, $\Lambda = 40$ nm and the silicon filling fraction is $\rho = 0.5$. Figure B.7c and B.7d show the normalized electric field profile of the even mode of the coupled strip and e-skid waveguides, respectively. It is seen that the skin-depth of the evanescent waves in e-skid waveguides is reduced, and as a result, the coupling length has been increased from 14.5λ for strip waveguides case to 30.6λ for e-skid waveguides case. Note that if we add the multilayer on

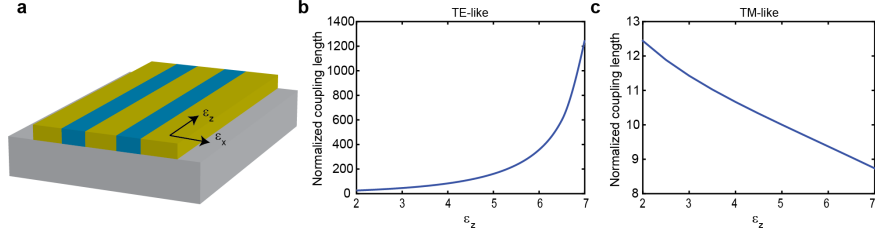


Fig. B.6. **Effect of cladding anisotropy on the coupling length for TE-like and TM-like modes of e-skid waveguides.** **a**, Schematic representation of the two coupled Si waveguides with a core size of 300 nm, height of 220 nm, and center-to-center separation of 1000 nm operating at $\lambda = 1550$ nm. The waveguides have been covered by a homogeneous anisotropic metamaterial (yellow) with $\varepsilon_x = 2$ and $\varepsilon_y = \varepsilon_z$. **b**, Coupling length for TE-like mode versus ε_z . **c**, Coupling length for TM-like mode versus ε_z . As we enhance the anisotropy of the cladding, the coupling length of TE-like mode increases as a result of skin-depth reduction in the cladding.

top of the waveguide core as well, more confinement is achievable and the cross-talk can be reduced further.

Cross-talk in E-skid Waveguides Without an Upper Cladding

In an e-skid waveguide, the waveguide cross-talk can be reduced further by increasing the anisotropy of the metamaterial. Figure B.8a shows the schematic layout to measure the cross-talk between coupled e-skid waveguides, and Fig. B.8b shows an SEM image of coupled e-skid waveguides. The parameters for the e-skid waveguide are set to $h_0 = 220$ nm, $\Lambda = 100$ nm, $\rho = 0.5$, and $N = 5$; this sets the separation distance between the two waveguides (edge-to-edge) to be $d_{\text{sep}} = 550$ nm, which is less than a free space wavelength ($\lambda = 1550$ nm). In this case, there is no upper SiO₂ cladding and the cross-section is similar to that in Fig. 3c of the main manuscript (Si/air multilayers). This leads to a higher anisotropy in metamaterials and reduces the skin-depth of the guided mode compared to the case of Si/SiO₂ multilayers. To evaluate the waveguide cross-talk, as in the main text, we have characterized the

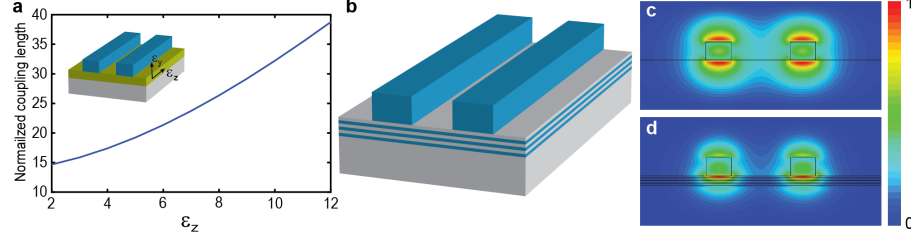


Fig. B.7. **E-skid waveguides for controlling the evanescent waves of the TM-like mode.** **a**, The schematic representation of proposed e-skid waveguides for controlling the skin-depth of the TM-like mode (inset). Since the electric field of the TM-like mode is polarized in the y direction, the cladding must be anisotropic in yz plane. To simplify the structure, the anisotropic cladding (yellow) is implemented only underneath the waveguides. The plot shows the normalized coupling length between the two waveguides versus the anisotropy of the metamaterial layer while the permittivity in the y direction is fixed to be 2.2. The thickness of the layer is 120 nm. The waveguide parameters are the same as that in Fig. B.6. **b**, Practical Si/SiO₂ multilayer structure to confine the evanescent waves and reduce the cross-talk between the two waveguides. $\Lambda = 40$ nm and the silicon filling fraction is $\rho = 0.5$. **c** and **d**, The normalized electric field profile of the even mode of the coupled strip and e-skid waveguides, respectively. It is seen that the multilayer structure helps to confine the mode inside the waveguide and reduces the overlap between the evanescent waves of the two waveguides. This results in the increase of the coupling length from 14.5λ to 30.6λ .

coupling length L_c by measuring the output power ratio (I_2/I_1) for different lengths (L) of devices. Red and blue circles in Figs. B.8c-B.8e are the measured output power ratio for e-skid and strip waveguides, respectively, and dashed lines are their respective fitting curves with $I_2/I_1 = \tan^2(\pi L/2L_c)$. Figures B.8c-B.8e are with different core widths of $w_0 = 350, 400,$ and 450 nm, respectively. Figure B.8f summarizes the normalized coupling lengths (L_c/λ) that are characterized through Figs. B.8c-B.8e: e-skid (red circles) and strip (blue circles) waveguides. The solid lines are their respective simulation results that match well with the experimental measurements. Notice that, in every case, the coupling length of an e-skid waveguide is much longer than that of a strip waveguide. The maximum coupling length of more than 3 cm is

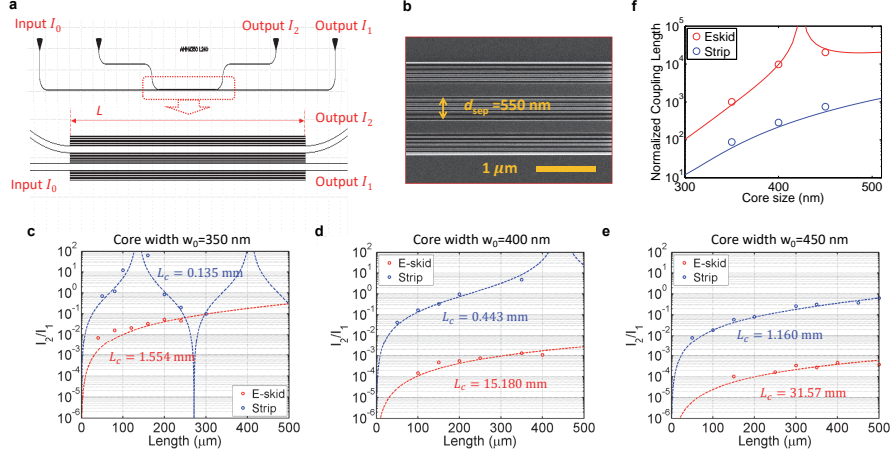


Fig. B.8. **Cross-talk in e-skid waveguides without an Upper cladding.** **a**, Schematic layout to measure the cross-talk and **b**, SEM image of coupled e-skid waveguides on an SOI platform. Geometric parameters are set to $h_0 = 220$ nm, $\Lambda = 100$ nm, $\rho = 0.5$, and $N = 5$, setting the separation distance between the two waveguides to be $d_{\text{sep}} = 550$ nm. There is no upper cladding. **c-e**, Coupling length L_c characterization by measuring the output power ratio (I_2/I_1) vs. device length L ; core widths w_0 are **(c)** 350 nm, **(d)** 400 nm, and **(e)** 450 nm, respectively. Red and blue circles are the measured power ratio for the e-skid and strip waveguides, respectively, and dashed lines are their fitting curves with $I_2/I_1 = \tan^2(\pi L/2L_c)$. **f**, Normalized coupling length (L_c/λ) for the e-skid (red circles) and strip (blue circles) waveguides. Red and blue lines are their respective simulation results.

achieved ($w_0 = 450$ nm), and, when w_0 is 400 or 450 nm, the coupling length for an e-skid waveguide is about 30 times longer in comparison with strip waveguide.

B.4 Bending loss

We have also simulated [152] and measured the bending loss when the waveguides are coated by an SiO_2 upper cladding (Fig. B.9). An oxide cladding is usually used to protect the device and to integrate it with electronic interconnects [90]. In this experiment, the input power is divided into two paths with equal lengths. It is seen

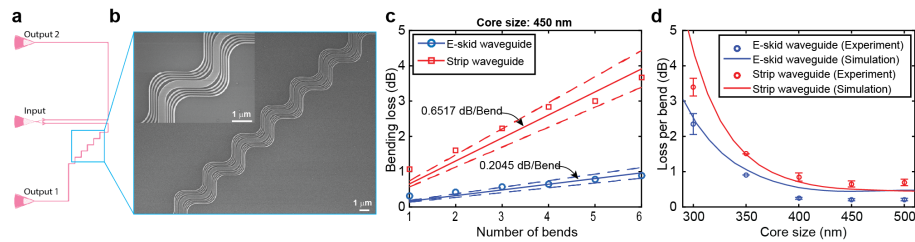


Fig. B.9. **Bending loss.** **a**, Schematic representation of the experimental setup to measure the bending loss. Light is in-coupled through the middle grating coupler. It is divided into two branches of equal length but with a different number of bends. **b**, The top view SEM image of an e-skid waveguide with multiple bends. The inset shows a closer view. The bending radius is $1 \mu\text{m}$ and the other parameters of the waveguides are the same as the waveguides in Fig. 4 in the main text. **c**, The comparison of bending loss between e-skid and strip waveguides at telecommunication wavelength. The experimental points are fitted by a straight line. **d**, The comparison of simulated and measured bending loss in e-skid and strip waveguides versus the core size indicating a considerable reduction in the bending loss, specially when the core size is small.

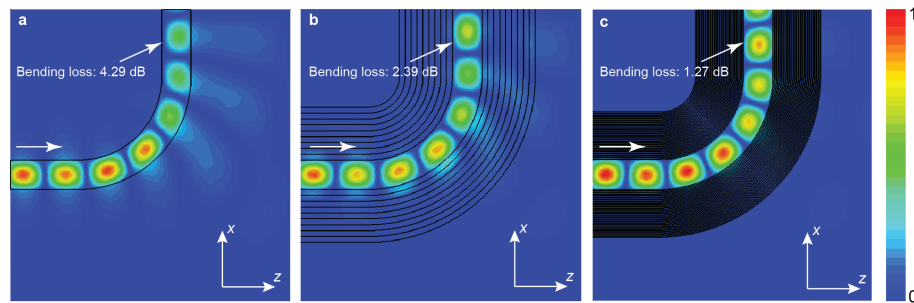


Fig. B.10. **Full-wave simulation of the TE-like mode of curved waveguides.** Full-wave simulation results of the magnetic field of the TE-like mode of curved (a) strip waveguide, (b) e-skid waveguide with $\Lambda=120$ nm, and (c) e-skid waveguide with $\Lambda=20$ nm. The waveguide core size and bending radius are 300 nm and 1 μm , respectively. Other simulation parameters of the waveguides are the same as those in Fig. B.9. The waveguides are excited from the left side. The anisotropic cladding reduces the skin-depth in the cladding. Thus, the scattering at the bend is reduced in the e-skid waveguide case. The comparison of the field amplitude at the end of the waveguides clearly shows that the bending loss in e-skid waveguide is relatively lower. In the ideal case where the periodicity is deep subwavelength, the bending loss is considerably lower in e-skid waveguides.

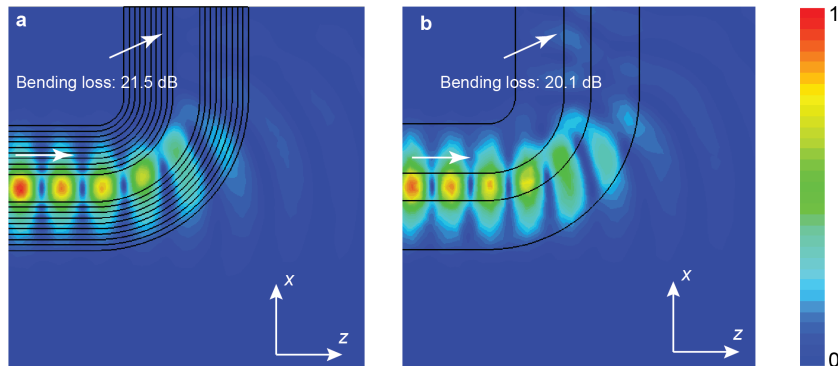


Fig. B.11. **Full-wave simulation of the TM-mode of curved waveguides.** **a**, Full-wave simulation results of the magnetic field of the TM-like mode of curved e-skid waveguide with $\Lambda=120$ nm. Other simulation parameters of the waveguides are the same as those in Fig. B.10. **b**, The field profile of the same waveguide when the multilayer cladding is replaced by an isotropic cladding with the same permittivity as the effective permittivity of the multilayer metamaterial in the y direction. Since the electric field of the TM-like mode is polarized in the y direction and the electric field in the x direction is negligible, the anisotropy does not play any role in confinement. Thus, the TM-like mode is similar to that of an isotropic cladding waveguide. Note the TE-like mode probes the anisotropy of the multi-layer cladding and is fundamentally different.

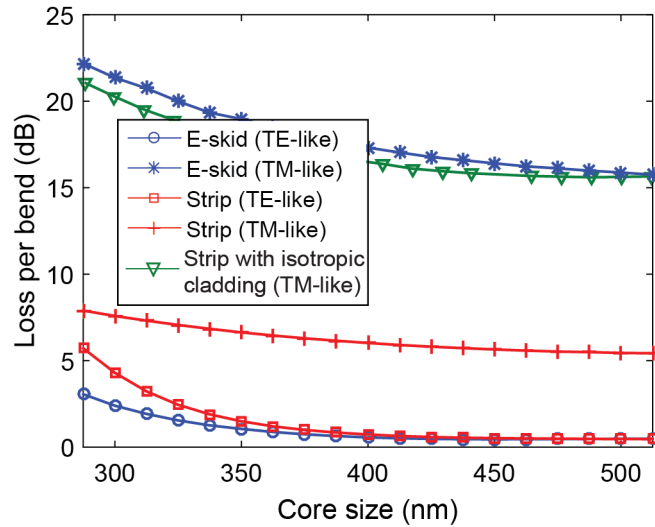


Fig. B.12. **Comparison of the full-wave simulated bending loss in e-skid and strip waveguides for both TE-like and TM-like modes.** The structure is the same as in Fig. B.10. The bending loss for TE-like modes in e-skid waveguide is lower in comparison with that in strip waveguides because the multilayer cladding confines the light inside the core and reduces the skin depth in the cladding, especially when the core size is small and a considerable fraction of the total power is in the cladding. The green curve shows the bending loss for the TM-like mode when the metamaterial cladding is replaced by an isotropic cladding with the same size and the same permittivity as the effective permittivity of the multilayer metamaterial in the y direction. It is seen that the TM-like modes do not feel the anisotropy of the multilayer cladding. Thus, the anisotropic cladding cannot help to control the evanescent waves for TM-like modes. As a result, the bending loss for TM-like modes in e-skid waveguide is even worse than that in strip waveguides.

that the bending loss is considerably reduced due to the metamaterial cladding even when the core size is large.

In the main text, we have presented the magnetic field of curved strip waveguides and e-skid waveguides using a transformation optics approach to demonstrate the effect of skin-depth on the bending loss. However, for accurate calculation of bending loss, 3D full-wave simulations are required. Figure B.10 shows the top view of the simulated [152] magnetic field profile of TE-like mode for curved strip and e-skid waveguides. It is seen that for all-cases the skin-depth extends on the right side and is compressed on the left side in agreement with the transformation optics calculations. The performance of e-skid waveguides improves if we approach the effective medium theory limit ($\Lambda \rightarrow 0$) (Fig. B.10). As we mentioned earlier, the TM-like mode of on-chip waveguides does not feel the anisotropy of the cladding because the electric field in the x direction is negligible. Hence, the confinement of the TM-like mode in e-skid cladding is the same as that in an isotropic cladding as shown in Fig. B.11.

We compare the bending loss for both TE-like and TM-like modes of e-skid and strip waveguides in Fig. B.12. As we mentioned in the main text, the additional degree of freedom in total internal reflection can be used to control evanescent waves of p-polarized (TE-like) modes. Hence, the anisotropic cladding helps to reduce the bending loss of the TE-like mode in e-skid waveguides in comparison with strip waveguides. However, this degree of freedom does not exist for s polarized (TM-like) modes. Since the effective permittivity of the cladding for the TM-like mode is larger than the permittivity of SiO_2 , the evanescent waves decay slower for TM-like modes in e-skid waveguides. Thus, the skin-depth extends more and more power is radiated at sharp bends in comparison with strip waveguides.

B.5 Mode conversion efficiency

The mode conversion efficiency between the e-skid waveguide and the strip waveguide are also investigated. For the mode conversion efficiency, we use a racetrack

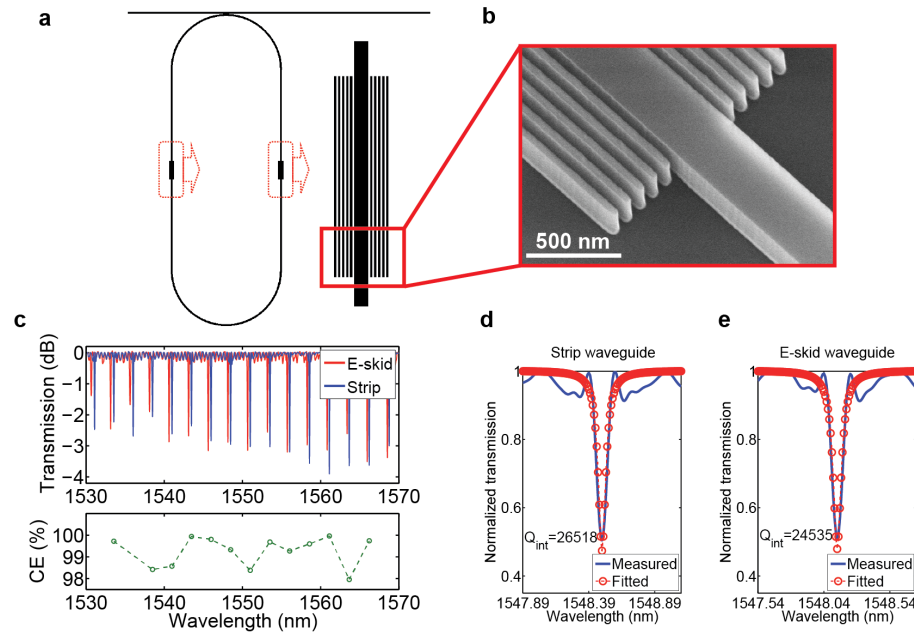


Fig. B.13. **Mode conversion efficiency.** **a**, The schematic representation of the experiment set-up. **b**, SEM image of an e-skid to strip waveguide transition. **c**, Measured transmission spectra of the racetrack resonators without (blue) and with (red) the metamaterial claddings, and characterized mode conversion efficiency (CE). **d** & **e**, Fitted resonances: (**d**) without (strip waveguide) and (**e**), with (e-skid waveguide) the metamaterial claddings. The waveguide geometries are set to $h_0 = 220$ nm, $w_0 = 350$ nm, $w\rho = w(1 - \rho) = 50$ nm, and $N = 5$.

resonator (Fig. B.13) to characterize the insertion loss efficiency [244]. Figure B.13c shows the normalized transmission spectra for the e-skid (red) and strip (blue) waveguides. The resonances are slightly shifted with metamaterials due to the different propagation phase in the e-skid waveguide (see Fig. 3 in the main text), but the extinction ratios are almost similar suggesting a similar cavity loss. Figures B.13d and B.13e are the fitted resonances for the strip and e-skid waveguides, respectively, and the intrinsic quality factors are 26,518 and 24,535, which correspond to the round-trip losses of 0.6893 dB/round and 0.7466 dB/round, respectively [245]. Since we have four interfaces for the mode conversion, a rough estimation of the mode conversion loss is about 0.0143 dB/facet, which corresponds to a mode conversion efficiency of 99.6%. The mode conversion efficiencies (CEs) with other resonances are also characterized and plotted in Fig. B.13c. This high mode conversion efficiency between the strip waveguide and the e-skid waveguide in TE-like modes indicates a low insertion loss, and suggests a high compatibility with the previously used PIC devices.

B.6 Propagation loss

To characterize the propagation losses in the e-skid and the strip waveguides, we have fabricated two sets of waveguides (e-skid and strip waveguides) with different lengths of the straight section. The waveguide parameters are set to $w_0 = 450$ nm, $h_0 = 220$ nm, $w_\rho = w_{(1-\rho)} = 50$ nm, and $N = 5$; then the lengths of the straight section of the e-skid and strip waveguides are varied from 0 to 1.8 mm. Figure B.14 shows the measured transmission powers of e-skid (blue circles) and strip (red circles) waveguides at $\lambda_0 = 1550$ nm, for different device lengths. Solid lines in each figure are the linear fitting curves that give the propagation losses of 2.65 dB/cm and 3.43 dB/cm to strip and e-skid waveguides, respectively. The propagation losses for strip and e-skid waveguides at different wavelengths have also been characterized. The average losses for strip and e-skid waveguides for wavelengths between 1540 nm to

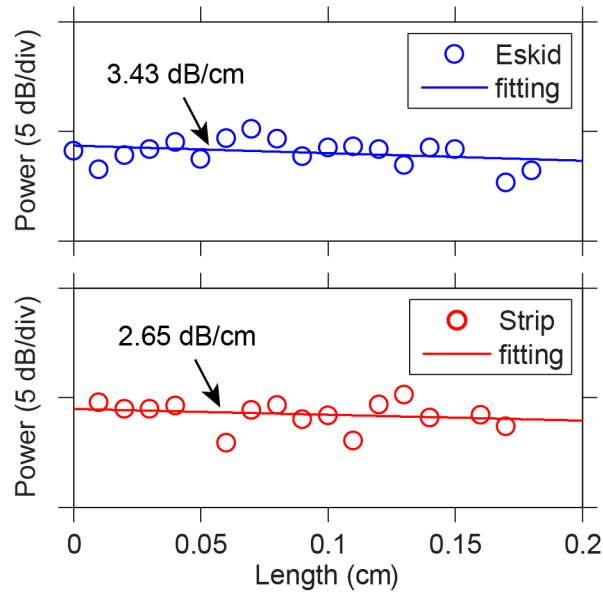


Fig. B.14. **Propagation losses in e-skid and strip waveguides.** The circles represent normalized transmission through straight e-skid (blue) and strip (red) waveguides at $\lambda = 1550$ nm. The length of the waveguides is varied from 0 to 1.8 mm to characterize the propagation loss (fitting curves). The propagation loss in e-skid and strip waveguide is 3.43 and 2.65 dB/cm at $\lambda = 1550$ nm, and the average losses for e-skid and strip waveguides for wavelengths between 1540 nm to 1560 nm are 3.67 dB/cm and 1.84 dB/cm, respectively, with a standard deviation of 1.0 dB/cm and 1.4 dB/cm, respectively. The other waveguide parameters are $w_0 = 450$ nm, $h_0 = 220$ nm, $w_\rho = w_{(1-\rho)} = 50$ nm, and $N = 5$. This clearly shows that e-skid waveguides have comparable losses to standard strip waveguides opening the path for practical applications.

1560 nm are 1.84 dB/cm and 3.67 dB/cm, respectively, with a standard deviation of 1.4 dB/cm and 1.0 dB/cm, respectively. This propagation loss of the e-skid waveguide is reasonable for compact devices, especially given that the cross-talks and bending losses are improved significantly (see Table I in Chapter 3 for comparison with other techniques).

REFERENCES

REFERENCES

- [1] P. Lodahl, S. Mahmoodian, and S. Stobbe, “Interfacing single photons and single quantum dots with photonic nanostructures,” *Reviews of Modern Physics*, vol. 87, no. 2, pp. 347–400, May 2015.
- [2] C. Schuck, W. H. P. Pernice, and H. X. Tang, “Waveguide integrated low noise NbTiN nanowire single-photon detectors with milli-Hz dark count rate,” *Scientific Reports*, vol. 3, p. 1893, May 2013.
- [3] R. Mitsch, C. Sayrin, B. Albrecht, P. Schneeweiss, and A. Rauschenbeutel, “Quantum state-controlled directional spontaneous emission of photons into a nanophotonic waveguide,” *Nature Communications*, vol. 5, p. 5713, Dec. 2014.
- [4] T. V. Mechelen and Z. Jacob, “Universal spin-momentum locking of evanescent waves,” *Optica*, vol. 3, no. 2, pp. 118–126, Feb. 2016.
- [5] F. Kalhor, T. Thundat, and Z. Jacob, “Universal spin-momentum locked optical forces,” *Applied Physics Letters*, vol. 108, no. 6, p. 061102, Feb. 2016.
- [6] S. Pendharker, F. Kalhor, T. Van Mechelen, S. Jahani, N. Nazemifard, T. Thundat, and Z. Jacob, “Spin photonic forces in non-reciprocal waveguides,” *Optics Express*, vol. 26, no. 18, pp. 23 898–23 910, 2018.
- [7] C. L. Cortes and Z. Jacob, “Super-Coulombic atomatom interactions in hyperbolic media,” *Nature Communications*, vol. 8, p. 14144, Jan. 2017.
- [8] A. González-Tudela, C.-L. Hung, D. E. Chang, J. I. Cirac, and H. J. Kimble, “Subwavelength vacuum lattices and atomatom interactions in two-dimensional photonic crystals,” *Nature Photonics*, vol. 9, no. 5, pp. 320–325, May 2015.
- [9] E. Yablonovitch, “Inhibited Spontaneous Emission in Solid-State Physics and Electronics,” *Physical Review Letters*, vol. 58, no. 20, pp. 2059–2062, May 1987.
- [10] H. N. S. Krishnamoorthy, Z. Jacob, E. Narimanov, I. Kretzschmar, and V. M. Menon, “Topological Transitions in Metamaterials,” *Science*, vol. 336, no. 6078, pp. 205–209, Apr. 2012.
- [11] K. J. Vahala, “Optical microcavities,” *Nature*, vol. 424, pp. 839–846, Aug. 2003.
- [12] Y. Guo and Z. Jacob, “Fluctuational electrodynamics of hyperbolic metamaterials,” *Journal of Applied Physics*, vol. 115, no. 23, p. 234306, Jun. 2014.
- [13] T. Aoki, B. Dayan, E. Wilcut, W. P. Bowen, A. S. Parkins, T. J. Kippenberg, K. J. Vahala, and H. J. Kimble, “Observation of strong coupling between one atom and a monolithic microresonator,” *Nature*, vol. 443, no. 7112, pp. 671–674, Oct. 2006.

- [14] J. P. Reithmaier, G. Sk, A. Lffler, C. Hofmann, S. Kuhn, S. Reitzenstein, L. V. Keldysh, V. D. Kulakovskii, T. L. Reinecke, and A. Forchel, “Strong coupling in a single quantum dotsemiconductor microcavity system,” *Nature*, vol. 432, no. 7014, pp. 197–200, Nov. 2004.
- [15] K. Srinivasan and O. Painter, “Linear and nonlinear optical spectroscopy of a strongly coupled microdiskquantum dot system,” *Nature*, vol. 450, no. 7171, pp. 862–865, Dec. 2007.
- [16] T. Yoshie, A. Scherer, J. Hendrickson, G. Khitrova, H. M. Gibbs, G. Rupper, C. Ell, O. B. Shchekin, and D. G. Deppe, “Vacuum Rabi splitting with a single quantum dot in a photonic crystal nanocavity,” *Nature*, vol. 432, no. 7014, pp. 200–203, Nov. 2004.
- [17] J. T. Choy, B. J. M. Hausmann, T. M. Babinec, I. Bulu, M. Khan, P. Maletinsky, A. Yacoby, and M. Lonar, “Enhanced single-photon emission from a diamond-silver aperture,” *Nature Photonics*, vol. 5, no. 12, pp. 738–743, Oct. 2011.
- [18] A. Faraon, P. E. Barclay, C. Santori, K.-M. C. Fu, and R. G. Beausoleil, “Resonant enhancement of the zero-phonon emission from a colour centre in a diamond cavity,” *Nature Photonics*, vol. 5, no. 5, pp. 301–305, May 2011.
- [19] A. V. Akimov, A. Mukherjee, C. L. Yu, D. E. Chang, A. S. Zibrov, P. R. Hemmer, H. Park, and M. D. Lukin, “Generation of single optical plasmons in metallic nanowires coupled to quantum dots,” *Nature*, vol. 450, no. 7168, pp. 402–406, Nov. 2007.
- [20] D. A. B. Miller, “Are optical transistors the logical next step?” *Nature Photonics*, vol. 4, no. 1, pp. 3–5, Jan. 2010.
- [21] H. Gibbs, *Optical Bistability: Controlling Light With Light*. Elsevier, 2012.
- [22] M. F. Yanik, S. Fan, M. Soljačić, and J. D. Joannopoulos, “All-optical transistor action with bistable switching in a photonic crystal cross-waveguide geometry,” *Optics Letters*, vol. 28, no. 24, pp. 2506–2508, Dec. 2003.
- [23] A. Krasnok, S. Li, S. Lepeshov, R. Savelev, D. G. Baranov, and A. Alù, “All-Optical Switching and Unidirectional Plasmon Launching with Nonlinear Dielectric Nanoantennas,” *Physical Review Applied*, vol. 9, no. 1, p. 014015, Jan. 2018.
- [24] P. Bermel, A. Rodriguez, S. G. Johnson, J. D. Joannopoulos, and M. Soljačić, “Single-photon all-optical switching using waveguide-cavity quantum electrodynamics,” *Physical Review A*, vol. 74, no. 4, p. 043818, Oct. 2006.
- [25] D. E. Chang, A. S. Srensen, E. A. Demler, and M. D. Lukin, “A single-photon transistor using nanoscale surface plasmons,” *Nature Physics*, vol. 3, no. 11, pp. 807–812, Nov. 2007.
- [26] D. Tiarks, S. Baur, K. Schneider, S. Drr, and G. Rempe, “Single-Photon Transistor Using a F\”orster Resonance,” *Physical Review Letters*, vol. 113, no. 5, p. 053602, Jul. 2014.
- [27] H. Gorniaczyk, C. Tresp, J. Schmidt, H. Fedder, and S. Hofferberth, “Single-Photon Transistor Mediated by Interstate Rydberg Interactions,” *Physical Review Letters*, vol. 113, no. 5, p. 053601, Jul. 2014.

- [28] A. Yariv and P. Yeh, *Photonics: Optical Electronics in Modern Communications*, sixth edition edition ed. Oxford University Press, Jan. 2006.
- [29] D. Axelrod, N. L. Thompson, and T. P. Burghardt, “Total internal reflection fluorescent microscopy,” *Journal of Microscopy*, vol. 129, no. 1, pp. 19–28.
- [30] R.-M. Ma, R. F. Oulton, V. J. Sorger, G. Bartal, and X. Zhang, “Room-temperature sub-diffraction-limited plasmon laser by total internal reflection,” *Nature Materials*, vol. 10, no. 2, pp. 110–113.
- [31] S. Bassiri, C. H. Papas, and N. Engheta, “Electromagnetic wave propagation through a dielectricchiral interface and through a chiral slab,” *JOSA A*, vol. 5, no. 9, pp. 1450–1459.
- [32] V. G. Veselago, “The electrodynamics of substances with simultaneously negative values of ϵ and μ ,” *Soviet Physics Uspekhi*, vol. 10, no. 4, pp. 509–514.
- [33] J. B. Pendry, “Negative refraction makes a perfect lens,” *Physical Review Letters*, vol. 85, no. 18, pp. 3966–3969.
- [34] J. D. Joannopoulos, S. G. Johnson, J. N. Winn, and R. D. Meade, *Photonic Crystals: Molding the Flow of Light, Second Edition*. Princeton University Press, Mar. 2008.
- [35] T. M. Jordan, J. C. Partridge, and N. W. Roberts, “Non-polarizing broadband multilayer reflectors in fish,” *Nature Photonics*, vol. 6, no. 11, pp. 759–763.
- [36] G. England, M. Kolle, P. Kim, M. Khan, P. Muoz, E. Mazur, and J. Aizenberg, “Bioinspired micrograting arrays mimicking the reverse color diffraction elements evolved by the butterfly pierella luna,” *Proceedings of the National Academy of Sciences*, vol. 111, no. 44, pp. 15 630–15 634.
- [37] N. Yu, P. Genevet, M. A. Kats, F. Aieta, J.-P. Tetienne, F. Capasso, and Z. Gaburro, “Light propagation with phase discontinuities: Generalized laws of reflection and refraction,” *Science*, vol. 334, no. 6054, pp. 333–337.
- [38] N. Yu and F. Capasso, “Flat optics with designer metasurfaces,” *Nature Materials*, vol. 13, no. 2, pp. 139–150.
- [39] S. M. Kamali, E. Arbabi, A. Arbabi, and A. Faraon, “A review of dielectric optical metasurfaces for wavefront control,” *Nanophotonics*, vol. 7, no. 6, pp. 1041–1068, 2018.
- [40] D. Lin, P. Fan, E. Hasman, and M. L. Brongersma, “Dielectric gradient metasurface optical elements,” *Science*, vol. 345, no. 6194, pp. 298–302.
- [41] X. Ni, N. K. Emani, A. V. Kildishev, A. Boltasseva, and V. M. Shalaev, “Broadband light bending with plasmonic nanoantennas,” *Science*, vol. 335, no. 6067, pp. 427–427.
- [42] M. Khorasaninejad and F. Capasso, “Metalenses: Versatile multifunctional photonic components,” *Science*, vol. 358, no. 6367, p. eaam8100, 2017.

- [43] S. M. Kamali, E. Arbabi, A. Arbabi, Y. Horie, M. Faraji-Dana, and A. Faraon, “Angle-multiplexed metasurfaces: Encoding independent wavefronts in a single metasurface under different illumination angles,” *Physical Review X*, vol. 7, no. 4, p. 041056, 2017.
- [44] S. Jahani and Z. Jacob, “Transparent subdiffraction optics: nanoscale light confinement without metal,” *Optica*, vol. 1, no. 2, pp. 96–100, Aug. 2014.
- [45] A. Blais, R.-S. Huang, A. Wallraff, S. M. Girvin, and R. J. Schoelkopf, “Cavity quantum electrodynamics for superconducting electrical circuits: An architecture for quantum computation,” *Physical Review A*, vol. 69, no. 6, p. 062320, 2004.
- [46] R. Soref, “The Past, Present, and Future of Silicon Photonics,” *IEEE Journal of Selected Topics in Quantum Electronics*, vol. 12, no. 6, pp. 1678–1687, Nov. 2006.
- [47] P. Berini, “Plasmon-polariton waves guided by thin lossy metal films of finite width: Bound modes of symmetric structures,” *Physical Review B*, vol. 61, no. 15, pp. 10484–10503.
- [48] J. A. Dionne, L. A. Sweatlock, H. A. Atwater, and A. Polman, “Plasmon slot waveguides: Towards chip-scale propagation with subwavelength-scale localization,” *Physical Review B*, vol. 73, no. 3, p. 035407, Jan. 2006.
- [49] D. F. P. Pile and D. K. Gramotnev, “Channel plasmonpolariton in a triangular groove on a metal surface,” *Optics Letters*, vol. 29, no. 10, pp. 1069–1071.
- [50] D. K. Gramotnev and S. I. Bozhevolnyi, “Plasmonics beyond the diffraction limit,” *Nature Photonics*, vol. 4, no. 2, pp. 83–91, Feb. 2010.
- [51] R. F. Oulton, V. J. Sorger, D. A. Genov, D. F. P. Pile, and X. Zhang, “A hybrid plasmonic waveguide for subwavelength confinement and long-range propagation,” *Nature Photonics*, vol. 2, no. 8, pp. 496–500, Aug. 2008.
- [52] M. Silveirinha and N. Engheta, “Tunneling of electromagnetic energy through subwavelength channels and bends using ϵ -near-zero materials,” *Physical Review Letters*, vol. 97, no. 15, p. 157403.
- [53] V. R. Almeida, Q. Xu, C. A. Barrios, and M. Lipson, “Guiding and confining light in void nanostructure,” *Optics Letters*, vol. 29, no. 11, pp. 1209–1211, Jun. 2004.
- [54] S. Hu, M. Khater, R. Salas-Montiel, E. Kratschmer, S. Engelmann, W. M. Green, and S. M. Weiss, “Experimental realization of deep-subwavelength confinement in dielectric optical resonators,” *Science advances*, vol. 4, no. 8, p. eaat2355, 2018.
- [55] T. F. Krauss, “Planar photonic crystal waveguide devices for integrated optics,” *physica status solidi (a)*, vol. 197, no. 3, pp. 688–702.
- [56] D. Dai, Y. Shi, and S. He, “Comparative study of the integration density for passive linear planar light-wave circuits based on three different kinds of nanophotonic waveguide,” *Applied Optics*, vol. 46, no. 7, pp. 1126–1131, Mar. 2007.

- [57] I. Liberal and N. Engheta, “Near-zero refractive index photonics,” *Nature Photonics*, vol. 11, no. 3, p. 149, Mar. 2017.
- [58] N. Kinsey, C. DeVault, J. Kim, M. Ferrera, V. M. Shalaev, and A. Boltas-seva, “Epsilon-near-zero Al-doped ZnO for ultrafast switching at telecom wavelengths,” *Optica*, vol. 2, no. 7, pp. 616–622, Jul. 2015.
- [59] M. Z. Alam, I. D. Leon, and R. W. Boyd, “Large optical nonlinearity of indium tin oxide in its epsilon-near-zero region,” *Science*, vol. 352, no. 6287, pp. 795–797, May 2016.
- [60] C. L. Cortes, W. Newman, S. Molesky, and Z. Jacob, “Quantum nanophotonics using hyperbolic metamaterials,” *Journal of Optics*, vol. 14, no. 6, p. 063001, Jun. 2012.
- [61] S. Jahani, H. Zhao, and Z. Jacob, “Switching Purcell effect with nonlinear epsilon-near-zero media,” *Applied Physics Letters*, vol. 113, no. 2, p. 021103, 2018.
- [62] N. C. Harris, D. Grassani, A. Simbula, M. Pant, M. Galli, T. Baehr-Jones, M. Hochberg, D. Englund, D. Bajoni, and C. Galland, “Integrated source of spectrally filtered correlated photons for large-scale quantum photonic systems,” *Physical Review X*, vol. 4, no. 4, p. 041047, 2014.
- [63] S. Khasminskaya, F. Pyatkov, K. Słowik, S. Ferrari, O. Kahl, V. Kovalyuk, P. Rath, A. Vetter, F. Hennrich, M. M. Kappes *et al.*, “Fully integrated quantum photonic circuit with an electrically driven light source,” *Nature Photonics*, vol. 10, no. 11, p. 727, 2016.
- [64] H. Takesue, S. W. Nam, Q. Zhang, R. H. Hadfield, T. Honjo, K. Tamaki, and Y. Yamamoto, “Quantum key distribution over a 40-dB channel loss using superconducting single-photon detectors,” *Nature Photonics*, vol. 1, no. 6, p. 343, Jun. 2007.
- [65] C. M. Natarajan, M. G. Tanner, and R. H. Hadfield, “Superconducting nanowire single-photon detectors: physics and applications,” *Superconductor Science and Technology*, vol. 25, no. 6, p. 063001, 2012.
- [66] J. Renema, R. Gaudio, Q. Wang, Z. Zhou, A. Gaggero, F. Mattioli, R. Leoni, D. Sahin, M. de Dood, A. Fiore, and M. van Exter, “Experimental Test of Theories of the Detection Mechanism in a Nanowire Superconducting Single Photon Detector,” *Physical Review Letters*, vol. 112, no. 11, p. 117604, Mar. 2014.
- [67] B. A. Korzh, Q.-Y. Zhao, S. Frasca, J. P. Allmaras, T. M. Autry, E. A. Bersin, M. Colangelo, G. M. Crouch, A. E. Dane, T. Gerrits, F. Marsili, G. Moody, E. Ramirez, J. D. Rezac, M. J. Stevens, E. E. Wollman, D. Zhu, P. D. Hale, K. L. Silverman, R. P. Mirin, S. W. Nam, M. D. Shaw, and K. K. Berggren, “Demonstrating sub-3 ps temporal resolution in a superconducting nanowire single-photon detector,” *arXiv:1804.06839 [cond-mat, physics:physics, physics:quant-ph]*, Apr. 2018, arXiv: 1804.06839.
- [68] B. Korzh, Q.-Y. Zhao, S. Frasca, D. Zhu, E. Ramirez, E. Bersin, M. Colangelo, A. Dane, A. Beyer, J. Allmaras *et al.*, “Wsi superconducting nanowire single photon detector with a temporal resolution below 5 ps,” *CLEO: QELS_Fundamental Science*, no. 5, pp. FW3F–3, 2018.

- [69] S. Jahani, L. P. Yang, A. B. Tepole, J. C. Bardin, H. X. Tang, and Z. Jacob, “Probabilistic vortex crossing model for superconducting nanowire single-photon detectors: quantum timing jitter and spectral dependence of quantum efficiency,” (*Preparing to submit*).
- [70] D. A. Miller, “Device requirements for optical interconnects to silicon chips,” *Proceedings of the IEEE*, vol. 97, no. 7, pp. 1166–1185, 2009.
- [71] Z. Han and S. I. Bozhevolnyi, “Radiation guiding with surface plasmon polaritons,” *Reports on Progress in Physics*, vol. 76, no. 1, p. 016402, 2012.
- [72] R. Zia, M. D. Selker, P. B. Catrysse, and M. L. Brongersma, “Geometries and materials for subwavelength surface plasmon modes,” *JOSA A*, vol. 21, no. 12, pp. 2442–2446, 2004.
- [73] G. Wiederhecker, C. M. d. B. Cordeiro, F. Couny, F. Benabid, S. Maier, J. Knight, C. Cruz, and H. Fragnito, “Field enhancement within an optical fibre with a subwavelength air core,” *Nature photonics*, vol. 1, no. 2, p. 115, 2007.
- [74] C. Koos, P. Vorreau, T. Vallaitis, P. Dumon, W. Bogaerts, R. Baets, B. Es-embeson, I. Biaggio, T. Michinobu, F. Diederich *et al.*, “All-optical high-speed signal processing with silicon–organic hybrid slot waveguides,” *Nature photonics*, vol. 3, no. 4, p. 216, 2009.
- [75] J. D. Joannopoulos, P. R. Villeneuve, and S. Fan, “Photonic crystals: putting a new twist on light,” *Nature*, vol. 386, no. 6621, p. 143, 1997.
- [76] S.-Y. Lin, E. Chow, V. Hietala, P. R. Villeneuve, and J. D. Joannopoulos, “Experimental demonstration of guiding and bending of electromagnetic waves in a photonic crystal,” *Science*, vol. 282, no. 5387, pp. 274–276, 1998.
- [77] S. Tomljenovic-Hanic, C. Martijn de Sterke, and M. J. Steel, “Packing density of conventional waveguides and photonic crystal waveguides,” *Optics Communications*, vol. 259, no. 1, pp. 142–148, 2017.
- [78] S. A. Maier, “Plasmonic field enhancement and SERS in the effective mode volume picture,” *Optics Express*, vol. 14, no. 5, pp. 1957–1964, 2006.
- [79] P. Berini, “Figures of merit for surface plasmon waveguides,” *Optics Express*, vol. 14, no. 26, pp. 13 030–13 042, 2006.
- [80] M. F. Weber, C. A. Stover, L. R. Gilbert, T. J. Nevitt, and A. J. Ouderkirk, “Giant birefringent optics in multilayer polymer mirrors,” *Science*, vol. 287, no. 5462, pp. 2451–2456, 2000.
- [81] A. Fiore, V. Berger, E. Rosencher, P. Bravetti, and J. Nagle, “Phase matching using an isotropic nonlinear optical material,” *Nature*, vol. 391, no. 6666, pp. 463–466, Jan. 1998.
- [82] G. Veronis and S. Fan, “Crosstalk between three-dimensional plasmonic slot waveguides,” *Optics Express*, vol. 16, no. 3, p. 2129, 2008.
- [83] P. B. Catrysse and S. Fan, “Transverse electromagnetic modes in aperture waveguides containing a metamaterial with extreme anisotropy,” *Physical Review Letters*, vol. 106, no. 22, p. 223902, 2011.

- [84] F. Goos and H. Hänchen, “Ein neuer und fundamentaler versuch zur totalreflexion,” *Annalen der Physik*, vol. 436, no. 7-8, pp. 333–346, 1947.
- [85] M. McGuirk and C. Carniglia, “An angular spectrum representation approach to the goos-hänchen shift,” *JOSA*, vol. 67, no. 1, pp. 103–107, 1977.
- [86] B. Jalali and S. Fathpour, “Silicon Photonics,” *Journal of Lightwave Technology*, vol. 24, no. 12, pp. 4600–4615, Dec. 2006.
- [87] W. Bogaerts, R. Baets, P. Dumon, V. Wiaux, S. Beckx, D. Taillaert, B. Luyssaert, J. V. Campenhout, P. Bienstman, and D. V. Thourhout, “Nanophotonic waveguides in silicon-on-insulator fabricated with CMOS technology,” *Journal of Lightwave Technology*, vol. 23, no. 1, pp. 401–412, Jan. 2005.
- [88] R. Nagarajan, C. H. Joyner, R. P. Schneider, J. S. Bostak, T. Butrie, A. G. Dentai, V. G. Dominic, P. W. Evans, M. Kato, M. Kauffman, D. J. H. Lambert, S. K. Mathis, A. Mathur, R. H. Miles, M. L. Mitchell, M. J. Missey, S. Murthy, A. C. Nilsson, F. H. Peters, S. C. Pennypacker, J. L. Pleumeekers, R. A. Salvatore, R. K. Schlenker, R. B. Taylor, H.-S. Tsai, M. F. V. Leeuwen, J. Webjorn, M. Ziari, D. Perkins, J. Singh, S. G. Grubb, M. S. Reffle, D. G. Mehuys, F. A. Kish, and D. F. Welch, “Large-scale photonic integrated circuits,” *IEEE Journal of Selected Topics in Quantum Electronics*, vol. 11, no. 1, pp. 50–65, Jan. 2005.
- [89] S. Kim, K. Han, C. Wang, J. A. Jaramillo-Villegas, X. Xue, C. Bao, Y. Xuan, D. E. Leaird, A. M. Weiner, and M. Qi, “Dispersion engineering and frequency comb generation in thin silicon nitride concentric microresonators,” *Nature Communications*, vol. 8, no. 1, p. 372, Aug. 2017.
- [90] L. Chrostowski and M. Hochberg, *Silicon Photonics Design: From Devices to Systems*. Cambridge University Press, May 2015.
- [91] D. Dai, J. Bauters, and J. E. Bowers, “Passive technologies for future large-scale photonic integrated circuits on silicon: polarization handling, light non-reciprocity and loss reduction,” *Light: Science & Applications*, vol. 1, no. 3, p. e1, Mar. 2012.
- [92] M. J. R. Heck, J. F. Bauters, M. L. Davenport, J. K. Doylend, S. Jain, G. Kurczveil, S. Srinivasan, Y. Tang, and J. E. Bowers, “Hybrid Silicon Photonic Integrated Circuit Technology,” *IEEE Journal of Selected Topics in Quantum Electronics*, vol. 19, no. 4, pp. 6 100 117–6 100 117, Jul. 2013.
- [93] L.-W. Luo, N. Ophir, C. P. Chen, L. H. Gabrielli, C. B. Poitras, K. Bergmen, and M. Lipson, “WDM-compatible mode-division multiplexing on a silicon chip,” *Nature Communications*, vol. 5:3069, 2014.
- [94] B. Momeni, S. Yegnanarayanan, M. Soltani, A. A. Eftekhar, E. S. Hosseini, and A. Adibi, “Silicon nanophotonic devices for integrated sensing,” *Journal of Nanophotonics*, vol. 3, no. 1, p. 031001, Apr. 2009.
- [95] Y. Shen, N. C. Harris, S. Skirlo, M. Prabhu, T. Baehr-Jones, M. Hochberg, X. Sun, S. Zhao, H. Larochelle, D. Englund, and M. Soljačić, “Deep learning with coherent nanophotonic circuits,” *Nature Photonics*, vol. 11, no. 7, pp. 441–446, Jul. 2017.

- [96] E. Luan, H. Shoman, D. M. Ratner, K. C. Cheung, and L. Chrostowski, “Silicon photonic biosensors using label-free detection,” 2018.
- [97] D. M. Kita, J. Michon, S. G. Johnson, and J. Hu, “Are slot and sub-wavelength grating waveguides better than strip waveguides for sensing?” *Optica*, vol. 5, no. 9, pp. 1046–1054, 2018.
- [98] A. Alù and N. Engheta, “All Optical Metamaterial Circuit Board at the Nanoscale,” *Physical Review Letters*, vol. 103, no. 14, p. 143902, Sep. 2009.
- [99] S. Kim and M. Qi, “Mode-evolution-based polarization rotation and coupling between silicon and hybrid plasmonic waveguides,” *Sci. Rep.*, vol. 5, p. 18378, 2015.
- [100] —, “Polarization rotation and coupling between silicon waveguide and hybrid plasmonic waveguide,” *Opt. Express*, vol. 23, no. 8, pp. 9968–9978, 2015.
- [101] S. Raza, N. Stenger, A. Pors, T. Holmgaard, S. Kadkhodazadeh, J. B. Wagner, K. Pedersen, M. Wubs, S. I. Bozhevolnyi, and N. A. Mortensen, “Extremely confined gap surface-plasmon modes excited by electrons,” *Nature Communications*, vol. 5, p. 4125, Jun. 2014.
- [102] N. Kinsey, M. Ferrera, V. M. Shalaev, and A. Boltasseva, “Examining nanophotonics for integrated hybrid systems: a review of plasmonic interconnects and modulators using traditional and alternative materials [Invited],” *Journal of the Optical Society of America B*, vol. 32, no. 1, p. 121, Jan. 2015.
- [103] J. B. Khurgin, “How to deal with the loss in plasmonics and metamaterials,” *Nature Nanotechnology*, vol. 10, no. 1, pp. 2–6, Jan. 2015.
- [104] —, “Replacing noble metals with alternative materials in plasmonics and metamaterials: how good an idea?” *Phil. Trans. R. Soc. A*, vol. 375, no. 2090, p. 20160068, Mar. 2017.
- [105] S. Jahani and Z. Jacob, “All-dielectric metamaterials,” *Nature Nanotechnology*, vol. 11, no. 1, pp. 23–36, 2016.
- [106] F. Priolo, T. Gregorkiewicz, M. Galli, and T. F. Krauss, “Silicon nanostructures for photonics and photovoltaics,” *Nature Nanotechnology*, vol. 9, no. 1, p. 19, Jan. 2014.
- [107] A. I. Kuznetsov, A. E. Miroschnichenko, M. L. Brongersma, Y. S. Kivshar, and B. Lukyanichuk, “Optically resonant dielectric nanostructures,” *Science*, vol. 354, no. 6314, p. aag2472, Nov. 2016.
- [108] I. Staude and J. Schilling, “Metamaterial-inspired silicon nanophotonics,” *Nature Photonics*, vol. 11, no. 5, pp. 274–284, May 2017.
- [109] P. Cheben, R. Halir, J. H. Schmid, H. A. Atwater, and D. R. Smith, “Subwavelength integrated photonics,” *Nature*, vol. 560, no. 7720, pp. 565–572, Aug. 2018.
- [110] C. J. Chang-Hasnain and W. Yang, “High-contrast gratings for integrated optoelectronics,” *Advances in Optics and Photonics*, vol. 4, no. 3, pp. 379–440, Sep. 2012.

- [111] A. E. Krasnok, A. E. Miroschnichenko, P. A. Belov, and Y. S. Kivshar, “All-dielectric optical nanoantennas,” *Optics Express*, vol. 20, no. 18, pp. 20 599–20 604, Aug. 2012.
- [112] D. G. Baranov, D. A. Zuev, S. I. Lepeshov, O. V. Kotov, A. E. Krasnok, A. B. Evlyukhin, and B. N. Chichkov, “All-dielectric nanophotonics: the quest for better materials and fabrication techniques,” *Optica*, vol. 4, no. 7, pp. 814–825, 2017.
- [113] W. Liu, A. E. Miroschnichenko, and Y. S. Kivshar, “Q-factor enhancement in all-dielectric anisotropic nanoresonators,” *Physical Review B*, vol. 94, no. 19, p. 195436, Nov. 2016.
- [114] A. Arbabi, Y. Horie, M. Bagheri, and A. Faraon, “Dielectric metasurfaces for complete control of phase and polarization with subwavelength spatial resolution and high transmission,” *Nature Nanotechnology*, vol. 10, no. 11, pp. 937–943, Nov. 2015.
- [115] E. Arbabi, A. Arbabi, S. M. Kamali, Y. Horie, and A. Faraon, “Multiwavelength polarization-insensitive lenses based on dielectric metasurfaces with meta-molecules,” *Optica*, vol. 3, no. 6, pp. 628–633, Jun. 2016.
- [116] M. Khorasaninejad, W. T. Chen, R. C. Devlin, J. Oh, A. Y. Zhu, and F. Capasso, “Metalenses at visible wavelengths: Diffraction-limited focusing and subwavelength resolution imaging,” *Science*, vol. 352, no. 6290, pp. 1190–1194, Jun. 2016.
- [117] B. Shen, P. Wang, R. Polson, and R. Menon, “An integrated-nanophotonics polarization beamsplitter with 2.4 × 2.4 m² footprint,” *Nature Photonics*, vol. 9, no. 6, pp. 378–382, Jun. 2015.
- [118] A. Y. Piggott, J. Lu, K. G. Lagoudakis, J. Petykiewicz, T. M. Babinec, and J. Vuckovic, “Inverse design and demonstration of a compact and broadband on-chip wavelength demultiplexer,” *Nature Photonics*, vol. 9, no. 6, pp. 374–377, Jun. 2015.
- [119] M. Hafezi, S. Mittal, J. Fan, A. Migdall, and J. M. Taylor, “Imaging topological edge states in silicon photonics,” *Nature Photonics*, vol. 7, no. 12, p. 1001, Dec. 2013.
- [120] A. Slobozhanyuk, S. H. Mousavi, X. Ni, D. Smirnova, Y. S. Kivshar, and A. B. Khanikaev, “Three-dimensional all-dielectric photonic topological insulator,” *Nature Photonics*, vol. 11, no. 2, p. 130, 2017.
- [121] H. Benisty, C. Weisbuch, D. Labilloy, M. Rattier, C. J. M. Smith, T. F. Krauss, R. M. d. I. Rue, R. Houdre, U. Oesterle, C. Jouanin, and D. Cassagne, “Optical and confinement properties of two-dimensional photonic crystals,” *Journal of Lightwave Technology*, vol. 17, no. 11, pp. 2063–2077, Nov. 1999.
- [122] C. W. Hsu, B. Zhen, J. Lee, S.-L. Chua, S. G. Johnson, J. D. Joannopoulos, and M. Soljačić, “Observation of trapped light within the radiation continuum,” *Nature*, vol. 499, no. 7457, p. 188, Jul. 2013.

- [123] A. Mekis, J. C. Chen, I. Kurland, S. Fan, P. R. Villeneuve, and J. D. Joannopoulos, “High Transmission through Sharp Bends in Photonic Crystal Waveguides,” *Physical Review Letters*, vol. 77, no. 18, pp. 3787–3790, Oct. 1996.
- [124] W. Song, R. Gatlula, S. Abbaslou, M. Lu, A. Stein, W. Y.-C. Lai, J. Provine, R. F. W. Pease, D. N. Christodoulides, and W. Jiang, “High-density waveguide superlattices with low crosstalk,” *Nature Communications*, vol. 6, p. 7027, May 2015.
- [125] M. Mrejen, H. Suchowski, T. Hatakeyama, C. Wu, L. Feng, K. O’Brien, Y. Wang, and X. Zhang, “Adiabatic elimination-based coupling control in densely packed subwavelength waveguides,” *Nature Communications*, vol. 6, p. 7565, Jun. 2015.
- [126] L. H. Gabrielli, D. Liu, S. G. Johnson, and M. Lipson, “On-chip transformation optics for multimode waveguide bends,” *Nature Communications*, vol. 3, p. 1217, Nov. 2012.
- [127] B. Shen, R. Polson, and R. Menon, “Metamaterial-waveguide bends with effective bend radius $\lambda_0/2$,” *Optics Letters*, vol. 40, no. 24, pp. 5750–5753, Dec. 2015.
- [128] —, “Increasing the density of passive photonic-integrated circuits via nanophotonic cloaking,” *Nature Communications*, vol. 7, p. 13126, Nov. 2016.
- [129] S. Jahani and Z. Jacob, “Photonic skin-depth engineering,” *Journal of the Optical Society of America B*, vol. 32, no. 7, pp. 1346–1353, 2015.
- [130] P. J. Bock, P. Cheben, J. H. Schmid, J. Lapointe, A. Delge, S. Janz, G. C. Aers, D.-X. Xu, A. Densmore, and T. J. Hall, “Subwavelength grating periodic structures in silicon-on-insulator: a new type of microphotonic waveguide,” *Optics Express*, vol. 18, no. 19, pp. 20 251–20 262, Sep. 2010.
- [131] R. Halir, P. J. Bock, P. Cheben, A. Ortega-Moux, C. Alonso-Ramos, J. H. Schmid, J. Lapointe, D.-X. Xu, J. G. Wangemert-Prez, . Molina-Fernandez, and S. Janz, “Waveguide sub-wavelength structures: a review of principles and applications,” *Laser & Photonics Reviews*, vol. 9, no. 1, pp. 25–49, Jan. 2015.
- [132] S.-H. Yang, M. L. Cooper, P. R. Bandaru, and S. Mookherjea, “Giant birefringence in multi-slotted silicon nanophotonic waveguides,” *Optics Express*, vol. 16, no. 11, p. 8306, May 2008.
- [133] U. Levy, M. Nezhad, H.-C. Kim, C.-H. Tsai, L. Pang, and Y. Fainman, “Implementation of a graded-index medium by use of subwavelength structures with graded fill factor,” *Journal of the Optical Society of America A*, vol. 22, no. 4, p. 724, Apr. 2005.
- [134] K. Murray, Z. Lu, H. Jayatileka, and L. Chrostowski, “Dense dissimilar waveguide routing for highly efficient thermo-optic switches on silicon,” *Optics Express*, vol. 23, no. 15, pp. 19 575–19 585, Jul. 2015.
- [135] F. Zhang, H. Yun, V. Donzella, Z. Lu, Y. Wang, Z. Chen, L. Chrostowski, and N. A. Jaeger, “Sinusoidal anti-coupling soi strip waveguides,” in *CLEO: Science and Innovations*. Optical Society of America, 2015, pp. SM1I–7.

- [136] S. Jahani and Z. Jacob, “Breakthroughs in photonics 2014: relaxed total internal reflection,” *IEEE Photonics Journal*, vol. 7, no. 3, pp. 1–5, 2015.
- [137] G. W. Milton, *The Theory of Composites*, 1st ed. Cambridge University Press, May 2002.
- [138] H. Herzig Sheinfux, I. Kaminker, Y. Plotnik, G. Bartal, and M. Segev, “Subwavelength Multilayer Dielectrics: Ultrasensitive Transmission and Breakdown of Effective-Medium Theory,” *Physical Review Letters*, vol. 113, no. 24, p. 243901, Dec. 2014.
- [139] R. Halir, P. Cheben, J. M. Luque-Gonzalez, J. D. Sarmiento-Merenguel, J. H. Schmid, G. Wangemert-Prez, D.-X. Xu, S. Wang, A. Ortega-Moux, and . Molina-Fernndez, “Ultra-broadband nanophotonic beamsplitter using an anisotropic sub-wavelength metamaterial,” *Laser & Photonics Reviews*, vol. 10, no. 6, pp. 1039–1046, Nov. 2016.
- [140] A. A. Sayem, M. R. C. Mahdy, and M. S. Rahman, “Broad angle negative refraction in lossless all dielectric or semiconductor based asymmetric anisotropic metamaterial,” *Journal of Optics*, vol. 18, no. 1, p. 015101, 2016.
- [141] J. Gomis-Bresco, D. Artigas, and L. Torner, “Anisotropy-induced photonic bound states in the continuum,” *Nature Photonics*, vol. 11, no. 4, pp. 232–236, Apr. 2017.
- [142] H. Li, S. Atakaramians, R. Lwin, X. Tang, Z. Yu, A. Argyros, and B. T. Kuhlmey, “Flexible single-mode hollow-core terahertz fiber with metamaterial cladding,” *Optica*, vol. 3, no. 9, pp. 941–947, 2016.
- [143] V. E. Babicheva, M. Y. Shalaginov, S. Ishii, A. Boltasseva, and A. V. Kildishev, “Finite-width plasmonic waveguides with hyperbolic multilayer cladding,” *Optics express*, vol. 23, no. 8, pp. 9681–9689, 2015.
- [144] J. M. Luque-González, A. Herrero-Bermello, A. Ortega-Moñux, Í. Molina-Fernández, A. V. Velasco, P. Cheben, J. H. Schmid, S. Wang, and R. Halir, “Tilted subwavelength gratings: controlling anisotropy in metamaterial nanophotonic waveguides,” *Optics Letters*, vol. 43, no. 19, pp. 4691–4694, 2018.
- [145] M. I. Dyakonov, “New type of electromagnetic wave propagating at an interface,” *Sov. Phys. JETP*, vol. 67, pp. 714–716, 1988.
- [146] O. Takayama, L. Crasovan, D. Artigas, and L. Torner, “Observation of Dyakonov Surface Waves,” *Physical Review Letters*, vol. 102, no. 4, p. 043903, Jan. 2009.
- [147] O. Takayama, D. Artigas, and L. Torner, “Lossless directional guiding of light in dielectric nanosheets using Dyakonov surface waves,” *Nature Nanotechnology*, vol. 9, no. 6, pp. 419–424, Jun. 2014.
- [148] J. Polo and A. Lakhtakia, “Surface electromagnetic waves: A review,” *Laser & Photonics Reviews*, vol. 5, no. 2, pp. 234–246, Mar. 2011.

- [149] N. Talebi, C. Ozsoy-Keskinbora, H. M. Benia, K. Kern, C. T. Koch, and P. A. van Aken, “Wedge Dyakonov Waves and Dyakonov Plasmons in Topological Insulator Bi₂Se₃ Probed by Electron Beams,” *ACS Nano*, vol. 10, no. 7, pp. 6988–6994, Jul. 2016.
- [150] M. T. Boroojerdi, M. Mnard, and A. G. Kirk, “Two-period contra-directional grating assisted coupler,” *Optics Express*, vol. 24, no. 20, pp. 22 865–22 874, Oct. 2016.
- [151] Y. Wang, X. Wang, J. Flueckiger, H. Yun, W. Shi, R. Bojko, N. A. Jaeger, and L. Chrostowski, “Focusing sub-wavelength grating couplers with low back reflections for rapid prototyping of silicon photonic circuits,” *Optics express*, vol. 22, no. 17, pp. 20 652–20 662, 2014.
- [152] CST Microwave Studio, <http://www.cst.com>.
- [153] M. Heiblum and J. Harris, “Analysis of curved optical waveguides by conformal transformation,” *IEEE Journal of Quantum Electronics*, vol. 11, no. 2, pp. 75–83, Feb. 1975.
- [154] Y. A. Vlasov and S. J. McNab, “Losses in single-mode silicon-on-insulator strip waveguides and bends,” *Optics Express*, vol. 12, no. 8, pp. 1622–1631, 2004.
- [155] E. A. J. Marcatili, “Bends in optical dielectric guides,” *The Bell System Technical Journal*, vol. 48, no. 7, pp. 2103–2132, Sep. 1969.
- [156] Z. Han, P. Zhang, and S. I. Bozhevolnyi, “Calculation of bending losses for highly confined modes of optical waveguides with transformation optics,” *Optics Letters*, vol. 38, no. 11, pp. 1778–1780, Jun. 2013.
- [157] Lumerical FDTD Solutions, <http://www.lumerical.com>.
- [158] R. J. Bojko, J. Li, L. He, T. Baehr-Jones, M. Hochberg, and Y. Aida, “Electron beam lithography writing strategies for low loss, high confinement silicon optical waveguides,” *Journal of Vacuum Science & Technology B*, vol. 29, no. 6, p. 06F309, Nov. 2011.
- [159] A. Khavasi, L. Chrostowski, Z. Lu, and R. Bojko, “Significant Crosstalk Reduction Using All-Dielectric CMOS-Compatible Metamaterials,” *IEEE Photonics Technology Letters*, vol. 28, no. 24, pp. 2787–2790, Dec. 2016.
- [160] S. K. Selvaraja, G. Winroth, S. Locorotondo, G. Murdoch, A. Milenin, C. Delvaux, P. Ong, S. Pathak, W. Xie, G. Sterckx, G. Lepage, D. V. Thourhout, W. Bogaerts, J. V. Campenhout, and P. Absil, “193nm immersion lithography for high-performance silicon photonic circuits,” *Proceeding of SPIE*, vol. 9052, p. 90520F, Apr. 2014.
- [161] P. Moitra, Y. Yang, Z. Anderson, I. I. Kravchenko, D. P. Briggs, and J. Valentine, “Realization of an all-dielectric zero-index optical metamaterial,” *Nature Photonics*, vol. 7, no. 10, pp. 791–795, Oct. 2013.
- [162] O. Reshef, P. Camayd-Muñoz, D. I. Vulis, Y. Li, M. Lončar, and E. Mazur, “Direct Observation of Phase-Free Propagation in a Silicon Waveguide,” *ACS Photonics*, vol. 4, no. 10, pp. 2385–2389, Oct. 2017.

- [163] S. Molesky, C. J. Dewalt, and Z. Jacob, “High temperature epsilon-near-zero and epsilon-near-pole metamaterial emitters for thermophotovoltaics,” *Optics Express*, vol. 21, no. 101, pp. A96–A110, Jan. 2013.
- [164] W. D. Newman, C. L. Cortes, J. Atkinson, S. Pramanik, R. G. DeCorby, and Z. Jacob, “FerrellBerreman Modes in Plasmonic Epsilon-near-Zero Media,” *ACS Photonics*, vol. 2, no. 1, pp. 2–7, Jan. 2015.
- [165] M. G. Silveirinha and N. Engheta, “Theory of supercoupling, squeezing wave energy, and field confinement in narrow channels and tight bends using ϵ near-zero metamaterials,” *Physical Review B*, vol. 76, no. 24, p. 245109, Dec. 2007.
- [166] A. M. Mahmoud, I. Liberal, and N. Engheta, “Dipole-dipole interactions mediated by epsilon-and-mu-near-zero waveguide supercoupling [Invited],” *Optical Materials Express*, vol. 7, no. 2, pp. 415–424, Feb. 2017.
- [167] L. Caspani, R. Kaipurath, M. Clerici, M. Ferrera, T. Roger, J. Kim, N. Kinsey, M. Pietrzyk, A. Di Falco, V. Shalaev, A. Boltasseva, and D. Faccio, “Enhanced nonlinear refractive index in ϵ -near-zero materials,” *Physical Review Letters*, vol. 116, no. 23, p. 233901, Jun. 2016.
- [168] H. Suchowski, K. O’Brien, Z. J. Wong, A. Salandrino, X. Yin, and X. Zhang, “Phase Mismatch-Free Nonlinear Propagation in Optical Zero-Index Materials,” *Science*, vol. 342, no. 6163, pp. 1223–1226, Dec. 2013.
- [169] G. A. Wurtz, R. Pollard, W. Hendren, G. P. Wiederrecht, D. J. Gosztola, V. A. Podolskiy, and A. V. Zayats, “Designed ultrafast optical nonlinearity in a plasmonic nanorod metamaterial enhanced by nonlocality,” *Nature Nanotechnology*, vol. 6, no. 2, p. 107, Feb. 2011.
- [170] L. H. Nicholls, F. J. Rodriguez-Fortuo, M. E. Nasir, R. M. Crdova-Castro, N. Olivier, G. A. Wurtz, and A. V. Zayats, “Ultrafast synthesis and switching of light polarization in nonlinear anisotropic metamaterials,” *Nature Photonics*, vol. 11, no. 10, p. 628, Oct. 2017.
- [171] A. Poddubny, I. Iorsh, P. Belov, and Y. Kivshar, “Hyperbolic metamaterials,” *Nature Photonics*, vol. 7, no. 12, pp. 948–957, Nov. 2013.
- [172] P. Shekhar, J. Atkinson, and Z. Jacob, “Hyperbolic metamaterials: fundamentals and applications,” *Nano Convergence*, vol. 1, no. 1, Dec. 2014.
- [173] J. Yao, Z. Liu, Y. Liu, Y. Wang, C. Sun, G. Bartal, A. M. Stacy, and X. Zhang, “Optical Negative Refraction in Bulk Metamaterials of Nanowires,” *Science*, vol. 321, no. 5891, pp. 930–930, Aug. 2008.
- [174] A. V. Kabashin, P. Evans, S. Pastkovsky, W. Hendren, G. A. Wurtz, R. Atkinson, R. Pollard, V. A. Podolskiy, and A. V. Zayats, “Plasmonic nanorod metamaterials for biosensing,” *Nature Materials*, vol. 8, no. 11, pp. 867–871, Nov. 2009.
- [175] R. Starko-Bowes, J. Atkinson, W. Newman, H. Hu, T. Kallos, G. Palikaras, R. Fedosejevs, S. Pramanik, and Z. Jacob, “Optical characterization of epsilon-near-zero, epsilon-near-pole, and hyperbolic response in nanowire metamaterials,” *Journal of the Optical Society of America B*, vol. 32, no. 10, p. 2074, Oct. 2015.

- [176] Z. Liu, H. Lee, Y. Xiong, C. Sun, and X. Zhang, “Far-Field Optical Hyperlens Magnifying Sub-Diffraction-Limited Objects,” *Science*, vol. 315, no. 5819, pp. 1686–1686, Mar. 2007.
- [177] Z. Jacob, I. I. Smolyaninov, and E. E. Narimanov, “Broadband Purcell effect: Radiative decay engineering with metamaterials,” *Applied Physics Letters*, vol. 100, no. 18, p. 181105, Apr. 2012.
- [178] O. Kidwai, S. V. Zhukovsky, and J. E. Sipe, “Dipole radiation near hyperbolic metamaterials: applicability of effective-medium approximation,” *Optics Letters*, vol. 36, no. 13, pp. 2530–2532, Jul. 2011.
- [179] P. Shekhar, M. Malac, V. Gaiand, N. Dalili, A. Meldrum, and Z. Jacob, “Momentum-Resolved Electron Energy Loss Spectroscopy for Mapping the Photonic Density of States,” *ACS Photonics*, vol. 4, no. 4, pp. 1009–1014, Apr. 2017.
- [180] C. L. Cortes and Z. Jacob, “Photonic analog of a van Hove singularity in metamaterials,” *Physical Review B*, vol. 88, no. 4, Jul. 2013.
- [181] R. W. Boyd, *Nonlinear Optics*, 3rd ed. Academic Press, 2003.
- [182] M. Kauranen and A. V. Zayats, “Nonlinear plasmonics,” *Nature Photonics*, vol. 6, no. 11, pp. 737–748, Nov. 2012.
- [183] R. S. Bennink, Y.-K. Yoon, R. W. Boyd, and J. E. Sipe, “Accessing the optical nonlinearity of metals with metaldielectric photonic bandgap structures,” *Optics Letters*, vol. 24, no. 20, p. 1416, Oct. 1999.
- [184] A. K. Sarychev and V. M. Shalaev, “Electromagnetic field fluctuations and optical nonlinearities in metal-dielectric composites,” *Physics Reports*, vol. 335, no. 6, pp. 275–371, Sep. 2000.
- [185] N. N. Lepeshkin, A. Schweinsberg, G. Piredda, R. S. Bennink, and R. W. Boyd, “Enhanced Nonlinear Optical Response of One-Dimensional Metal-Dielectric Photonic Crystals,” *Physical Review Letters*, vol. 93, no. 12, Sep. 2004.
- [186] M. Scalora, N. Mattiucci, G. DAguanno, M. Larciprete, and M. J. Bloemer, “Nonlinear pulse propagation in one-dimensional metal-dielectric multilayer stacks: Ultrawide bandwidth optical limiting,” *Physical Review E*, vol. 73, no. 1, Jan. 2006.
- [187] A. Husakou and J. Herrmann, “Steplike Transmission of Light through a Metal-Dielectric Multilayer Structure due to an Intensity-Dependent Sign of the Effective Dielectric Constant,” *Physical Review Letters*, vol. 99, no. 12, p. 127402, Sep. 2007.
- [188] S. Campione, T. S. Luk, S. Liu, and M. B. Sinclair, “Optical properties of transiently-excited semiconductor hyperbolic metamaterials,” *Optical Materials Express*, vol. 5, no. 11, pp. 2385–2394, Nov. 2015.
- [189] C. Argyropoulos, N. M. Estakhri, F. Monticone, and A. Alù, “Negative refraction, gain and nonlinear effects in hyperbolic metamaterials,” *Optics Express*, vol. 21, no. 12, pp. 15 037–15 047, Jun. 2013.

- [190] O. V. Shramkova and G. P. Tsironis, “Nonreciprocal nonlinear wave scattering by loss-compensated active hyperbolic structures,” *Scientific Reports*, vol. 7, p. 42919, Feb. 2017.
- [191] N. M. Litchinitser, A. I. Maimistov, I. R. Gabitov, R. Z. Sagdeev, and V. M. Shalaev, “Metamaterials: electromagnetic enhancement at zero-index transition,” *Optics Letters*, vol. 33, no. 20, pp. 2350–2352, Oct. 2008.
- [192] M. Dalarsson and P. Tassin, “Analytical solution for wave propagation through a graded index interface between a right-handed and a left-handed material,” *Optics Express*, vol. 17, no. 8, pp. 6747–6752, Apr. 2009.
- [193] B. Wells, Z. A. Kudyshev, N. Litchinitser, and V. A. Podolskiy, “Nonlocal Effects in Transition Hyperbolic Metamaterials,” *ACS Photonics*, vol. 4, no. 10, pp. 2470–2478, Oct. 2017.
- [194] N. F. Mott and L. Friedman, “Metal-insulator transitions in VO₂, Ti₂O₃ and Ti_{2-x}V_xO₃,” *The Philosophical Magazine: A Journal of Theoretical Experimental and Applied Physics*, vol. 30, no. 2, pp. 389–402, Aug. 1974.
- [195] M. I. Stockman, “Nanoplasmonics: past, present, and glimpse into future,” *Optics Express*, vol. 19, no. 22, pp. 22 029–22 106, Oct. 2011.
- [196] A. V. Chebykin, A. A. Orlov, A. S. Shalin, A. N. Poddubny, and P. A. Belov, “Strong Purcell effect in anisotropic ϵ -near-zero metamaterials,” *Physical Review B*, vol. 91, no. 20, p. 205126, May 2015.
- [197] I. Charaev, A. Semenov, S. Doerner, G. Gomard, K. Ilin, and M. Siegel, “Current dependence of the hot-spot response spectrum of superconducting single-photon detectors with different layouts,” *Superconductor Science and Technology*, vol. 30, no. 2, p. 025016, 2016.
- [198] R. H. Hadfield, “Single-photon detectors for optical quantum information applications,” *Nature Photonics*, vol. 3, no. 12, p. 696, Dec. 2009.
- [199] G. N. Goltsman, O. Okunev, G. Chulkova, A. Lipatov, A. Semenov, K. Smirnov, B. Voronov, A. Dzardanov, C. Williams, and R. Sobolewski, “Picosecond superconducting single-photon optical detector,” *Applied Physics Letters*, vol. 79, no. 6, pp. 705–707, 2001.
- [200] M. D. Eisaman, J. Fan, A. Migdall, and S. V. Polyakov, “Invited Review Article: Single-photon sources and detectors,” *Review of Scientific Instruments*, vol. 82, no. 7, p. 071101, Jul. 2011.
- [201] Q.-Y. Zhao, D. Zhu, N. Calandri, A. E. Dane, A. N. McCaughan, F. Bellei, H.-Z. Wang, D. F. Santavicca, and K. K. Berggren, “Single-photon imager based on a superconducting nanowire delay line,” *Nature Photonics*, vol. 11, no. 4, p. 247, Apr. 2017.
- [202] F. Marsili, V. B. Verma, J. A. Stern, S. Harrington, A. E. Lita, T. Gerrits, I. Vayshenker, B. Baek, M. D. Shaw, R. P. Mirin, and S. W. Nam, “Detecting single infrared photons with 93% system efficiency,” *Nature Photonics*, vol. 7, no. 3, p. 210, Mar. 2013.

- [203] M. Sidorova, A. Semenov, A. Kuzmin, I. Charaev, S. Doerner, and M. Siegel, “Intrinsic Jitter in Photon Detection by Straight Superconducting Nanowires,” *IEEE Transactions on Applied Superconductivity*, pp. 1–1, 2018.
- [204] W. H. P. Pernice, C. Schuck, O. Minaeva, M. Li, G. N. Goltsman, A. V. Sergienko, and H. X. Tang, “High-speed and high-efficiency travelling wave single-photon detectors embedded in nanophotonic circuits,” *Nature Communications*, vol. 3, p. 1325, Dec. 2012.
- [205] M. Tarkhov, J. Claudon, J. P. Poizat, A. Korneev, A. Divochiy, O. Minaeva, V. Seleznev, N. Kaurova, B. Voronov, A. V. Semenov, and G. Goltsman, “Ultrafast reset time of superconducting single photon detectors,” *Applied Physics Letters*, vol. 92, no. 24, p. 241112, Jun. 2008.
- [206] K. Epstein, A. M. Goldman, and A. M. Kadin, “Vortex-antivortex pair dissociation in two-dimensional superconductors,” *Physical Review Letters*, vol. 47, no. 7, pp. 534–537, 1981.
- [207] L. N. Bulaevskii, M. J. Graf, and V. G. Kogan, “Vortex-assisted photon counts and their magnetic field dependence in single-photon superconducting detectors,” *Physical Review B*, vol. 85, no. 1, p. 014505, 2012.
- [208] A. Engel and A. Schilling, “Numerical analysis of detection-mechanism models of superconducting nanowire single-photon detector,” *Journal of Applied Physics*, vol. 114, no. 21, p. 214501, 2013.
- [209] F. Marsili, M. J. Stevens, A. Kozorezov, V. B. Verma, C. Lambert, J. A. Stern, R. D. Horansky, S. Dyer, S. Duff, D. P. Pappas, A. E. Lita, M. D. Shaw, R. P. Mirin, and S. W. Nam, “Hotspot relaxation dynamics in a current-carrying superconductor,” *Physical Review B*, vol. 93, no. 9, p. 094518, Mar. 2016.
- [210] Y. Korneeva, I. Florya, S. Vdovichev, M. Moshkova, N. Simonov, N. Kaurova, A. Korneev, and G. Goltsman, “Comparison of Hot Spot Formation in NbN and MoN Thin Superconducting Films After Photon Absorption,” *IEEE Transactions on Applied Superconductivity*, vol. 27, no. 4, pp. 1–4, Jun. 2017.
- [211] A. Semenov, A. Engel, H.-W. Hbers, K. Il’in, and M. Siegel, “Spectral cut-off in the efficiency of the resistive state formation caused by absorption of a single-photon in current-carrying superconducting nano-strips,” *The European Physical Journal B - Condensed Matter and Complex Systems*, vol. 47, no. 4, pp. 495–501, Oct. 2005.
- [212] A. N. Zotova and D. Y. Vodolazov, “Photon detection by current-carrying superconducting film: A time-dependent Ginzburg-Landau approach,” *Physical Review B*, vol. 85, no. 2, p. 024509, Jan. 2012.
- [213] L. N. Bulaevskii, M. J. Graf, C. D. Batista, and V. G. Kogan, “Vortex-induced dissipation in narrow current-biased thin-film superconducting strips,” *Physical Review B*, vol. 83, no. 14, p. 144526, 2011.
- [214] D. Y. Vodolazov, Y. P. Korneeva, A. Semenov, A. Korneev, and G. Goltsman, “Vortex-assisted mechanism of photon counting in a superconducting nanowire single-photon detector revealed by external magnetic field,” *Physical Review B*, vol. 92, no. 10, p. 104503, 2015.

- [215] A. D. Semenov, G. N. Goltsman, and A. A. Korneev, “Quantum detection by current carrying superconducting film,” *Physica C: Superconductivity*, vol. 351, no. 4, pp. 349–356, 2001.
- [216] A. Engel, J. Lonsky, X. Zhang, and A. Schilling, “Detection mechanism in SNSPD: Numerical results of a conceptually simple, yet powerful detection model,” *IEEE Transactions on Applied Superconductivity*, vol. 25, no. 3, pp. 1–7, 2015.
- [217] H. Bartolf, A. Engel, A. Schilling, K. Ilin, M. Siegel, H.-W. Hbers, and A. Semenov, “Current-assisted thermally activated flux liberation in ultrathin nanopatterned NbN superconducting meander structures,” *Physical Review B*, vol. 81, no. 2, p. 024502, 2010.
- [218] M. Tinkham, *Introduction to superconductivity*. Courier Corporation, 2004.
- [219] V. G. Kogan, “Interaction of vortices in thin superconducting films and the Berezinskii-Kosterlitz-Thouless transition,” *Physical Review B*, vol. 75, no. 6, p. 064514, Feb. 2007.
- [220] J. Pearl, “Current distribution in superconducting films carrying quantized fluxoids,” *Applied Physics Letters*, vol. 5, no. 4, pp. 65–66, Aug. 1964.
- [221] A. M. Kadin, M. Leung, and A. D. Smith, “Photon-assisted vortex depairing in two-dimensional superconductors,” *Physical Review Letters*, vol. 65, no. 25, pp. 3193–3196, Dec. 1990.
- [222] J. R. Clem, “Time-dependent voltage generated by flux motion across a superconducting strip,” *Journal of Low Temperature Physics*, vol. 42, no. 3-4, pp. 363–371, Feb. 1981.
- [223] D. F. Santavicca, J. K. Adams, L. E. Grant, A. N. McCaughan, and K. K. Berggren, “Microwave dynamics of high aspect ratio superconducting nanowires studied using self-resonance,” *Journal of Applied Physics*, vol. 119, no. 23, p. 234302, Jun. 2016.
- [224] T. Yamashita, S. Miki, K. Makise, W. Qiu, H. Terai, M. Fujiwara, M. Sasaki, and Z. Wang, “Origin of intrinsic dark count in superconducting nanowire single-photon detectors,” *Applied Physics Letters*, vol. 99, no. 16, p. 161105, Oct. 2011.
- [225] J. R. Clem and K. K. Berggren, “Geometry-dependent critical currents in superconducting nanocircuits,” *Physical Review B*, vol. 84, no. 17, Nov. 2011.
- [226] A. Murphy, A. Semenov, A. Korneev, Y. Korneeva, G. Goltsman, and A. Bezryadin, “Three Temperature Regimes in Superconducting Photon Detectors: Quantum, Thermal and Multiple Phase-Slips as Generators of Dark Counts,” *Scientific Reports*, vol. 5, p. 10174, May 2015.
- [227] L.-P. Yang, H. X. Tang, and Z. Jacob, “Concept of quantum timing jitter and non-Markovian limits in single-photon detection,” *Physical Review A*, vol. 97, no. 1, p. 013833, Jan. 2018.
- [228] L.-P. Yang and Z. Jacob, “Quantum critical detector: Amplifying weak signals using first-order dynamical quantum phase transitions,” *arXiv preprint arXiv:1807.04617*, 2018.

- [229] H. Wu, C. Gu, Y. Cheng, and X. Hu, “Vortex-crossing-induced timing jitter of superconducting nanowire single-photon detectors,” *Applied Physics Letters*, vol. 111, no. 6, p. 062603, Aug. 2017.
- [230] N. Calandri, Q.-Y. Zhao, D. Zhu, A. Dane, and K. K. Berggren, “Superconducting nanowire detector jitter limited by detector geometry,” *Applied Physics Letters*, vol. 109, no. 15, p. 152601, Oct. 2016.
- [231] J. A. OConnor, M. G. Tanner, C. M. Natarajan, G. S. Buller, R. J. Warburton, S. Miki, Z. Wang, S. W. Nam, and R. H. Hadfield, “Spatial dependence of output pulse delay in a niobium nitride nanowire superconducting single-photon detector,” *Applied Physics Letters*, vol. 98, no. 20, p. 201116, May 2011.
- [232] Y. Cheng, C. Gu, and X. Hu, “Inhomogeneity-induced timing jitter of superconducting nanowire single-photon detectors,” *Applied Physics Letters*, vol. 111, no. 6, p. 062604, Aug. 2017.
- [233] J. P. Allmaras, A. G. Kozorezov, B. A. Korzh, and M. D. Shaw, “Intrinsic timing jitter and latency in superconducting single photon nanowire detectors,” *arXiv:1805.00130 [physics]*, Apr. 2018, arXiv: 1805.00130.
- [234] J. Renema, G. Frucci, Z. Zhou, F. Mattioli, A. Gaggero, R. Leoni, M. J. de Dood, A. Fiore, and M. P. van Exter, “Universal response curve for nanowire superconducting single-photon detectors,” *Physical Review B*, vol. 87, no. 17, p. 174526, 2013.
- [235] M. Caloz, B. Korzh, N. Timoney, M. Weiss, S. Gariglio, R. J. Warburton, C. Schnenberger, J. Renema, H. Zbinden, and F. Bussires, “Optically probing the detection mechanism in a molybdenum silicide superconducting nanowire single-photon detector,” *Applied Physics Letters*, vol. 110, no. 8, p. 083106, Feb. 2017.
- [236] A. D. Semenov, P. Haas, H.-W. Hübers, K. Ilin, M. Siegel, A. Kirste, T. Schurig, and A. Engel, “Vortex-based single-photon response in nanostructured superconducting detectors,” *Physica C: Superconductivity and its Applications*, vol. 468, no. 7, pp. 627–630, 2008.
- [237] M. Hofherr, D. Rall, K. Ilin, M. Siegel, A. Semenov, H.-W. Hübers, and N. Gippius, “Intrinsic detection efficiency of superconducting nanowire single-photon detectors with different thicknesses,” *Journal of Applied Physics*, vol. 108, no. 1, p. 014507, 2010.
- [238] K. M. Rosfjord, J. K. W. Yang, E. A. Dauler, A. J. Kerman, V. Anant, B. M. Voronov, G. N. Goltsman, and K. K. Berggren, “Nanowire Single-photon detector with an integrated optical cavity and anti-reflection coating,” *Optics Express*, vol. 14, no. 2, pp. 527–534, Jan. 2006.
- [239] A. Vetter, S. Ferrari, P. Rath, R. Alaei, O. Kahl, V. Kovalyuk, S. Diewald, G. N. Goltsman, A. Korneev, C. Rockstuhl *et al.*, “Cavity-enhanced and ultrafast superconducting single-photon detectors,” *Nano letters*, vol. 16, no. 11, pp. 7085–7092, 2016.
- [240] J. Münzberg, A. Vetter, F. Beutel, W. Hartmann, S. Ferrari, W. H. Pernice, and C. Rockstuhl, “Superconducting nanowire single-photon detector implemented in a 2d photonic crystal cavity,” *Optica*, vol. 5, no. 5, pp. 658–665, May 2018.

- [241] F. Najafi, J. Mower, N. C. Harris, F. Bellei, A. Dane, C. Lee, X. Hu, P. Kharel, F. Marsili, S. Assefa, K. K. Berggren, and D. Englund, “On-chip detection of non-classical light by scalable integration of single-photon detectors,” *Nature Communications*, vol. 6, p. 5873, Jan. 2015.
- [242] S. Jahani, S. Kim, J. Atkinson, J. C. Wirth, F. Kalhor, A. A. Noman, W. D. Newman, P. Shekhar, K. Han, V. Van, R. G. DeCorby, L. Chrostowski, M. Qi, and Z. Jacob, “Controlling evanescent waves using silicon photonic all-dielectric metamaterials for dense integration,” *Nature Communications*, vol. 9, no. 1, p. 1893, 2018.
- [243] M. K. Akhlaghi, E. Schelew, and J. F. Young, “Waveguide integrated superconducting single-photon detectors implemented as near-perfect absorbers of coherent radiation,” *Nature Communications*, vol. 6, p. 8233, Sep. 2015.
- [244] K. Han, S. Kim, J. Wirth, M. Teng, Y. Xuan, B. Niu, and M. Qi, “Strip-slot direct mode coupler,” *Optics Express*, vol. 24, no. 6, p. 6532, Mar. 2016.
- [245] S. Xiao, M. H. Khan, H. Shen, and M. Qi, “Modeling and measurement of losses in silicon-on-insulator resonators and bends,” *Optics Express*, vol. 15, no. 17, p. 10553, 2007.